UNIVERSITY OF PALERMO
PHD JOINT PROGRAM:
UNIVERSITY OF CATANIA - UNIVERSITY OF MESSINA
XXXV CYCLE

DOCTORAL THESIS

Computational Assessment of Fluid Flow in Stenotic Arteries: Applications in Targeted Drug Therapy

Author:
NIMRA MUQADDASS

Supervisor:
Prof. FRANCESCO OLIVERI

Co-Supervisor:
Prof. Alessandra Jannelli

A thesis submitted in fulfillment of the requirements for the degree of Doctor of Philosophy

in

Mathematics and Computational Sciences

June 24, 2024

Signed: 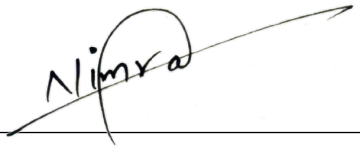

Date: 24.06.2024

"Life is not easy for any of us, but what of that? We must have perseverance and above all confidence in ourselves. We must believe that we are gifted in something, and that this thing, at whatever cost, must be attained. "

Marie Curie

UNIVERSITY OF PALERMO

Abstract

Department of Mathematics and Computer Sciences

Doctor of Philosophy

Computational Assessment of Fluid Flow in Stenotic Arteries: Applications in Targeted Drug Therapy

by NIMRA MUQADDASS

Blood flow dynamics are crucial in the development and progression of cardiovascular diseases. Computational modeling of blood circulation in arteries is vital for understanding disease symptoms and enhancing treatments. Aneurysms, stenoses, and atherosclerosis can change blood flow characteristics, leading to serious health complications due to abnormal blood flow patterns and high wall shear stresses (WWS). Simulating these changes can help in detecting cardiovascular diseases early and managing them effectively.

The commencement of the dissertation involves an effort to create a model of the 2D shape of a non-uniform artery wall that has a restricted segment, using a segmented function, which includes an obstruction of approximately 40%. The blood flow in the body follows a rhythmic pressure gradient that imitates the heart's systolic and diastolic phases. Because blood behaves like a non-Newtonian fluid in certain situations, the Casson model for non-Newtonian fluids is used to account for the yield stress resulting from the formation of red blood cell aggregates at low shear rates. The Navier-Stokes equations, which describe incompressible and unsteady fluid flow, are expanded to include the non-Newtonian behavior of blood flow in radial coordinates. This is accomplished by including a temperature equation.

To analyze the impact of stenosis over the flow, drug delivery agents such as copper (Cu) and alumina (Al_2O_3) nanoparticles with a concentration of about 0.03% are used. The concept of magnetohydrodynamics (MHD) involves applying a magnetic field to blood flow in an artery, taking into account the Hall current, to deliver magnetic drug carriers to a specific location within the bloodstream. The simulation of blood flow begins from a state of rest with zero velocity and temperature, using initial conditions to simplify the mathematical modeling process. On the symmetry axis, a zero radial gradient condition is applied to both velocity and temperature, while no-slip conditions are applied to the arterial wall.

The complexity of the governing partial differential equations is removed by non-dimensionalizing them. There are two cases to consider: the first case involves disregarding the long wavelength approach, which remains open issue for future consideration. The alternative scenario involves presenting the acquired dimensionless PDEs through the long-wavelength approximation and then applying a radial coordinate transformation to simplify them even further. Afterward, MATLAB software is utilized to execute the 2D explicit forward time central space (FTCS) differentiation method. Momentum and thermal analysis were done for blood, Cu-blood nanofluid, and Cu-Al_2O_3-blood hybrid nanofluid, along with wall shear stress (WWS) and local Nusselt number (Nu_{local}) evaluation.

We proceed to revise the last batch of dimensional partial differential equations (PDEs) describing the behavior of non-Newtonian Cu-Al_2O_3-blood by incorporating magnetohydrodynamic (MHD) effects. Our approach involves converting the PDEs into a Reynolds-averaged Navier Stokes equation (RANS), which employs Reynolds averaging to account for turbulence in the mean flow. This is achieved by decomposing the flow variables into average and perturbed components. The equations for fluid dynamics include turbulent forces caused by eddy shear and molecular turbulence. These forces are accounted for using Boussinesq's eddy-viscosity hypothesis, which is based on the average flow of the fluid. Additionally, the Zero-equation turbulence model, which is also called the algebraic turbulence model, is utilized by combining the principles of Prandtl mixing length and Boussinesq approximation. Turbulent flow is considered unsteady and fully developed, and flow properties are also modified using the Prandtl mixing length model with the laminar and turbulent effect contribution. The subsequent step involves making these equations non-dimensional and then utilizing radial coordinate transformations. The resulting set of dimensionless partial differential equations that consists of Reynold and turbulent Prandtl numbers are then simulated using FTCS methodology. Additionally, the effect of various emerging parameters is analyzed through a graphical representation of the momentum equation for high Reynold numbers (Re = 42000, 46000).
The last analysis involved flow momentum and pressure for the laminar flow scenario by considering blood as a Newtonian fluid. Using AutoCAD software, a 3D constricted artery with a 70% elliptical shaped stenosis was created. To proceed further, an ideal mesh was created using OpenFOAM's `blockMesh` and `snappyHexMesh` tools. The simulation for laminar and incompressible flow has been conducted using the `icoFoam` solver, which guarantees the convergence of the simulation at Courant number $\approx 0.2 < 1$. Two different scenarios have been taken into account for the velocity inlet. Firstly, a parabolic velocity profile was used with a maximum inlet velocity of $0.003m/s$. The outlet velocity was set to zero gradient and the inlet pressure was also set to zero. Secondly, we used a constant inlet velocity of $0.0137m/s$ for laminar flow with a Reynolds number of 200. We graphically analyzed the momentum and pressure of the fluid both at the center of the stricture and throughout the constriction arterial segment for both inlet velocity conditions.

Acknowledgements

I stand at the culmination of an incredible journey that has spanned several years, a journey filled with challenges and opportunities, learning and growth, and I am profoundly grateful to the multitude of people who have supported me along this path. First and foremost, I extend my deepest gratitude to my parents, whose unwavering support and ceaseless prayers have been my guiding light and constant source of strength. They have instilled in me the values of perseverance and dedication, which have been indispensable throughout my Ph.D. Their belief in my abilities and their unconditional love have been the bedrock of my resolve, and for that, I am eternally indebted.

I am immensely thankful to my Ph.D. advisors, Prof. Francesco Oliveri and Prof. Alessandra Jannelli, whose expertise and insightful guidance have been pivotal in my research. Their mentorship has been a beacon of inspiration, encouraging me to push my knowledge's boundaries and strive for excellence in my scholarly pursuits. Their constructive criticism and patient instruction have shaped both my thesis and my approach to scientific inquiry. Also, special thanks are due to Prof. Maria Carmela Lombardo, my Ph.D. coordinator, for her unwavering support and invaluable advice throughout my doctoral studies and have helped me navigate the complexities of the Ph.D. program.

I am also deeply grateful to my Ph.D. collaborators, Prof. Carlo Massimo Casciola, Prof. Paolo Gualtieri, and Prof. Francesco Battista, at the Department of Mechanical and Aerospace Engineering, Sapienza Roma. Their collaboration has been instrumental in refining my research methodology and in broadening the scope of my academic perspective. Their willingness to share their vast knowledge and expertise has greatly enriched my research experience.

I owe a debt of gratitude to my friends from the Pakistani community, who have been a source of constant encouragement and companionship. Their support during my best and worst times has been a testament to the enduring spirit of camaraderie and solidarity. They have not only shared in my academic endeavors but have also been a vital part of my personal growth, offering comfort and cheer, laughter and solace.

In essence, this thesis is not just a reflection of my work but a mosaic of the contributions from all those who have been a part of my Ph.D. journey. To all those who have offered their goodwill, counsel, and friendship, I am thankful beyond words. Your collective belief in my potential has been the wind beneath my wings, propelling me toward this significant academic milestone.

As I contemplate the future, I carry with me not only the knowledge that I have acquired but also the relationships that I have treasured, the challenges that I have overcome, and the memories that I have created. My journey so far has been enriching and enlightening, and for that, I am deeply grateful to all of you.

Nimra Muqaddass

Contents

List of Figures

List of Tables

List of Abbreviations

NSE	Navier stokes equation
RANS	Reynolds average Navier Stokes Equation
DNS	Direct numerical simulation
LES	Large eddy simulation
URANS	Unsteady Reynolds average Navier Stokes Equation
FTCS	Forward time central space
IC	Initial conditions
BC	Boundary conditions
NF	Nanofluid
HNF	Hybrid nanofluid
ODEs	Ordinary differential equations
PDEs	Partial differential equations
VOF	Volume of Fluid
CVD	Cardovascular diseases
CAD	Coronary artery disease
PAD	Peripheral artery disease
NPs	Nanoparticles
MNPs	Magnetic nanoparticles
PML	Prandtl mixing length

List of Symbols

English symbols

L	Length of arterial section	m
$(\widetilde{r}, \widetilde{z})$	Dimensional cylindrical coordinates	m
(r, z)	Dmensionless cylindrical coordinates	m
$\widetilde{t}$	Dimensional time	s
t	Dmensionless time	s
$(\widetilde{u}, \widetilde{w})$	Components of dimensional velocity	ms^{-1}
(u, w)	Components of dimensionless velocity	ms^{-1}
R_0	Radius of arterial section	m
$\widetilde{p}$	Dimensional pressure	Pa
p	Dimensionless pressure	Pa
Cu	Copper nanoparticles	
Al_2O_3	Alumina nanoparticles	
e_{ij}	Strain rate	
P_y	Fluid's yield stress	Nm^{-2}
$\widetilde{T}$	Dimensional temperature field	K
l_0	Stenotic region length	m
m	Hall current	
C_p	Spacific heat capacity	$Jkg^{-1}K^{-1}$
p_0	Pressure gradient amplitude	Nm^{-3}
p_1	Amplitude of pulsatile component of pressure	Nm^{-2}
$\widetilde{d}$	Stenotic region distance from origin	m
f_p	Pulse frequency	Hz
Re	Dimensionless Reynolds number	
Pr	Dimensionless Prandtl number	
Ec	Dimensionless Eckert number	
M	Dimensionless Hartmann number	
T_w	Wall temperature	K
A_0	Constant pressure gradient	Nm^{-3}
e	Amplitude of fluctuating component	
$\boldsymbol{J}$	Current density	
$\boldsymbol{E}$	Electric field	
P_e	Electron pressure	

Greek symbols

β	Casson model parameter	
ω	Angular frequency	$rad\,s^{-1}$
ρ	Density	kgm^{-3}
κ	Thermal conductivity	$Wm^{-1}K^{-1}$
ϵ	Vassel aspect ratio	

ϕ	Volume fraction of particles	
β_0	Magnetic field strength	T
δ^*	Severity of stenosis	
τ_{ij}	Shear stress	
π_{ij}	Square of deformation rate	
μ_b	Casson viscosity	$\mathrm{Kgm^{-1}s^{-1}}$
μ	Dynamic viscosity	$\mathrm{Kgm^{-1}s^{-1}}$
σ	Electric conductivity	

Subscript/Superscript

f	Ordinary fluid
nf	Nanofluid
hnf	Hybrid nanofluid

To my beloved parents

Introduction

Initial Overview

Cardiovascular diseases (CVDs) remain a global health concern, necessitating continual advancements in the understanding and management of arterial conditions. Throughout a person's lifetime, the heart pumps approximately 5 liters of blood into the cardiovascular circulatory system every minute in order to maintain the proper functioning of organs, tissues, and cells. Although this system has evolved to be highly effective, it is still vulnerable to a variety of different heart and vascular disorders. In fact, cardiovascular diseases (CVDs) are to date the most common cause of death both in Italy and worldwide (Ritchie, 2018) (Figure 1). According to the World Health Organization (WHO) (Mendis, Puska, and Norrving, 2011), many premature deaths, including 3 million people under 60 years old, could have been prevented through improved diagnostics and interventions. For proper function and survival, the cardiovascular system, which includes the heart, blood vessels, and blood, is responsible for a continuous supply of nutrients and oxygen, as well as the removal of waste products (Paulsen, 2010; Tortora and Grabowski, 2000).

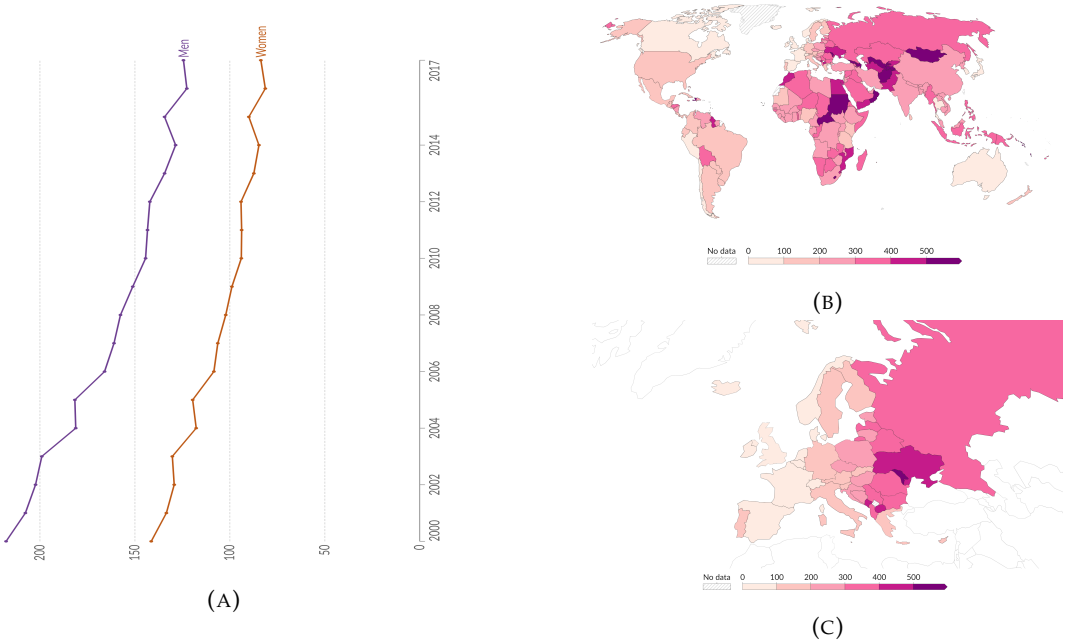

(A)

(B)

(C)

FIGURE 1: **(A)** The number of deaths caused by CVDs in Italy, categorized by gender and on a yearly basis, from 2000 to 2017. **(B)** Globally, and per 100,000 population, the average death rate from CVDs in 2017. **C** Europe's 2017 CVD death rate: per 100,000. The data and images were adapted from Our World in Data (Ritchie, 2018).

The presence of red blood cells plays a vital role in determining the behavior of blood and its properties Table 1. Therefore, a comprehensive understanding of the impact of these cells on the fluid properties is essential for developing effective

preventative measures against vascular diseases. The obstruction of vessels leads to reduced blood flow and slower circulation, which can be attributed to wall shear stress. As such, it is crucial to examine hemodynamic factors related to blood and vessels to gain a better understanding of arterial diseases (Huang et al., 1987). Numerous research studies have showcased the successful application of experimental and numerical methods in the field of medical treatment. Among these, Chen and Lu (2004) conducted an investigation into the wall shear stress of blood, utilizing the Carreau-Yasuda fluid model. Concurrently, Perktold et al. (1991) analyzed blood as a Newtonian fluid, comparing their velocity profile and wall shear stress distribution findings to those of Ku and Gidden (1983).

TABLE 1: An overview of blood components (Hoskins and Hardman, 2017).

Blood Components	**Principle Functions**	**% by Volume**
Plasma	Transports blood, carbon dioxide, and nutrients	50–60
Red cells	Oxygen carriers	40–50
White cells	Body's immune system	0.7
Platelets	Clot formation of blood	0.3
Macromolecules: albumin	To maintain oncotic pressure	2
Other	Various	1.5

The circulatory system relies on the transportation of a vital fluid called blood, which is responsible for delivering oxygen, nutrients, and hormones to various parts of the body. This complex system ensures that all the organs and tissues receive the necessary resources to function optimally. (Yan et al., 2020b) had investigated the hemodynamic rheology inside an arterial segment having a cone shape of stenosis. (Kojić et al., 2008) studied blood flow through the cardiovascular system, which is one of the essential phenomena in biomedical engineering. For doctors, the turbulent blood flow is more interesting, which might happen due to the increase in flow to a particular value, narrowing of the blood vessels, or the presence of eddies and stenosis swirling vortexes. (Shi, Lawford, and Hose, 2011) considered the blood a homogeneous fluid with different properties depending on the size of the blood vessel. (Elhanafy, Elsaid, and Guaily, 2020b) had numerically evaluated the hemodynamic characteristics of blood flow in arterial stenotic sections with multiple degrees of stenosis. The transport of molecules in a fluid is governed by convective-diffusive laws. Therefore, (Kojic et al., 2017) modeled the Navier–Stokes equations and the incompressibility equation, considering blood as a viscous, incompressible, and homogeneous fluid within the vessel. One such study, conducted by (Haldar, 1985a), analyzed blood flow in stenotic regions of various shapes and identified how these areas could impede the flow in arterial segments. The blood flow problem for an arterial stenotic region was mathematically modeled by(Chakravarty and Mandal, 1994b). Within a tapered stenotic region, (Mandal, 2005b) interpreted the non-Newtonian blood flow modeled by Power law fluid numerically for time-variant stenosis.

Fluid flows in nature and engineering applications are usually turbulent, characterized by chaotic movements in a flow that was previously regular or laminar. This

transition from laminar to turbulent flow occurs due to various reasons, such as an increase in the flow's speed or characteristic length, as convective forces overcome viscous forces. The Reynolds number, which is the ratio between convective and viscous forces, is used to classify different flow types. Turbulent flows are known for their irregularity, diffusivity, and vorticity, with a wide range of vortical structures in space and time interacting with each other to exchange energy at different scales. The transfer of energy from the largest scales, where kinetic energy is most concentrated, to smaller scales as the large structures break, is called the **direct energy cascade**. The nineteenth century was the first time scientists and engineers began to study fundamental flows theoretically and experimentally, (Prandtl, 1925; Taylor, 1932; Prandtl, 1942; Boussinesq, 1877a; Reynolds, 1894; Boussinesq, 1897; Casciola, Olivieri, Piva, et al., 1998).
Turbulence modeling aims to develop equations for computing turbulent flow by approximating the precise Navier-Stokes equations. The Reynolds-averaged Navier-Stokes equations (RANS) strategy breaks down flow variables into mean and fluctuating components through Reynolds decomposition. The Navier-Stokes equations are then applied to the Reynolds-decomposed variables and averaged to arrive at the Reynolds-stress tensor, an unknown factor that requires modeling to solve the RANS equations. The primary obstacle in closing the Navier-Stokes equations system is modeling the Reynolds-stress tensor.
The narrowing of the arteries' lumen is caused by an inflammatory disorder induced by various unhealthy behaviors and lifestyles, which is the main underlying pathological process of CVDs, known as atherosclerosis (Haverich and Boyle, 2019). (Lyras and Lee, 2021) utilized the OpenFOAM software to numerically model blood flow through different arterial segments. Several studies have been conducted on blood flow in this area. (Lopes et al., 2021) provided a comparative numerical analysis on blood flow through arterial segments using finite element and finite volume methods. Although blood is considered a non-Newtonian fluid, in some large arteries such as the aorta, where the shear rate exceeds one hundred per second, the blood flow exhibits Newtonian behavior (Pedley, 1980; Berger and Jou, 2000). Therefore, blood is considered a Newtonian fluid in such large arteries.
For providing a clear and detailed explanation for fluid flows, Navier-Stokes equations are essential when dealing with incompressible flow and forcing terms. These equations emerge from the application of Newton's second law to fluid motion, underpinned by the underlying assumption that fluid stress is a combination of a diffusing viscous term proportional to the gradient of velocity and a pressure term. In the case of incompressible flows, the density of the fluid remains the same and the velocity field has a zero divergence. The incompressible Navier-Stokes equations, which include forcing terms, can be represented in the following manner:

$$\frac{\partial \mathbf{u}}{\partial t} + (\mathbf{u} \cdot \nabla)\mathbf{u} = -\frac{1}{\rho}\nabla p + \nu \Delta \mathbf{u} + \mathbf{f}, \tag{1}$$

The velocity field is represented by u, while p represents the pressure field. The constant density is denoted by ρ, and the kinematic viscosity is represented by ν. The external force per unit mass acting on the fluid is represented by f in this formulation. This formulation is designed to incorporate the effects of external forces, such as gravity or electromagnetic forces. These external forces are particularly important for a wide range of applications in both natural and technological contexts. The preservation of mass in a flow of incompressible fluid is guaranteed by the continuity equation, which states that $\nabla . u = 0$. These equations are non-linear, and their

solutions can be complicated and even turbulent, which makes predicting fluid behavior under different circumstances both vital and challenging.

Doctoral dissertation Contributions

This research addresses the intricate interplay of laminar and turbulent flow of non-Newtonian blood through stenosed arteries, incorporating a novel hybrid composition of Cu and Al_2O_3. Furthermore, this study leverages numerical simulations, employing the Finite Difference Time Domain (FTCS) scheme in MATLAB and the OpenFOAM solver (icoFoam), to comprehensively investigate the hemodynamic behavior.
The rheological properties of blood are notably non-Newtonian, and their impact on flow dynamics becomes particularly significant in the context of arterial stenosis. The transition from laminar to turbulent flow within stenosed arteries is a critical factor influencing the progression and severity of cardiovascular diseases. The introduction of a hybrid composition, blending copper (Cu) and aluminum oxide (Al_2O_3), offers a unique avenue to influence the mechanical and thermal properties of the arterial environment. This hybrid material is expected to induce distinct fluid-structure interactions, shaping the overall hemodynamic response.
The computational approach in this study involves the application of the FTCS scheme in MATLAB for its efficiency in solving partial differential equations characterizing blood flow. Additionally, the use of the OpenFOAM solver, specifically icoFoam, provides a robust platform for the simulation of incompressible, laminar flows. The integration of these numerical methods enables a comprehensive exploration of the impact of stenosis and hybrid materials on blood flow patterns and thermal aspects in arterial conduits.
The primary objectives of this thesis are threefold: firstly, to develop and validate numerical models for simulating non-Newtonian blood flow through stenosed arteries using the FTCS scheme in MATLAB and Newtonian flow using the icoFoam solver in OpenFOAM; secondly, to modify the usual NSE into Reynolds averaged Navier Stokes equation and to implement the Prandtl mixing length, zero equation turbulence model; and thirdly, investigate the influence of stenosis on the laminar flow non-Newtonian blood flow and to explore the effects of the hybrid Cu-Al_2O_3 composition on hemodynamic and thermal characteristics within stenosed arteries.
The anticipated outcomes of this research include a deeper understanding of the fluid dynamics in stenosed arteries, especially under non-Newtonian conditions, and insights into the potential benefits or challenges introduced by the hybrid Cu-Al_2O_3 composition. The findings are expected to contribute significantly to the development of more accurate models for predicting blood flow behaviors and inspire innovative approaches for medical interventions in arterial diseases.
The structure of this thesis is organized as follows:

- In Chapter 1, a thorough approach is presented for the hybrid nano-blood flow model in an elliptical-shaped stenotic arterial segment, accounting for non-Newtonian Casson behavior and the influence of a magnetic field through Hall current. The model is simulated numerically using a finite differentiation method with a forward time central space on MATLAB, and the resultant fluid flow parameters are analyzed.

- Chapter 2 presents modifications made to the ordinary Navier-Stokes equations, where fluid motion equations are averaged over time, and flow variables

are separated into mean and fluctuating components (RANS). To describe the rheological behavior of non-Newtonian fluids, such as blood, Casson's model is utilized. The zero equation turbulence model is used to calculate turbulent viscosity directly from local flow properties without solving additional equations. The Prandtl mixing length model is used to approximate the eddy viscosity in turbulent flow. The Fast Transient Solver (FTCS) is employed to compute the results.

- In Chapter 3, the characteristics of blood as a Newtonian fluid are discussed. AutoCAD software simulates a 3D stenotic arterial segment to create an STL format. The vertices and number of cells in each direction are specified to create a structured hexahedral mesh using the `blockmesh` utility. The mesh quality is improved around the edges and walls of the artery with the help of `snappyHexMesh`. The boundary conditions are defined using `fixedValue`, `zeroGradient`, and `no-slip`. For the incompressible, laminar flow of Newtonian blood flow, simulations are performed using the `icoFoam` package. The velocity and pressure profiles are analyzed for both constant and parabolic inlet conditions.

In summary, this research endeavors to bridge the knowledge gap in the understanding of non-Newtonian blood flow through stenosed arteries, incorporating the influence of a hybrid Cu-Al_2O_3 composition. The utilization of both MATLAB and OpenFOAM provides a robust framework for numerical investigations, offering a comprehensive and insightful exploration of the hemodynamic environment within stenotic arteries.

Chapter 1

Cu-Al_2O_3-Blood Flow Through Stenotic Arteries Analysis

Overview

A numerical investigation into blood flow through constricted blood vessels holds significant importance in the medical field, especially concerning cardiovascular diseases (CVDs). The dedicated chapter analyzing unsteady axisymmetric fluid flow through elliptical-shaped stenotic arteries offers a thorough examination of blood flow dynamics within this specific context Section 1.2. The Casson fluid model is used to capture the non-Newtonian behavior of blood, while pulsatile pressure gradients Section /refsection:CassonModelPressure represent the pulsatile nature of blood flow. The Navier-Stokes equation is fundamental in studying axisymmetric flows for fluid dynamics and heat transfer Section 1.4. Moreover, adding copper (Cu) and alumina (Al_2O_3) nanoparticles to the bloodstream increases the complexity of the analysis and expands its applications to drug delivery Section 1.5 aims to understand the impact of a magnetic field on flow dynamics via the Hall current Section 1.6. After deriving relevant equations and associated conditions, dimensional partial differential equations are transformed into non-dimensional form via dimensionless transformations Section 1.7. This transformation facilitates a clearer understanding and analysis of the underlying physics. The chapter is divided into two major cases. Case 1 undergoes thorough examination using the long wavelength approximation and radial coordinate transformations to obtain a reduced set of flow equations. Section 1.7.1. Extensive analysis is conducted within this framework, elucidating the nuances of flow dynamics and heat transfer processes. Case 2 is In-progress work but has potential for future research as it disregards the long wavelength approximation. (See Section 1.7.2.) The non-dimensionalized equations result in unsteady partial differential equations, which are solved numerically using the forward time central space method in MATLAB Section 1.9. Stability analysis is conducted with a strict error threshold. Additionally, graphical representations are used to study the impact of emerging parameters in the nonlinear flow equations Section 1.10. Comparison of velocity and temperature profiles with previously published data, giving an overview of the study's findings. Finally, the chapter summarizes the analysis' findings in Section 1.11.

1.1 Introduction

Cardiovascular diseases (CVD) continue to pose a substantial burden on global health care systems, with conditions like coronary artery disease (CAD), stroke, and peripheral artery disease (PAD) contributing significantly to morbidity and mortality. Among the key pathophysiological features of these diseases is the development of arterial stenosis, characterized by the narrowing of arteries due to plaque buildup, which significantly alters blood flow patterns, leading to adverse effects such as reduced oxygen delivery to tissues and increased risk of thrombosis. Several computational approaches have been employed to study blood flow in stenosed arteries. Finite element methods (FEM), finite difference methods (FDM), and finite volume methods (FVM) are commonly used numerical techniques to solve the governing equations of fluid dynamics, such as the Navier-Stokes equations, in complex geometries typical of vascular structures. These simulations allow researchers to investigate parameters such as velocity profiles, wall shear stress, pressure gradients, and flow patterns, which are critical for understanding the biomechanical forces acting on arterial walls and their implications for disease progression (Cimmelli, Oliveri, and Pace, 2011; Supratim, 2023; Haand et al., 2022; Nadeem et al., 2023; Carvalho et al., 2020b; Sarwar et al., 2022; Vasu, Dubey, and Bég, 2019; Chakravarty and Dalal, 2018; Cavaccini et al., 2006).

Nanoparticles and hybrid nanoparticles have garnered significant attention in the field of drug delivery in medicine due to their unique properties that offer several advantages over conventional drug delivery systems (Choi and Eastman, 1995; H et al., 1993; Lee et al., 1999; Eastman et al., 2001; Mauro et al., 2009; Demir et al., 2013; Minea, 2020; De Luca et al., 2017). Firstly, nanoparticles have a high surface area-to-volume ratio, allowing for efficient drug loading and encapsulation. This enables precise control over drug release kinetics, improving therapeutic efficacy and reducing side effects. Additionally, nanoparticles can be engineered to target specific tissues or cells through surface modifications, enhancing drug delivery to the desired site while minimizing systemic exposure. In medicine, nanoparticles and hybrid nanoparticles are used as promising vehicles for therapeutic agents in drug delivery. Liposomes (Meng, Niu, and Li, 2022; Lamichhane et al., 2018; Yanrong et al., 2019; Demetzos, 2016; Daraee et al., 2016), polymeric nanoparticles (Aldosari et al., 2023; Barbieri, 2023; Pulingam et al., 2022; Xiao et al., 2022; Gao, Nicolas, and Ha-Duong, 2021), Iron oxide nanoparticles (Tatarchuk et al., 2023; Varghese, Vijay, and Dalvi, 2021; Bruschi and Toledo, 2019; Antoniac et al., 2020; Suciu et al., 2020; Huang et al., 2023), Silica nanoparticles (Sahai, Gogoi, and Ahmad, 2021; Harun et al., 2021; He et al., 2020; Najafi, Morsali, and Bozorgmehr, 2019; Connell et al., 2018; Pandey et al., 2009), Magnetic nanoparticles (Sodagar, Shakiba, and Niazmand, 2020; Zafar et al., 2022; Gul, Tzirtzilakis, and Makhanov, 2022; Pathak and Afkhami, 2023).

Copper nanoparticles have unique properties that make them particularly useful in drug delivery applications. They also exhibit inherent antimicrobial properties, which can help prevent infections in the diseased artery and promote faster healing (Tyagi, Arya, and Tyagi, 2023; Naatz et al., 2020a; Halevas and Pantazaki, 2018; Cassano et al., 2022; Naatz et al., 2020b; Mulpuru, Maurya, and Mishra, 2019). Aluminum oxide Al_2O_3 nanoparticles are a stable and inert structure that can be used for drug delivery. Due to their high surface area-to-volume ratio, they are effective in loading therapeutic agents and releasing them in a controlled manner. Moreover, these nanoparticles have shown to be highly biocompatible and have low toxicity levels, which makes them a suitable option for biomedical applications (Al_2O_3 nanoparticles for current analysis (Spivak et al., 2022; Kaushik et al., 2022; Alias et

al., 2016; Makarishcheva et al., 2022; Naatz et al., 2020b; Yerpude et al., 2022).
Hybrid nanoparticles are nanoparticles that combine different materials or functionalities and can be customized to address various challenges. A good example is the incorporation of magnetic nanoparticles into drug-loaded carriers, which enables targeted delivery using external magnetic fields. This overcomes the obstacles posed by altered blood flow patterns in stenotic arteries. Hybrid nanoparticles can also enhance the stability and circulation time of drug carriers in the bloodstream, which is crucial for effective delivery to the target site in CVD. By combining materials with complementary properties, such as polymers for stability and lipids for biocompatibility, hybrid nanoparticles can overcome limitations associated with individual components, ensuring optimal drug delivery in the presence of stenosis. Cu-Al_2O_3 hybrid nanoparticles show promise for drug delivery in stenotic arteries. They have unique properties that provide several advantages, including targeted drug delivery, stability, biocompatibility, efficient penetration, and controlled drug release. These nanoparticles have the potential to improve outcomes for patients with cardiovascular diseases (Khanduri and Sharma, 2022; Gandhi, Sharma, and Makinde, 2022; Fraser, 2023a; Sharma, Poonam, and Chamkha, 2022; Fraser, 2023b; Dolui, Bhaumik, and De, 2022).
Magnetic fields, in combination with Hall currents, offer a new way to deliver drugs in stenotic arteries where blood flow is restricted due to plaque buildup. This condition can increase the risk of cardiovascular events. The use of magnetic nanoparticles (MNPs) allows for targeted drug delivery to specific locations within the body through the application of external magnetic fields. This approach exploits the unique properties of MNPs that can be functionalized with therapeutic agents. In the case of stenotic arteries, magnetic fields can guide drug-loaded MNPs to the site of arterial narrowing, improving the effectiveness of drug delivery. Magnetic fields can be used to precisely control the localization of drug-loaded magnetic nanoparticles (MNPs), ensuring that they are delivered to the narrowed region of an artery where they are needed. The magnetic force exerted on the MNPs by Hall currents can help them overcome obstacles such as turbulent blood flow and endothelial barriers, making it easier for therapeutic agents to penetrate deeper into the arterial wall (Cimmelli, Oliveri, and Pace, 2004; Naser, Abdullah, and Talib, 2019; Fazio and Jannelli, 2020; Mok, Han, and Lee, 2020; Fazio and Jannelli, 2021; Umadevi et al., 2021; Burns, 2023; Abdullah and Ismail, 2022; Omamoke and Amos, 2023; Robison, 2023).

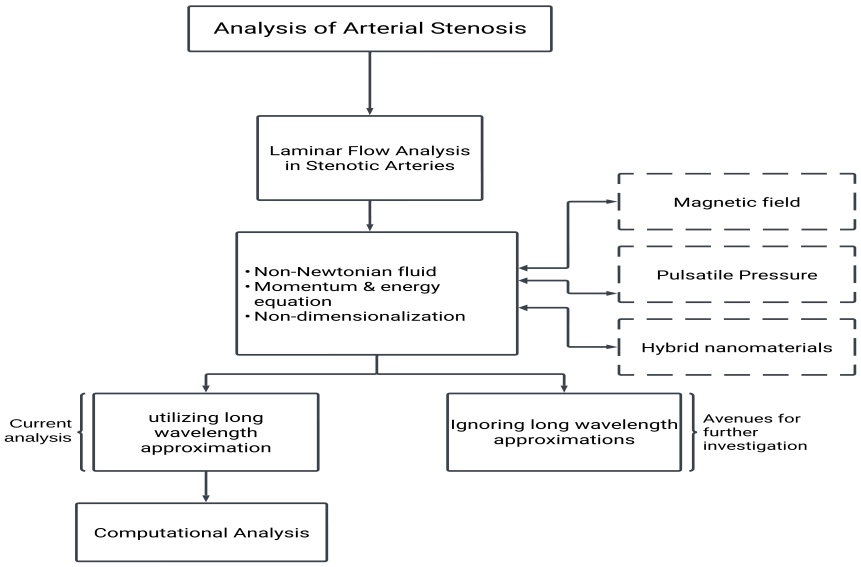

FIGURE 1.1: An overview of constricted arterial analysis.

1.2 Anatomy of stenotic flow

Modeling blood flow through a stenotic artery involves understanding the complex fluid dynamics that occur when a narrowing or blockage (stenosis) affects arterial blood flow. Blood behaves as a non-Newtonian fluid, meaning its viscosity can change under different flow conditions, which is particularly relevant in the context of arterial stenosis. The presence of stenosis alters the pressure and velocity profiles within the artery, potentially leading to turbulent flow, recirculation zones, and increased shear stress on the arterial walls. These changes are significant because they can influence the progression of cardiovascular diseases and the formation of further atherosclerotic plaques.

Blood flow through an artery with an elliptical-shaped stenosis can be modeled to understand the hemodynamic changes and can significantly alter the flow patterns, pressure distribution, and shear stress within the artery. An elliptical shaped stenosis in an artery can be described by modifying the radius of the artery R_0 along the axial direction $\widetilde{z}$ to mimic the narrowing caused by the stenosis described by the function in equation (1.1) where the narrowing using a function $\widetilde{R}(\widetilde{z})$ that varies the radius of the artery along its length l_0 and δ^* as maximum deviation from baseline.

$$\widetilde{R}(\widetilde{z}) = \begin{cases} R_0 - \delta^* sin\left(\pi\left(\frac{\widetilde{z}-\widetilde{d}}{l_0}\right)\right), & \widetilde{d} \leq \widetilde{z} \leq \widetilde{d} + l_0 \\ R_0 & otherwise. \end{cases} \tag{1.1}$$

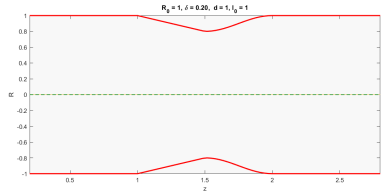

(A) Composite stenosis.

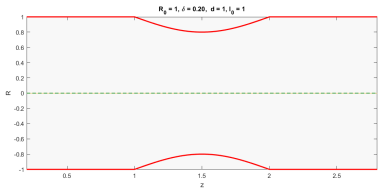

(B) Elliptical stenosis.

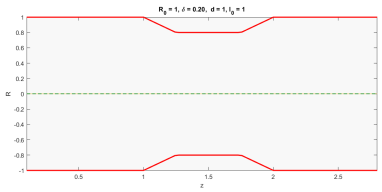

(C) Trapezoidal stenosis.

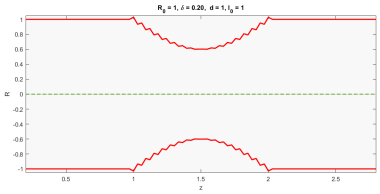

(D) Irregular stenosis.

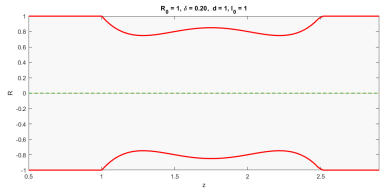

(E) Overlapping stenosis.

FIGURE 1.2: The graphic representation of different types of lesions caused by stenosis for $R = 1.0, l_0 = 1.0, \delta = 0.2, d = 1.0$.

1.3 Pulsatile dynamics of non-Newtonian blood

As a result of its complex composition, blood is considered to be non-Newtonian fluids, resulting in rheological properties like shear-thinning behavior and yield stress. While blood is viscous in capillaries, it flows more easily in larger vessels due to a decreased viscosity. In order to initiate blood flow, yield stress is required, and numerical simulation techniques can be used to understand flow patterns (Wootton and Ku, 1999; Xingting et al., 2022). As blood carries proteins and living cells suspended in plasma (Caro, 2001), understanding flow within the bloodstream is crucial to preventing vascular diseases.

The Casson model is a useful tool for modeling blood flow due to its ability to capture the non-linear behavior of blood viscosity, particularly at low shear rates where traditional Newtonian models fail. It incorporates parameters such as yield stress and Casson viscosity and can provide more accurate predictions of blood flow dynamics in various physiological and pathological conditions. The Casson model is particularly useful for describing the behavior of blood in situations where flow rates are low, such as in microcirculation or in vessels with stenosis. It provides a more accurate representation of blood flow compared to simple Newtonian models, especially at low shear rates where blood viscosity tends to increase significantly.

Applications of the Casson model include computational simulations of blood flow in biomedical engineering, hemodynamics studies, and understanding flow characteristics in diseased vessels, among others. It helps researchers and clinicians better understand the complexities of blood flow behavior, which is crucial for various medical and engineering applications.

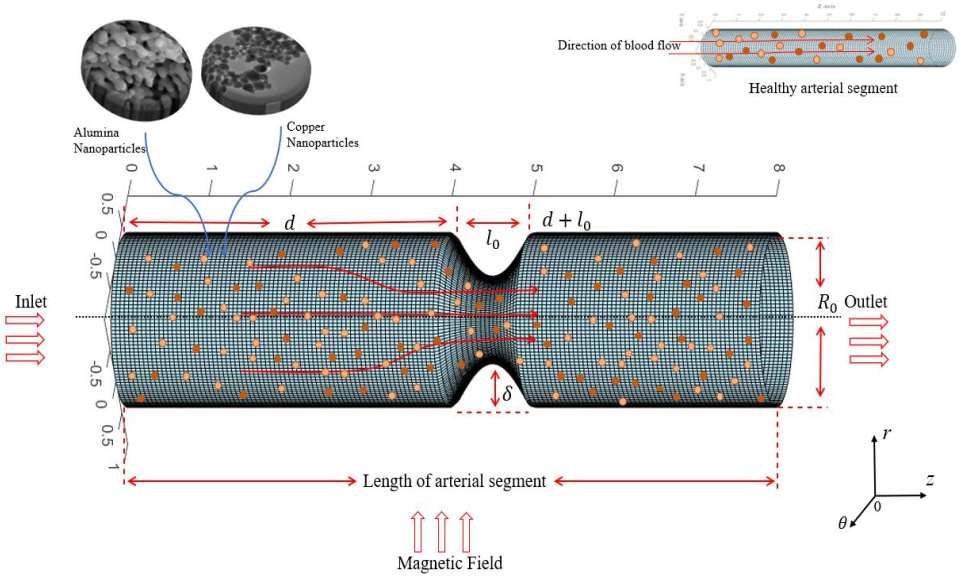

FIGURE 1.3: Model of constricted arterial lumen of radius R_0 involving non-Newtonian Cu-Al_2O_3-blood.

The Casson fluid model for incompressible fluid flows is defined by the following expression:

$$\bar{\tau}_{ij} = \begin{cases} 2(\bar{\mu}_b + \frac{\bar{P}_y}{\sqrt{2\bar{\pi}}})\bar{e}_{ij}, & \bar{\pi} > \bar{\pi}_c, \\ 2(\bar{\mu}_b + \frac{\bar{P}_y}{\sqrt{2\bar{\pi}_c}})\bar{e}_{ij}, & \bar{\pi} \leq \bar{\pi}_c. \end{cases}$$

Where $\bar{\pi} = \bar{e}_{ij} \cdot \bar{e}_{ij}$ is the product of deformation rate to itself, $\bar{\mu}_b$ is the viscosity of non-Newtonian fluid, $\bar{P}_y$ is the yield stress of fluid and $\bar{\mu}_c$ is the critical value based on non-Newtonian model. For $\bar{\pi} \leq \bar{\pi}_c$, $\bar{\tau}_{ij}$ becomes:

$$\bar{\tau}_{ij} = 2\bar{\mu}_b(1 + 1/\beta)\bar{e}_{ij}$$

$\beta = \frac{\bar{\mu}_b\sqrt{2\bar{\pi}_c}}{\bar{P}_y}$ known as Casson fluid parameter.

1.3.1 Pulsatile pressure gradient:

In the study of blood flow through narrowed arteries, using the Navier-Stokes equation (1.15) with a pulsatile pressure gradient is crucial to mimic actual cardiovascular conditions. The pulsatile nature of blood flow in arteries is due to the heart's systolic and diastolic phases. The pressure gradient in the arteries changes with each cardiac cycle. The pulsating nature of blood flow (Figure 1.4) is particularly crucial in the examination of cardiovascular diseases (CVD) because it can significantly impact the hemodynamic forces that the arterial walls experience. These forces, particularly shear stress, are recognized to have an influence on the development of ailments such as atherosclerosis, which frequently happens in narrowed regions of arteries. The pulsatile component represents the variations of the pressure curve around the steady component.

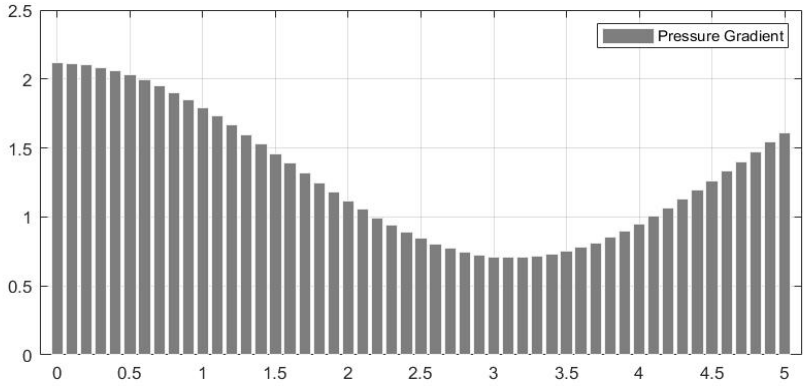

FIGURE 1.4: Pulsatile pressure gradient waveform.

The pressure gradient in Navier Stokes equation (1) is given by the following expression (Burton, 1972):

$$-\frac{\partial \widetilde{p}}{\partial \widetilde{z}} = p_0 + p_1 \cos \omega \widetilde{t}, \quad t > 0 \tag{1.2}$$

where p_0 is the amplitude of the pressure gradient representing the continuous force that drives blood through the circulatory system, even between heartbeats. p_1 is the amplitude of the pulsatile component for systolic and diastolic pressure component, $\omega = 2\pi f_p$ with f_p is the pulse frequency.

1.4 Mathematical equations governing flow

The Navier-Stokes Equations (NSE) are a set of partial differential equations that describe the motion of fluid substances such as liquids and gases. These equations arise from applying Newton's second law to fluid motion, together with the assumption that fluid stress is the sum of a diffusing viscous term (proportional to the gradient of velocity) and a pressure term. The Navier-Stokes equations are derived from the conservation and continuity equations of fluid properties. The continuity equation is derived first to establish conservation conditions. This equation is then used to conserve mass and momentum and ultimately integrated with a physical understanding of fluid characteristics to obtain the conservation equations.
When dealing with fluids in cylindrical coordinates such as in pipes, cylinders, or arteries, the NSE is expressed in terms of the radial (r), azimuthal (θ), and axial (z) components to accommodate the geometry of the system. With the suppositions that flow is incompressible, axisymmetric and non-Newtonian, the governing continuity and momentum equations are (Pontrelli, 2001; Gandhi et al., 2023):

$$\frac{\widetilde{u}}{\widetilde{r}} + \frac{\partial \widetilde{u}}{\partial \widetilde{r}} + \frac{\partial \widetilde{w}}{\partial \widetilde{z}} = 0, \tag{1.3}$$

$$\rho_{hnf}\left(\frac{\partial \widetilde{u}}{\partial \widetilde{t}} + \widetilde{u}\frac{\partial \widetilde{u}}{\partial \widetilde{r}} + \widetilde{w}\frac{\partial \widetilde{u}}{\partial \widetilde{z}}\right) = -\frac{\partial \widetilde{p}}{\partial \widetilde{r}} + \mu_{hnf}\left(1 + \frac{1}{\beta}\right)\left[\frac{\partial^2 \widetilde{u}}{\partial \widetilde{r}^2} + \frac{1}{\widetilde{r}}\frac{\partial \widetilde{u}}{\partial \widetilde{r}} + \frac{\partial^2 \widetilde{u}}{\partial \widetilde{z}^2} - \frac{\widetilde{u}}{\widetilde{r}^2}\right], \tag{1.4}$$

$$\rho_{hnf}\left(\frac{\partial \widetilde{w}}{\partial \widetilde{t}} + \widetilde{u}\frac{\partial \widetilde{w}}{\partial \widetilde{r}} + \widetilde{w}\frac{\partial \widetilde{w}}{\partial \widetilde{z}}\right) = -\frac{\partial \widetilde{p}}{\partial \widetilde{z}} + \mu_{hnf}\left(1 + \frac{1}{\beta}\right)\left[\frac{\partial^2 \widetilde{w}}{\partial \widetilde{r}^2} + \frac{1}{\widetilde{r}}\frac{\partial \widetilde{w}}{\partial \widetilde{r}} + \frac{\partial^2 \widetilde{w}}{\partial \widetilde{z}^2}\right], \tag{1.5}$$

Energy equation

The energy equation for the analysis of the Casson flow model is (Farooq et al., 2021):

$$(\rho C_p)_{hnf}\left(\frac{\partial \widetilde{T}}{\partial \widetilde{t}}+\widetilde{u}\frac{\partial \widetilde{T}}{\partial \widetilde{r}}+\widetilde{w}\frac{\partial \widetilde{T}}{\partial \widetilde{z}}\right)=K_{hnf}\left[\frac{\partial^2 \widetilde{T}}{\partial \widetilde{r}^2}+\frac{1}{\widetilde{r}}\frac{\partial \widetilde{T}}{\partial \widetilde{r}}+\frac{\partial^2 \widetilde{T}}{\partial \widetilde{z}^2}\right]+2\mu_{hnf}\left(1+\frac{1}{\beta}\right)\left[\left(\frac{\partial \widetilde{u}}{\partial \widetilde{r}}\right)^2+\left(\frac{\widetilde{u}}{\widetilde{r}}\right)^2+\left(\frac{\partial \widetilde{w}}{\partial \widetilde{z}}\right)^2+\frac{1}{2}\left(\frac{\partial \widetilde{u}}{\partial \widetilde{z}}+\frac{\partial \widetilde{w}}{\partial \widetilde{r}}\right)^2\right], \quad (1.6)$$

In the above equations,$(\widetilde{u},\widetilde{w})$, $\widetilde{t}$, $\widetilde{T}$, $\widetilde{p}$ are correspondingly dimensional velocities along radial and axial directions, time, temperature and pressure. ρ_{hnf}, μ_{hnf}, σ_{hnf}, $(C_p)_{hnf}$ and κ_{hnf} are respectively density, dynamic viscosity, electrical conductivity, specific heat capacity and thermal conductivity for hybrid nanofluid.

1.4.1 Initial & boundary conditions

Fluid flow can be influenced by the presence of solid surfaces, which can impede, redirect, or accelerate the flow. Thus, it is essential to understand how solid surfaces influence flow.

Initial conditions

In the context of blood flow through a stenosed artery, the initial velocity is zero, implying that the blood is at rest $\widetilde{t}=0$ within the narrowed artery at the beginning. As the heart pumps, the pressure gradient causes the blood to start flowing and accelerate from its initial state. The initial condition of $\widetilde{T}=0$ in equation (1.7) is often set for the non-dimensional temperature to standardize the model and facilitate the comparison of results. This approach allows the incorporation of temperature variations relative to the average body temperature (36°C) and simplifies the mathematical treatment of heat transfer and fluid dynamics within the arteries. This sets a baseline for observing the evolution of the flow and temperature fields over time.

$$\widetilde{w}=0, \quad \widetilde{T}=0, \qquad at\ \widetilde{t}=0. \quad (1.7)$$

Wall conditions

The boundary conditions specify the behavior of the flow at the boundaries of the domain as provided in equation (1.8). At the axis (centerline) of the artery ($\widetilde{r}=0$), the radial gradient of velocity and temperature are both zero. Physically, this indicates that at the centerline of the artery (axis), there is no radial flow (symmetry in the flow) and no radial temperature gradient, meaning the temperature is uniform across this axis.
At the wall of the artery ($\widetilde{r}=\widetilde{R}$), where $\widetilde{R}$ is the value of the radius, the velocity gradient is set to zero, which is a no-slip condition typical for viscous fluids at solid boundaries as evident in equation (1.8). Essentially, it stipulates that fluid molecules in direct contact with a solid surface do not slip or move relative to it. Instead, they stick to it due to the viscous effects and move at the same rate as the solid boundary. As fluid flows, the layer closest to the surface slows down because of the viscous forces between the fluid layers. This causes the next layer to slow down as well, and so on. The region of the flow that is adjacent to the wall and where viscous effects (and velocity gradients) are significant is called the **boundary layer**. The

temperature $\widetilde{T}$ is set to the arterial wall temperature $\widetilde{T}_w$, suggesting that the wall is maintained at a constant temperature (Gandhi et al., 2023).

$$\begin{aligned} &\frac{\partial \widetilde{w}}{\partial \widetilde{r}} = 0, \quad \frac{\partial \widetilde{T}}{\partial \widetilde{r}} = 0, \qquad at\ \widetilde{r} = 0, \\ &\widetilde{w} = 0, \quad \widetilde{T} = \widetilde{T}_w, \qquad at\ \widetilde{r} = \widetilde{R}. \end{aligned} \tag{1.8}$$

1.5 Hybrid composition of Cu and Al_2O_3 nanoparticles:

Copper (Cu) and alumina (Al_2O_3) nanoparticles show unique properties that make them promising candidates for drug delivery in medicine. These nanoparticles are highly versatile in drug delivery applications due to their adjustable surface properties and high surface area-to-volume ratios, allowing for precise dosage regulation and enhanced therapeutic efficacy. One of their significant advantages is their inherent biocompatibility and low toxicity profile, which are crucial factors in ensuring the safe and effective delivery of therapeutic agents within the human body. Copper (Cu) and alumina (Al_2O_3) nanoparticles provide a versatile platform for drug encapsulation and controlled release, with potential applications in targeted therapy and tissue engineering. Due to their high surface area-to-volume ratio, these nanoparticles allow for efficient drug loading. Additionally, their chemical stability ensures long-term viability in biological environments. Cu-Al_2O_3 nanoparticles combine copper's antimicrobial properties and potential synergies with therapeutic agents with alumina's high surface area, inertness, and ability to protect encapsulated drugs, allowing for controlled release kinetics and prolonged circulation times in the bloodstream.

The concentration of nanoparticles in drug delivery is a critical factor that determines the effectiveness and safety of the delivery system. If the concentration is too low, the therapeutic benefits may not be sufficient. On the other hand, if the concentration is too high, it may cause adverse effects or toxicity. In many studies, volume fractions of nanoparticles typically range from as low as 0.1% to as high as 10% or more of the total volume. Typically, the volume fraction of copper nanoparticles falls within the lower end of the spectrum, ranging from 0.1% to 5%, and for Al_2O_3, the volume fraction commonly falls within the range of 0.1% to 10%.

For the current analysis, the volume fraction of 0.025 for both Cu and Al_2O_3 is considered which indicates that for every unit volume of the ordinary liquid (blood), 0.025 units of volume are occupied by Cu and Al_2O_3 nanoparticles combined or 2.5% of the total volume being occupied by the nanoparticles.

The thermophysical features, i.e., density, thermal conductivity, electrical conductivity, and specific heat for base fluid (blood), copper (Cu) and aluminum oxide (Al_2O_3) are given in the Table 1.1 and the relation between both nanofluids are mentioned in Table 1.2 and Table 1.3. μ_f, σ_f, $(C_p)_f$, ρ_f and κ_f are viscosity, electrical conductivity, specific heat capacity, density and thermal conductivity of the base fluid. (ϕ_1, ϕ_2) are nanoparticle volume fraction. s_1, s_2 and b_f denotes first, second particles and base fluid.

TABLE 1.1: Thermophysical features for Cu, Al_2O_3 and blood (Ghadikolaei et al., 2018).

Thermophysical Properties	Cu	Al_2O_3	Human Blood
Density kgm^{-3}	8933	3970	1063
Specific thermal capacity $JKg^{-1}K^{-1}$	385	765	3594
Thermal conductivity $Wm^{-1}K^{-1}$	401	40	0.492
Electrical conductivity Ωm^{-1}	59.6×10^6	35×10^6	6.67×10^{-1}

TABLE 1.2: properties of nanofluid (Ghadikolaei et al., 2018).

Properties	Nanofluid
Dynamic viscosity	$\mu_{nf} = \frac{\mu_f}{(1-\phi)^{2.5}}$
Density	$\rho_{nf} = (1-\phi)\rho_f - \phi\rho_s$
Thermal conductivity	$\kappa_{nf} = \kappa_f \left(\frac{\kappa_s + 2\kappa_f - 2\phi(\kappa_f - \kappa_s)}{\kappa_s + 2\kappa_f + \phi(\kappa_f - \kappa_{s)}} \right)$
Electrical conductivity	$\sigma_{nf} = \sigma_f \left(\frac{2\sigma_f + \sigma_s - 2\phi(\sigma_f - \sigma_s)}{2\sigma_f + \sigma_s + \phi(\sigma_f - \sigma_s)} \right)$
Heat capacity	$(\rho C_p)_{nf} = (1-\phi)(\rho C_p)_f - \phi(\rho C_p)_s$

TABLE 1.3: Thermo-physical properties of hybrid nanofluid (Ghadikolaei et al., 2018),(Pak and Cho, 1998),(Xuan and Roetzel, 2000),(Einstein, 1956),(Maxwell, 1881).

Properties	Hybrid nanofluid
Dynamic viscosity	$\mu_{hnf} = \frac{\mu_f}{(1-\phi_1)^{2.5}(1-\phi_2)^{2.5}}$
Density	$\rho_{hnf} = [(1-\phi_2)((1-\phi_1)\rho_f + \phi_1\rho_1)] + \phi_2\rho_2$
Thermal conductivity	$\frac{\kappa_{hnf}}{\kappa_{bf}} = \left(\frac{(\kappa_{s2} + 2\kappa_{bf}) - 2\phi_2(\kappa_{bf} - \kappa_{s2})}{(\kappa_{s2} + 2\kappa_{bf}) + \phi_2(\kappa_{bf} - \kappa_{s2})} \right)$, $\frac{\kappa_{bf}}{\kappa_f} = \left(\frac{(\kappa_{s1} + 2\kappa_f) - 2\phi_1(\kappa_f - \kappa_{s1})}{(\kappa_{s1} + 2\kappa_{bf}) + \phi_1(\kappa_f - \kappa_{s1})} \right)$
Electrical conductivity	$\sigma_{hnf} = \sigma_{bf} \left(\frac{2\sigma_{bf} + \sigma_{s2} - 2\phi_2(\sigma_{bf} - \sigma_{s2})}{2\sigma_{bf} + \sigma_{s2} + \phi_2(\sigma_{bf} - \sigma_{s2})} \right)$, $\sigma_{bf} = \sigma_f \left(\frac{2\sigma_f + \sigma_{s1} - 2\phi_1(\sigma_f - \sigma_{s1})}{2\sigma_f + \sigma_{s1} + \phi_1(\sigma_f - \sigma_{s1})} \right)$
Heat capacity	$(\rho C_p)_{hnf} = (\rho C_p)_f(1-\phi_2)\left((1-\phi_1) + \phi_1 \frac{(\rho C_p)_{s1}}{(\rho C_p)_f} \right) + \phi_2(\rho C_p)_{s2}$

1.6 Inclusion of magnetic field

The Hall effect arises when a conductive fluid, such as blood, flows through an applied magnetic field perpendicular to its motion, resulting in the generation of an electric field perpendicular to both the fluid flow direction and the magnetic field

lines. This phenomenon, known as the Hall current, induces additional forces on the fluid, influencing its behavior and altering flow dynamics within the artery. The interaction between blood flow and magnetic fields can facilitate targeted drug delivery and therapeutic interventions within stenotic arteries. Magnetic nanoparticles, functionalized with therapeutic agents or imaging contrast agents, can be introduced into the bloodstream and manipulated using applied magnetic fields to localize them within specific regions of interest, such as the stenotic lesion. Enhancing efficacy and retention of nanoparticles within stenosis by exploiting Hall current phenomenon improves drug delivery and imaging.
In the presence of magnetic field $\boldsymbol{B}$ with current density $\boldsymbol{J}$ the Lorentz force acting on the non-Newtonian blood is given by $\boldsymbol{J} \times \boldsymbol{B}$. According to the Ohm's law, the current density is related to the electric field $\boldsymbol{E}$ and conductivity σ as:

$$\boldsymbol{J} + \frac{\omega_e \tau_e}{\beta_0}(\boldsymbol{J} \times \boldsymbol{B}) = \sigma\bigg(\boldsymbol{E} + u + \boldsymbol{B} + \frac{\nabla P_e}{e\eta_e}\bigg).$$

Introducing Gauss's law of magnetism ($\nabla \cdot \boldsymbol{B} = 0$) and ($\boldsymbol{B} = \boldsymbol{B_0 J}$) be the applied magnetic field and assuming P_e, electron pressure is constant and $E = 0$ then we have:

$$\boldsymbol{J} + \frac{m}{\beta_0}(\boldsymbol{J} \times \boldsymbol{B}) = \sigma\bigg(u \times \boldsymbol{B}\bigg).$$

where $m = \omega_e \tau_e$ is the Hall parameter. By using the velocity and current density along axial and radial coordinates, the above expressions for magnetic field can be derived:

$$\boldsymbol{J_r} = \frac{\sigma\beta_0}{1+m^2}(mw + u), \quad \boldsymbol{J_z} = \frac{\sigma\beta_0}{1+m^2}(mu - w).$$

As a result, momentum and energy are as follows:

$$\rho_{hnf}\bigg(\frac{\partial \widetilde{u}}{\partial \widetilde{t}} + \widetilde{u}\frac{\partial \widetilde{u}}{\partial \widetilde{r}} + \widetilde{w}\frac{\partial \widetilde{u}}{\partial \widetilde{z}}\bigg) = -\frac{\partial \widetilde{p}}{\partial \widetilde{r}} + \frac{\sigma_{hnf}\beta_0^2}{(m^2+1)}(\widetilde{u} + m\widetilde{w}) + \mu_{hnf}\bigg(1 + \frac{1}{\beta}\bigg)\bigg[\frac{\partial^2 \widetilde{u}}{\partial \widetilde{r}^2} + \frac{1}{\widetilde{r}}\frac{\partial \widetilde{u}}{\partial \widetilde{r}} + \frac{\partial^2 \widetilde{u}}{\partial \widetilde{z}^2} - \frac{\widetilde{u}}{\widetilde{r}^2}\bigg], \quad (1.9)$$

$$\rho_{hnf}\bigg(\frac{\partial \widetilde{w}}{\partial \widetilde{t}} + \widetilde{u}\frac{\partial \widetilde{w}}{\partial \widetilde{r}} + \widetilde{w}\frac{\partial \widetilde{w}}{\partial \widetilde{z}}\bigg) = -\frac{\partial \widetilde{p}}{\partial \widetilde{z}} + \frac{\sigma_{hnf}\beta_0^2}{(m^2+1)}(\widetilde{w} - m\widetilde{u}) + \mu_{hnf}\bigg(1 + \frac{1}{\beta}\bigg)\bigg[\frac{\partial^2 \widetilde{w}}{\partial \widetilde{r}^2} + \frac{1}{\widetilde{r}}\frac{\partial \widetilde{w}}{\partial \widetilde{r}} + \frac{\partial^2 \widetilde{w}}{\partial \widetilde{z}^2}\bigg], \quad (1.10)$$

$$(\rho C_p)_{hnf}\bigg(\frac{\partial \widetilde{T}}{\partial \widetilde{t}} + \widetilde{u}\frac{\partial \widetilde{T}}{\partial \widetilde{r}} + \widetilde{w}\frac{\partial \widetilde{T}}{\partial \widetilde{z}}\bigg) = K_{hnf}\bigg[\frac{\partial^2 \widetilde{T}}{\partial \widetilde{r}^2} + \frac{1}{\widetilde{r}}\frac{\partial \widetilde{T}}{\partial \widetilde{r}} + \frac{\partial^2 \widetilde{T}}{\partial \widetilde{z}^2}\bigg] + 2\mu_{hnf}\bigg(1 + \frac{1}{\beta}\bigg)\bigg[\bigg(\frac{\partial \widetilde{u}}{\partial \widetilde{r}}\bigg)^2 + \bigg(\frac{\widetilde{u}}{\widetilde{r}}\bigg)^2 + \bigg(\frac{\partial \widetilde{w}}{\partial \widetilde{z}}\bigg)^2 + \frac{1}{2}\bigg(\frac{\partial \widetilde{u}}{\partial \widetilde{z}} + \frac{\partial \widetilde{w}}{\partial \widetilde{r}}\bigg)^2\bigg] + \frac{\sigma_{hnf}\beta_0^2}{(m^2+1)}(\widetilde{w} - m\widetilde{u})^2 \quad (1.11)$$

1.7 Non-dimensionalization

Nondimensionalization or scaling analysis involves stripping units of measurement from equations that depict physical phenomena, such as fluid flow. This approach aids in removing redundancy and affords us a clearer and more universal comprehension of the core behaviors of the system. Governing nonlinear set of flow equations (1.3), (1.9)-(1.11) along with boundary conditions (1.8) needs to be transformed via a suitable set of scaling variables against characteristic system dimensions, these transformations strip away units, affording a dimensionless framework that simplifies analysis and computation.

$$r=\frac{\widetilde{r}}{R_0},\quad z=\frac{\widetilde{z}}{l_0},\quad t=\frac{u_0\widetilde{t}}{R_0},\quad R=\frac{\widetilde{R}}{R_0},\quad d=\frac{\widetilde{d}}{l_0},\quad u=\frac{l_0\widetilde{u}}{\delta^* u_0},\quad w=\frac{\widetilde{w}}{u_0},$$

$$\theta=\frac{\widetilde{T}-\widetilde{T}_1}{\widetilde{T}_w-\widetilde{T}_1},\quad p=\frac{R_0^2\widetilde{p}}{u_0 l_0 \mu_0},\quad Re=\frac{R_0\rho_f u_0}{\mu_f},\quad Pr=\frac{c_p\mu_f}{\kappa_f},\quad \delta=\frac{\delta*}{R_0},\quad \epsilon=\frac{R_0}{l_0},$$

$$M^2=\frac{\sigma_f R_0^2\beta_0^2}{\mu_f},\quad Ec=\frac{u_0^2}{C_p(\widetilde{T}_w-\widetilde{T}_1)}. \tag{1.12}$$

Here, (u,w) are dimensionless velocities, (r,z) are dimensional radial and axial axis, t is dimensionless time, θ is dimensionless temperature, δ is dimensionless stenosis severity u_0 is reference velocity, T_w is wall temperature, l_0 is stenosis length, R_0 is the radius of artery and ϵ is vessel aspect ratio. Re is the Reynolds number, M is the Hartmann number, Pr is the Prandtl number and Ec is the Eckert number. This approach reveals key dimensionless groups—like Reynolds and Prandtl numbers—that encapsulate the essence of the flow, such as the relative importance of inertial to viscous forces, or thermal to momentum diffusivity. Utilizing equation (1.12), yields:

$$\delta\frac{u}{r}+\delta\frac{\partial u}{\partial r}+\frac{\partial w}{\partial z}=0, \tag{1.13}$$

$$\delta\epsilon^2 Re\frac{\rho_{hnf}}{\rho_f}\left(\frac{\partial u}{\partial t}+\delta\epsilon u\frac{\partial u}{\partial r}+\epsilon w\frac{\partial u}{\partial z}\right)=-\frac{\partial p}{\partial r}+\delta\epsilon^2 Re\frac{\rho_{hnf}}{\rho_f}\nu_{hnf}\left(1+\frac{1}{\beta}\right)\left[\frac{\partial^2 u}{\partial r^2}+\frac{1}{r}\frac{\partial u}{\partial r}\right.$$
$$\left.+\epsilon^2\frac{\partial^2 u}{\partial z^2}-\frac{u}{r}\right]+\frac{\epsilon^2 Re}{\rho_f}\frac{l_0\sigma_{hnf}\beta_0^2}{u_0(m^2+1)}(\delta\epsilon u+mw), \tag{1.14}$$

$$\frac{\rho_{hnf}}{\rho_f}\left(\frac{\partial w}{\partial t}+\delta\epsilon u\frac{\partial w}{\partial r}+\epsilon w\frac{\partial w}{\partial z}\right)=-\frac{1}{Re}\frac{\partial p}{\partial z}+\frac{\mu_{hnf}}{\mu_f}\frac{1}{Re}\left(1+\frac{1}{\beta}\right)\left[\frac{\partial^2 w}{\partial r^2}+\right.$$
$$\left.\frac{1}{r}\frac{\partial w}{\partial r}+\epsilon^2\frac{\partial^2 w}{\partial z^2}\right]+\frac{\sigma_{hnf}M^2}{\sigma_f Re(m^2+1)}(w-m\delta\epsilon u), \tag{1.15}$$

$$\frac{\partial\theta}{\partial t}+\delta\epsilon u\frac{\partial\theta}{\partial r}+\epsilon w\frac{\partial\theta}{\partial z}=\left(\frac{\kappa}{\rho C_p}\right)_{hnf}\frac{1}{u_0R_0}\left[\frac{\partial^2\theta}{\partial r^2}+\frac{1}{r}\frac{\partial\theta}{\partial r}+\epsilon^2\frac{\partial^2\theta}{\partial z^2}\right]+\left(\frac{\mu}{\rho C_p}\right)_{hnf}$$
$$\times\left(1+\frac{1}{\beta}\right)\frac{2u_0}{R_0(\bar{T}_w-\bar{T}_1)}\left[\delta^2\epsilon^2\left(\frac{\partial u}{\partial r}\right)^2+\delta^2\epsilon^2\left(\frac{u}{r}\right)^2+\epsilon^2\left(\frac{\partial w}{\partial z}\right)^2+\frac{\delta^2\epsilon^2}{2}\left(\frac{\partial u}{\partial z}\right)^2+\right.$$
$$\left.\frac{1}{2}\left(\frac{\partial w}{\partial r}\right)^2+\frac{\delta^2\epsilon^2u_0^2}{l_0^2}\frac{\partial w}{\partial r}\frac{\partial u}{\partial z}\right], \quad (1.16)$$

and dimensionless boundary conditions are:

$$w=0,\quad \theta=0,\qquad at\quad t=0,$$

$$\frac{\partial w}{\partial r}=0,\quad \frac{\partial\theta}{\partial r}=0,\qquad at\ r=0,$$
$$w=0,\quad \theta=1,\qquad at\ r=R. \quad (1.17)$$

By employing dimensional parameters provided in equation (1.12) in pressure gradient expression (1.2)

$$-\frac{\partial p}{\partial z}=A_0\left(1+e\cos c_1t\right) \quad (1.18)$$

where: $A_0=p_0/\mu_0u_0$, $A_1=p_1/\mu_0u_0$, $e=A_1/A_0$ and $c_1=a\pi f_pR_0/u_0$.

1.7.1 Case 1: Long wavelength approximation

The long-wavelength approximation is a widely used technique to study fluid dynamics near a solid boundary. By simplifying the complex equations that govern fluid motion, the long-wavelength approximation provides insight into the behavior of fluids in close proximity to solid boundaries. In certain situations, the assumption is commonly utilized in conjunction with linearized equations. In mathematical terms, it can be expressed as $\delta << 1$, which indicates that the characteristic length scale of the flow is much smaller than other relevant length scales in the system. Meanwhile, the degree of nonlinearity in the equations describing the flow is characterized by ϵ and $\epsilon=O(1)$, which means that the nonlinear terms in the equations are significant, they cannot be ignored or neglected, and certain terms in the equations are of the same order of magnitude as ϵ and thus relatively small. On the other hand, in weakly nonlinear scenarios, the nonlinearity is not significant, and higher-order nonlinear terms can be neglected, allowing for linearization. By making use of the long wavelength approximation, the flow equation can be simplified to:

$$\frac{\partial w}{\partial z}=0, \quad (1.19)$$

$$\frac{\partial p}{\partial r}=0, \quad (1.20)$$

$$\frac{\partial w}{\partial t}=\frac{\rho_f}{\rho_{hnf}}\frac{1}{Re}\left[-\frac{\partial p}{\partial z}+\frac{\mu_{hnf}}{\mu_f}\left(1+\frac{1}{\beta}\right)\left(\frac{\partial^2w}{\partial r^2}+\frac{1}{r}\frac{\partial w}{\partial r}\right)+\frac{M^2}{(m^2+1)}\frac{\sigma_{hnf}}{\sigma_f}w\right], \quad (1.21)$$

$$\frac{\partial\theta}{\partial t}=\frac{(\rho C_p)_f}{(\rho C_p)_{hnf}}\left[\frac{\kappa_{hnf}}{\kappa_f}\frac{1}{RePr}\left(\frac{\partial^2\theta}{\partial r^2}+\frac{1}{r}\frac{\partial\theta}{\partial r}\right)+\left(1+\frac{1}{\beta}\right)\frac{\mu_{hnf}}{\mu_f}\frac{Ec}{Re}\left(\frac{\partial w}{\partial r}\right)^2\right]. \tag{1.22}$$

The above equations (1.19)-(1.22) are a dimensionless set of flow equations with equation (1.17) as a unitless boundary condition. Importing dimensionless expression (1.18) for pressure gradient in axial direction in equation (1.21) for axial component of velocity:

$$\frac{\partial w}{\partial t}=\frac{\rho_f}{\rho_{hnf}}\frac{1}{Re}\left[A_0\left(1+e\cos(c_1t)\right)+\frac{\mu_{hnf}}{\mu_f}\left(1+\frac{1}{\beta}\right)\left(\frac{\partial^2 w}{\partial r^2}+\frac{1}{r}\frac{\partial w}{\partial r}\right)+\frac{M^2}{(m^2+1)}\frac{\sigma_{hnf}}{\sigma_f}w\right] \tag{1.23}$$

.

Radial coordinate transformations:

The radial coordinate transformations involve expressing the radial distance from the centerline of the artery in terms of a normalized variable $x = r/R(z)$. Radial coordinate transformations are useful in simplifying the mathematical formulation of flow equations, especially in situations where there are complex geometries like in stenotic arteries. By using a normalized variable, represented by x, which indicates the ratio of the radial distance to the local stenotic function, the flow equations can be transformed into a more manageable form that is easier to analyze and interpret. The set of equations (1.17), (1.22) and (1.23) becomes:

$$\frac{\partial w}{\partial t}=\frac{\rho_f}{\rho_{hnf}}\frac{1}{Re}\left[A_0\left(1+e\cos(c_1t)\right)+\frac{\mu_{hnf}}{\mu_f}\frac{1}{R(z)^2}\left(1+\frac{1}{\beta}\right)\left(\frac{\partial^2 w}{\partial x^2}+\frac{1}{x}\frac{\partial w}{\partial x}\right)+\frac{M^2}{(m^2+1)}\frac{\sigma_{hnf}}{\sigma_f}w\right], \tag{1.24}$$

$$\frac{\partial\theta}{\partial t}=\frac{(\rho C_p)_f}{(\rho C_p)_{hnf}}\left[\frac{\kappa_{hnf}}{\kappa_f}\frac{1}{RePr}\frac{1}{R(z)^2}\left(\frac{\partial^2\theta}{\partial x^2}+\frac{1}{x}\frac{\partial\theta}{\partial x}\right)+\left(1+\frac{1}{\beta}\right)\frac{\mu_{hnf}}{\mu_f}\frac{Ec}{Re}\frac{1}{R(z)^2}\left(\frac{\partial w}{\partial x}\right)^2\right], \tag{1.25}$$

and associated boundary conditions are:

$$\begin{aligned} &w(x,0)=0, \quad \theta(x,0)=0, \qquad at \quad t=0,\\ &\frac{\partial w(0,t)}{\partial x}=0, \quad \frac{\partial\theta(0,t)}{\partial x}=0, \qquad at \ x=0,\\ &w(1,t)=0, \quad \theta(1,t)=1, \qquad at \ x=1. \end{aligned} \tag{1.26}$$

And dimensionless form of equation (1.1), illustrating the elliptical stenosis for the present analysis:

$$R(z)=\begin{cases}1-\delta sin\left(\pi\left(z-d\right)\right), & d\le z\le d+1\\ 1 & otherwise.\end{cases} \tag{1.27}$$

In the above equations (1.24)-(1.27), e is the ratio of A_1 to A_0, A_1 is the pulsatile component of pressure component, A_0 is the average pressure, c_1 is frequency parameter.

1.7.2 Case 2: Disregarding long wavelength approximation

In the pursuit of comprehensively exploring the dynamics of blood flow through stenotic arteries, this section remains an intriguing avenue for future investigation. Unlike the completed study detailed in section 1.7.1, where long wavelength approximation was applied to simplify the dimensional partial differential equations governing the flow, this section diverges by intentionally omitting this approximation. Instead, intricate complexities are chosen for the original equations (1.13)-(1.16), seeking to capture nuances that may have been overlooked in the simplified framework. While radial coordinate transformations have been employed to facilitate analysis, the omission of long wavelength approximation presents a distinct challenge, offering a more rigorous examination of the system's behavior. By deferring the resolution of section 1.7.2 to future inquiry, potential insights into blood flow dynamics could be gained that could refine the understanding and inform further development.
Equations (1.13)-(1.16) can be re-written as:

$$\delta\left(\frac{u}{r}+\frac{\partial u}{\partial r}\right)+\frac{\partial w}{\partial z}=0, \tag{1.28}$$

$$\frac{\partial u}{\partial t}+\delta\epsilon u\frac{\partial u}{\partial r}+\epsilon w\frac{\partial u}{\partial z}=\frac{1}{\delta\epsilon^2 Re}\frac{\rho_f}{\rho_{hnf}}\left[-\frac{\partial p}{\partial r}+\delta\epsilon^2 Re\frac{\mu_{hnf}}{\rho_f}\left(1+\frac{1}{\beta}\right)\left(\frac{\partial^2 u}{\partial r^2}+\frac{1}{r}\frac{\partial u}{\partial r}+\epsilon^2\frac{\partial^2 u}{\partial z^2}-\frac{u}{r}\right)+\frac{l_0\epsilon^2 Re\sigma_{hnf}\beta_0^2}{u_0\rho_f(m^2+1)}(\delta\epsilon u+mw)\right], \tag{1.29}$$

$$\frac{\partial w}{\partial t}+\delta\epsilon u\frac{\partial w}{\partial r}+\epsilon w\frac{\partial w}{\partial z}=\frac{\rho_f}{Re\rho_{hnf}}\left[-\frac{\partial p}{\partial z}+\frac{\mu_{hnf}}{\mu_f}\left(1+\frac{1}{\beta}\right)\left(\frac{\partial^2 w}{\partial r^2}+\frac{1}{r}\frac{\partial w}{\partial r}+\epsilon^2\frac{\partial^2 w}{\partial z^2}\right)+\frac{\sigma_{hnf}M^2}{\sigma_f(m^2+1)}(w-m\delta\epsilon u)\right], \tag{1.30}$$

$$\frac{\partial\theta}{\partial t}+\delta\epsilon u\frac{\partial\theta}{\partial r}+\epsilon w\frac{\partial\theta}{\partial z}=\frac{\kappa_{hnf}(\rho C_p)_f}{\kappa_f(\rho C_p)_{hnf}RePr}\left[\frac{\partial^2\theta}{\partial r^2}+\frac{2}{r}\frac{\partial\theta}{\partial r}+\epsilon^2\frac{\partial^2\theta}{\partial z^2}\right]+\frac{2Ec(\rho C_p)_f}{Re(\rho C_p)_{hnf}}\left(1+\frac{1}{\beta}\right)\left[\delta^2\epsilon^2\left(\frac{\partial u}{\partial r}\right)^2+\delta^2\epsilon^2\left(\frac{u}{r}\right)^2+\epsilon^2\left(\frac{\partial w}{\partial z}\right)^2+\frac{\delta^2\epsilon^2}{2}\left(\frac{\partial u}{\partial z}\right)^2+\frac{1}{2}\left(\frac{\partial w}{\partial r}\right)^2+\frac{\delta^2\epsilon^2 u_0^2}{l_0^2}\frac{\partial w}{\partial r}\frac{\partial u}{\partial z}\right], \tag{1.31}$$

Radial coordinate transformations:

Using $(x = r/R(z))$, dimensionless continuity equation (1.28) will take the form:

$$\frac{\delta}{R(z)}\left(\frac{u}{x}+\frac{\partial u}{\partial x}\right)+\frac{\partial w}{\partial z}-\frac{x}{R(z)}\frac{\partial w}{\partial x}\frac{\partial R(z)}{\partial z}=0, \tag{1.32}$$

momentum profile in the radial direction (1.29):

$$\frac{\partial u}{\partial t}+\delta\epsilon\frac{u}{R(z)}\frac{\partial u}{\partial x}+\epsilon w\frac{\partial u}{\partial z}-\frac{\epsilon x}{R(z)}w\frac{\partial u}{\partial x}\frac{\partial R}{\partial z}=\frac{\rho_f}{\rho_{hnf}\delta\epsilon^2 Re}\Bigg[-\frac{\partial p}{\partial r}+\frac{\delta\epsilon^2 Re\rho_{hnf}\nu_{hnf}}{\rho_f}\times$$
$$\left(1+\frac{1}{\beta}\right)\times\left\{\frac{1}{R(z)^2}\frac{\partial^2 u}{\partial x^2}+\frac{1}{xR(z)^2}\frac{\partial u}{\partial x}+\epsilon^2\left(\frac{\partial^2 u}{\partial z^2}-\frac{2x}{R(z)}\frac{\partial R}{\partial z}\frac{\partial^2 u}{\partial x\partial z}-\frac{x}{R(z)}\frac{\partial u}{\partial x}\frac{\partial^2 R}{\partial z^2}+\right.\right.$$
$$\left.\left.\frac{2x}{R(z)^2}\left(\frac{\partial R}{\partial z}\right)^2\frac{\partial u}{\partial x}-\left(\frac{x}{R(z)}\right)^2\frac{\partial R}{\partial x}\frac{\partial^2 u}{\partial x^2}\right)-\frac{u}{xR(z)}\right\}+\frac{\epsilon^2 l_0\sigma_{hnf}Re\beta_0}{u_0\rho_f(m^2+1)}(\delta\epsilon u+mw)\Bigg], \tag{1.33}$$

The pressure gradient along the radial direction $(\partial p/\partial r)$ is deemed insignificant owing to the relatively small radius of the artery lumen when compared to the pressure wavelength so $(\partial p/\partial r)=0$. Alternatively,

$$\frac{\partial u}{\partial t}=-\left(\delta\epsilon\frac{u}{R(z)}\frac{\partial u}{\partial x}+\epsilon w\frac{\partial u}{\partial z}-\frac{\epsilon x}{R(z)}w\frac{\partial u}{\partial x}\frac{\partial R}{\partial z}\right)+\nu_{hnf}\left(1+\frac{1}{\beta}\right)\left[\frac{1}{R(z)^2}\frac{\partial^2 u}{\partial x^2}+\right.$$
$$\frac{1}{xR(z)^2}\frac{\partial u}{\partial x}+\epsilon^2\left(\frac{\partial^2 u}{\partial z^2}-\frac{2x}{R(z)}\frac{dR}{dz}\frac{\partial^2 u}{\partial x\partial z}-\frac{x}{R(z)}\frac{d^2R}{dz^2}\frac{\partial u}{\partial x}+\frac{2x}{R(z)}\left(\frac{dR}{dz}\right)^2\frac{\partial u}{\partial x}-\right.$$
$$\left.\left.\frac{x^2}{R(z)^2}\left(\frac{dR}{dz}\right)^2\frac{\partial^2 u}{\partial x^2}\right)-\frac{u}{xR(z)}\right]+\frac{\mu_f l_0\sigma_{hnf}M^2}{R_0^2\sigma_f\rho_{hnf}(m^2+1)}(\delta\epsilon u+mw), \tag{1.34}$$

and along the axial direction, momentum profile (1.30):

$$\frac{\partial w}{\partial t}+\frac{\delta\epsilon u}{R(z)}\frac{\partial w}{\partial x}+\epsilon w\left(\frac{\partial w}{\partial z}-\frac{x}{R(z)}\frac{dR}{dz}\frac{\partial w}{\partial x}\right)=\frac{\rho_f}{Re\rho_{hnf}}\Bigg[-\frac{\partial p}{\partial z}+\frac{\mu_{hnf}}{\mu_f}\left(1+\frac{1}{\beta}\right)\times$$
$$\left\{\frac{1}{R(z)^2}\frac{\partial^2 w}{\partial x^2}+\frac{1}{xR(z)^2}\frac{\partial w}{\partial x}+\epsilon^2\left(\frac{\partial^2 w}{\partial z^2}-\frac{2x}{R(z)}\frac{dR}{dz}\frac{\partial^2 w}{\partial x\partial z}-\frac{x}{R(z)}\frac{d^2R}{dz^2}\frac{\partial w}{\partial x}+\right.\right.$$
$$\left.\left.\frac{2x}{R(z)^2}\left(\frac{dR}{dz}\right)^2\frac{\partial w}{\partial x}-\left(\frac{x}{R(z)}\right)^2\left(\frac{dR}{dz}\right)^2\frac{\partial^2 w}{\partial x^2}\right)\right\}+\frac{\sigma_{hnf}M^2}{\sigma_f(m^2+1)}(w-\delta\epsilon mu), \tag{1.35}$$

adding the expression for flow directional pressure gradient in equation (1.18),

$$\frac{\partial w}{\partial t}=-\left(\frac{\delta\epsilon u}{R(z)}\frac{\partial w}{\partial x}+\epsilon w\frac{\partial w}{\partial z}-\frac{\epsilon x w}{R(z)}\frac{dR}{dz}\frac{\partial w}{\partial x}\right)+\frac{\rho_f}{Re\rho_{hnf}}\Big[A_0(1+e\cos(c_1 t))+$$
$$\frac{\mu_{hnf}}{\mu_f}\left(1+\frac{1}{\beta}\right)\left\{\frac{1}{R(z)^2}\frac{\partial^2 w}{\partial x^2}+\frac{1}{xR(z)^2}\frac{\partial w}{\partial x}+\epsilon^2\left(-\frac{2x}{R(z)}\frac{dR}{dz}\frac{\partial^2 w}{\partial x\partial z}-\frac{x}{R(z)}\frac{d^2R}{dz^2}\frac{\partial w}{\partial x}+\right.\right.$$
$$\left.\left.\frac{2x}{R(z)^2}\left(\frac{dR}{dz}\right)^2\frac{\partial w}{\partial x}-\left(\frac{x}{R(z)}\right)^2\left(\frac{dR}{dz}\right)^2\frac{\partial^2 w}{\partial x^2}\right)+\frac{\partial^2 w}{\partial z^2}\right\}+\frac{\sigma_{hnf}M^2}{\sigma_f(m^2+1)}(w-\delta\epsilon mu), \tag{1.36}$$

In a similar manner, an energy profile would look like this:

$$\frac{\partial\theta}{\partial t} = -\left(\frac{\delta\epsilon u}{R(z)}\frac{\partial\theta}{\partial x} + \epsilon w\frac{\partial\theta}{\partial z} - \frac{\epsilon x w}{R(z)}\frac{dR}{dz}\frac{\partial\theta}{\partial x}\right) + \frac{\kappa_{hnf}(\rho C_p)_f}{\kappa_f(\rho C_p)_{hnf}RePr}\left[\frac{1}{R(z)^2}\frac{\partial^2\theta}{\partial x^2} + \frac{1}{xR(z)^2}\frac{\partial\theta}{\partial x} + \epsilon^2\left(\frac{\partial^2\theta}{\partial z^2} - \frac{2x}{R(z)}\frac{dR}{dz}\frac{\partial^2\theta}{\partial r\partial x} - \frac{x}{R(z)}\frac{d^2R}{dz^2}\frac{\partial\theta}{\partial x} + \frac{2x}{R(z)^2}\left(\frac{dR}{dz}\right)^2\frac{\partial\theta}{\partial x} - \left(\frac{x}{R(z)}\frac{dR}{dz}\right)^2\frac{\partial^2\theta}{\partial x^2}\right)\right] + \frac{2Ec(\rho C_p)_f}{Re(\rho C_p)_{hnf}}\left(1+\frac{1}{\beta}\right)\left[\frac{\delta^2\epsilon^2}{R(z)^2}\left(\frac{\partial u}{\partial x}\right)^2 + \left(\frac{\delta\epsilon u}{xR(z)}\right)^2 + \epsilon^2\left(\left(\frac{\partial w}{\partial z}\right)^2 + \left(\frac{x}{R(z)}\frac{dR}{dz}\frac{\partial w}{\partial x}\right)^2 - \frac{2x}{R(z)}\frac{dR}{dz}\frac{\partial w}{\partial x}\frac{\partial w}{\partial z}\right) + \frac{\delta^2\epsilon^2}{2}\left(\left(\frac{\partial u}{\partial z}\right)^2 + \left(\frac{x}{R(z)}\frac{dR}{dz}\frac{\partial u}{\partial x}\right)^2 - \frac{2x}{R(z)}\frac{dR}{dz}\frac{\partial u}{\partial x}\frac{\partial u}{\partial z}\right) + \frac{1}{2R(z)^2}\left(\frac{\partial w}{\partial x}\right)^2 + \frac{\sigma^2\epsilon^2u_0}{l_0^2}\left(\frac{1}{R(z)}\frac{\partial u}{\partial z}\frac{\partial w}{\partial x} - \frac{x}{R(z)}\frac{dR}{dz}\frac{\partial u}{\partial x}\frac{\partial w}{\partial x}\right)\right] \tag{1.37}$$

1.8 Hemodynamic factors

Hemodynamic factors are important for regulating blood flow in the cardiovascular system and can affect various physiological and pathological processes. The two important parameters that are often studied in relation to blood flow dynamics are the local Nusselt number and wall shear stress.

1.8.1 Local Nusselt number

The local Nusselt number (Nu) is a dimensionless quantity used to measure convective heat transfer at a specific point within a fluid flow. When examining blood flow, the local Nusselt number provides valuable information about the effectiveness of heat transfer processes near the vessel walls. It calculates the ratio of convective heat transfer to conductive heat transfer and reflects how well the blood exchanges heat with the vessel walls, mathematically expressed as:

$$Nu_l = -\left(\frac{\partial\theta}{\partial r}\right)_{r=R(z)} \tag{1.38}$$

Using the radial coordinate transformation from section 1.7.1

$$Nu_l = -\frac{1}{R(z)}\left(\frac{\partial\theta}{\partial x}\right)_{x=1} \tag{1.39}$$

1.8.2 Wall shear stress

Wall shear stress refers to the tangential force per unit area exerted by the flowing blood on the endothelial lining of blood vessels. It arises due to the viscous friction between the blood and the vessel walls and is a critical determinant of endothelial function and vascular health. Wall shear stress influences various physiological

processes, including endothelial cell function, vascular remodeling, and the development of atherosclerosis. Shear stress in walls appears as:

$$\tau_w = -\mu_{hnf}\left(\frac{\partial w}{\partial r}\right)_{r=R(z)} \tag{1.40}$$

Using the radial coordinate transformation from section 1.7.1

$$\tau_w = -\frac{\mu_{hnf}}{R(z)}\left(\frac{\partial w}{\partial x}\right)_{x=1} \tag{1.41}$$

1.9 Numerical scheme

Numerical methods refer to a collection of mathematical problem-solving techniques that rely on numerical approximations and computations. Such methods are particularly applicable in situations where analytical or exact solutions are either impractical or impossible to obtain. The techniques are often used in a variety of fields, including engineering, physics, and finance, to name a few. Overall, numerical methods provide a reliable and efficient means of tackling complex mathematical problems that would otherwise be challenging to solve. The choice of a numerical method depends on the specific mathematical problem, available resources, and desired accuracy.

1.9.1 Finite difference method:

The finite differentiation method (FDM) is a numerical technique that approximates derivatives of functions. Dealing with analytical derivatives or discrete data, where the numerical solution is known only at a finite number of points in the physical domain, can be challenging to compute. The number of points which impact the accuracy and regulation of the numerical solution can be selected manually. The "mesh" refers to the collection of locations where the discrete solution is calculated. These locations are known as "nodes". For two dimensional in space and time, the key parameters of the mesh are Δx, Δz, and Δt. Δx and Δz represent the distance between adjacent points in 2D space, determining the resolution of the simulation. Meanwhile, Δt represents the distance between adjacent time steps, which determines the precision of the simulation over time. Figure 1.5 illustrates the solution domain. If x, z and t are an interval of uniform spacing $0 \leq x \leq xmax$, $0 \leq z \leq zmax$ and $0 \leq t \leq tmax$

$$x_j = \Delta x(j-1), \quad j = 1,2,3,...J,$$

$$z_m = \Delta z(m-1), \quad m = 1,2,3,...M,$$

and

$$t_n = \Delta t(n-1), \quad n = 1,2,3,...N,$$

where J, M and N are the total number of space and time steps or *nodes* including boundary. Size of time step Δt and space steps Δx, Δz can be expressed as follows:

$$\Delta x = \frac{xmax}{J-1}, \quad \Delta z = \frac{zmax}{M-1} \quad \Delta t = \frac{tmax}{N-1},$$

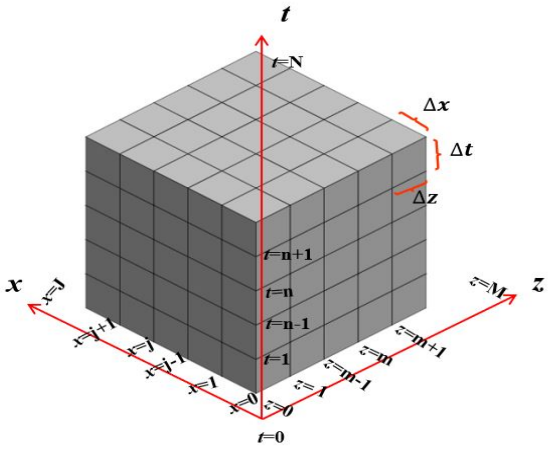

FIGURE 1.5: 2D mesh on bounded geometry with small squares for approximation.

Finite difference approximations discretize a continuous domain to estimate derivatives in order to solve differential equations numerically. For function f, using discrete approximations

$$\frac{\partial f}{\partial x}(x_i) \approx \frac{f(x_{i+1}) - f(x_i)}{\Delta x}$$

Using Taylor series expansion f at any point x_i

$$f(x_i + \delta x) = f(x_i) + \delta x \frac{\partial f}{\partial x}\Big|_{x_i} + \frac{(\delta x)^2}{2!}\frac{\partial^2 f}{\partial x^2}\Big|_{x_i} + \frac{(\delta x)^3}{3!}\frac{\partial^3 f}{\partial x^3}\Big|_{x_i} + \ldots\ldots,$$

replacing δx with Δx and solving above expression for $(\partial f/\partial x)_{x_i}$,

$$\frac{\partial f}{\partial x}\Big|_{x_i} = \frac{f(x_i + \Delta x) - f(x_i)}{\Delta x} - \frac{(\Delta x)^2}{2}\frac{\partial^2 f}{\partial x^2}\Big|_{x_i} - \frac{(\Delta x)^3}{3!}\frac{\partial^3 f}{\partial x^3}\Big|_{x_i} + \ldots\ldots,$$

and then

$$\frac{\partial f}{\partial x}\Big|_{x_i} = \frac{f(x_{i+1}) - f(x_i)}{\Delta x} + O(\Delta x) \tag{1.42}$$

Equation (1.42) is called **first order forward difference formula** with a truncation error of $O(\Delta x)$, which can be controlled by choosing the right mesh size. Similarly, the

$$\frac{\partial f}{\partial x}\Big|_{x_i} \approx \frac{f(x_i) - f(x_{i+1})}{\Delta x} + O(\Delta x), \tag{1.43}$$

is the first order backward difference formula,

$$\frac{\partial f}{\partial x}\Big|_{x_i} \approx \frac{f(x_{i-1}) - f(x_{i-1})}{2\Delta x} + O(\Delta x), \tag{1.44}$$

is the first order central difference formula, and

$$\frac{\partial^2 f}{\partial x^2}\Big|_{x_i} \approx \frac{f(x_{i+2}) - 2f(x_{i+1}) + f(x_i)}{\Delta x^2} + O(\Delta x)^2, \tag{1.45}$$

is the second order forward difference formula, and

$$\frac{\partial^2 f}{\partial x^2}\Big|_{x_i} \approx \frac{f(x_i) - 2f(x_{i-1}) + f(x_{i=2})}{\Delta x^2} + O(\Delta x)^2, \tag{1.46}$$

is the second order forward difference formula, and

$$\frac{\partial^2 f}{\partial x^2}\Big|_{x_i} \approx \frac{f(x_{i+1}) - 2f(x_i) + f(x_{i-1})}{\Delta x^2} + O(\Delta x)^2, \tag{1.47}$$

is the second order central difference formula.
The non-dimensional coupled and nonlinear set of differential equations along with associated initial and boundary conditions in equations (1.24)-(1.26) are computed numerically using expressions (1.42)-(1.47) for **explicit forward time central space finite differential scheme (FTCS)**, resulting in:

$$\begin{aligned}
\frac{\partial w}{\partial t} &= \frac{w_j^{n+1} - w_j^n}{\Delta t}, \\
\frac{\partial w}{\partial x} &= \frac{w_{j+1}^n - w_{j-1}^n}{2\Delta x}, \\
\frac{\partial^2 w}{\partial x^2} &= \frac{w_{j+1}^n - w_j^n + w_{j-1}^n}{(\Delta x)^2}, \\
\frac{\partial \theta}{\partial t} &= \frac{\theta_j^{n+1} - \theta_j^n}{\Delta t}, \\
\frac{\partial \theta}{\partial x} &= \frac{\theta_{j+1}^n - \theta_{j-1}^n}{2\Delta x}, \\
\frac{\partial^2 \theta}{\partial x^2} &= \frac{\theta_{j+1}^n - \theta_j^n + \theta_{j-1}^n}{(\Delta x)^2}.
\end{aligned} \tag{1.48}$$

In the context of blood flow through a constricted artery, where the flow is assumed to be predominantly in the axial direction (z), a 1D treatment in the radial direction (x) is sufficient to capture the primary flow features, particularly when the flow is assumed to be axisymmetric. Moreover, the variations in the axial direction are much slower compared to the radial direction, so one-dimensional FTCS provides a reasonable approximation of the flow behavior.

Using expressions in equation (1.48), flow equations will take the following form:

$$w(j,n+1) = w(j,n) + \Delta t \frac{\rho_f}{\rho_{hnf} Re}\left[A_0(1+e\cos(c_1 t(n)) + \frac{\mu_{hnf}}{\mu_f}\frac{1}{(R(m))^2}\left(1+\frac{1}{\beta}\right)\right.$$
$$\left(\frac{w(j+1,n)-w(j,n)+w(j-1,n)}{\Delta x^2} + \frac{1}{x(j)}\frac{w(j+1,n)-w(j-1,n)}{2\Delta x}\right)+$$
$$\left.\frac{M^2}{m^2+1}\frac{\sigma_{hnf}}{\sigma_f}w(j,n)\right] \quad (1.49)$$

$$\theta(j,n+1) = \theta(j,n) + \Delta t \frac{(\rho C_p)_f}{(\rho C_p)_{hnf}}\left[\frac{\kappa_{hnf}}{\kappa_f}\frac{1}{RePr}\frac{1}{(R(m))^2}\left(\frac{\theta(j+1,n)-\theta(j,n)+\theta(j-1,n)}{\Delta x^2}\right)\right.$$
$$+\frac{1}{x(j)}\frac{\theta(j+1,n)-\theta(j-1,n)}{2\Delta x} + \left(1+\frac{1}{\beta}\right)\frac{\mu_{hnf}}{\mu_f}\frac{Ec}{Re(R(m))^2}\left(\frac{w(j+1,n)-w(j-1,n)}{2\Delta x}\right)^2+$$
$$\left.\frac{\sigma_{hnf}}{\sigma_f}\frac{EcM^2}{Re}(w(j,n))^2\right], \quad (1.50)$$

with initial and boundary conditions:

$$w(j,1) = 0, \quad \theta(j,1) = 0, \qquad at \quad t = 0,$$

$$w(j+1,n) = w(j,n), \quad \theta(j+1,n) = \theta(j,n), \qquad at \ x = 0,$$
$$w(J,n) = 0, \quad \theta(J,n) = 1, \qquad at \ x = 1. \quad (1.51)$$

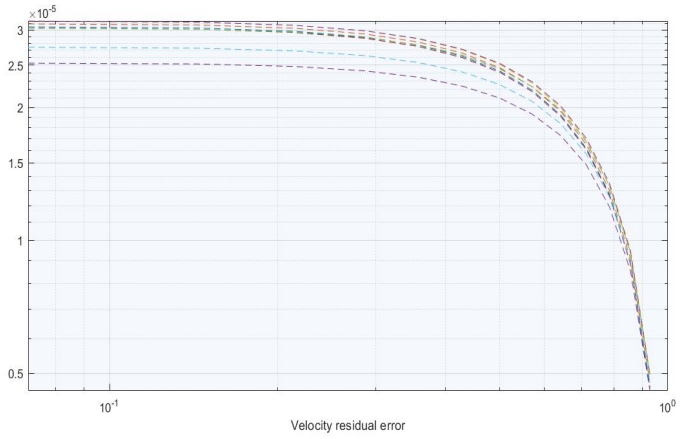

FIGURE 1.6: Convergence of velocity profile: Residual error analysis.

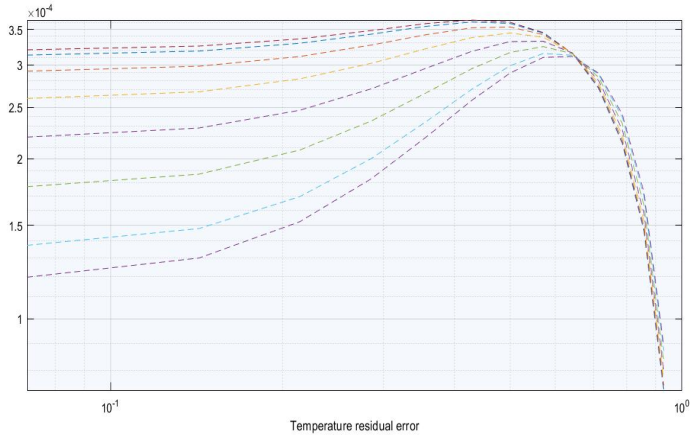

FIGURE 1.7: Convergence of temperature profile: Residual error analysis.

The **stability of FTCS scheme** depends on the step size Δx and Δt and for the current simulation $\Delta x = 0.025$ and $\Delta t = 0.0001$ are taken which are suitable for satisfying the stability condition (von Neumann stability analysis). Figure 1.6 and Figure 1.7, indicate the residual error graphs for both velocity and temperature profiles maintaining 10^{-6} error across the entire domain. The initial residual errors are relatively high in Figure 1.6 and 1.7, as significant corrections are made to the velocity and temperature field in the first few iterations or time steps. The residual error lines demonstrate a consistent and steady decay, indicating numerical method stability. As the iterations or time steps progress, the rate of decline in residual error slows down, and the curves start to flatten out, indicating the convergence of the solution. This indicates that the solution is approaching a steady state where further iterations or time steps do not result in significant changes in the velocity and temperature field.
The values of emerging parameters occurring in the set of non-dimensional PDEs are provided in Table 1.4.

TABLE 1.4: Values of non-dimensional parameters in equations (1.24)-(1.26).

Parameters	Fixed values
Reynolds number (Re)	02.00
Hartmann number (M)	00.50
Casson fluid parameter (β)	00.50
Eckert number (Ec)	04.00
Volume fraction of Copper nanoparticles (ϕ_1)	00.01
Volume fraction of Aluminium oxide nanoparticles (ϕ_2)	00.01
Mean pressure gradient (A_0)	01.41
Prandtl number (Pr)	07.00
Eccentricity (e)	00.50
Angular frequency (c_1)	01.00
Hall current parameter (m)	01.50

1.10 Flow analysis

An analysis is conducted of velocity and temperature profiles of non-Newtonian blood flow in the presence of Copper (Cu) and Aluminium Oxide (Al_2O_3) hybrid nanoparticles within a stenotic artery, using graphical and tabular representations. The flow is subjected to an applied magnetic field and a pulsating pressure gradient, a common cardiovascular physiological condition. The applied magnetic field is a deliberate external force introduced into the system in a controlled experimental or therapeutic setting to explore the potential benefits and impacts of magnetohydrodynamics (MHD) in medical applications. The non-Newtonian behavior of the blood is modeled using the Casson fluid model, which accounts for the yield stress exhibited by blood—a critical factor when considering the realistic flow of blood through constricted or diseased arteries and is particularly important in the study of blood flow in arteries with stenosis, where shear rates can vary significantly due to the narrowing of the artery.
This section consists of the influence of quantitative parameters emerging in the flow equations such as the volume fraction of Cu and Al_2O_3 nanoparticles, Casson fluid parameter, stenosis height, Reynolds number, Eckert number and Hartmann number over momentum and temperature equation (Table 1.5). For the computational part, $A_0 = 1.41$, $Re = 2.0$, $e = 0.5$, $c_1 = 1.0$, $\beta = 0.5$, $R = 0.825$, $M = 0.5$, $m = 0.1$, $Pr = 14$, $Ec = 0.1$, $\phi_1 = 0.025$ and $\phi_2 = 0.025$ are taken into account.

TABLE 1.5: Variations in emerging parameters.

Parameters	variations
Reynolds number (Re)	2, 2.5 , 3, 3.5
Hartmann number (M)	0.5, 1.0, 1.5, 2.0
Casson fluid parameter (β)	0.5, 1.0, 1.5, 2.0
Eckert number (Ec)	0.5, 1.0, 1.5, 2.0
Concentration of nanoparticle (ϕ_1, ϕ_2)	0.01, 0.02, 0.03, 0.04

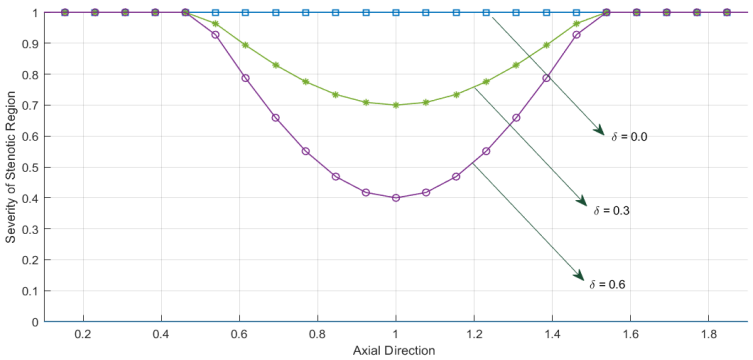

FIGURE 1.8: Variation of stenosis severity along the axial direction of an artery.

Figure 1.8 illustrates the impact of stenosis on the arterial radius, with the severity of stenosis altering the radius along the axial direction. The blue line (δ=0.0) reflects a non-stenotic, healthy artery. At δ=0.3, the stenosis causes a significant reduction in the arterial radius, leading to a decrease in the cross-sectional area by 51%,

which can substantially increase resistance to blood flow and may require clinical intervention. At δ=0.6, the stenosis is even more pronounced, with an 84% reduction in the cross-sectional area, which represents a severe narrowing that could critically restrict blood flow and would likely necessitate immediate medical treatment.

1.10.1 Plots for velocity profile

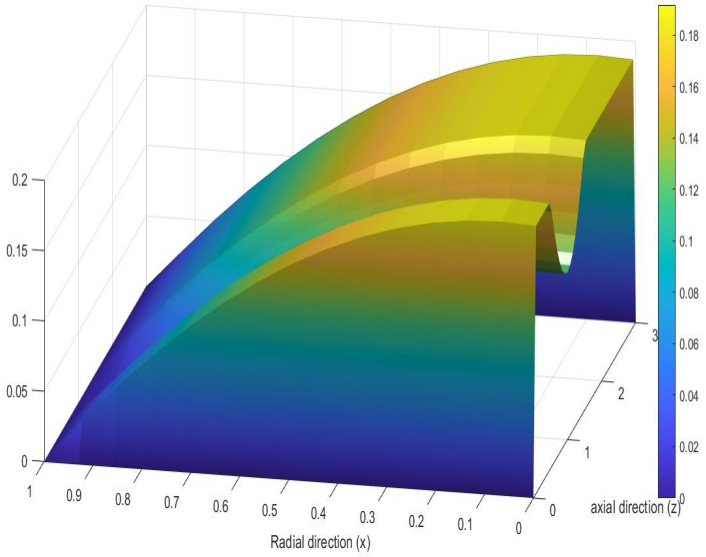

FIGURE 1.9: Surface plot for the velocity distribution of hybrid nanofluid in a 36% axisymmetric constricted stenotic artery.

Figure 1.9 shows the velocity profile of axisymmetric blood flow in an elliptical stenotic artery. The 3D surface plot visualizes the radial and axial directions as x and z, respectively. The color range indicates the velocity spectrum, with blue representing low velocities and yellow representing high velocities. The stenosis is represented as a dip in the center of the plot, indicating the arterial narrowing. The dark blue area of the artery axis indicates zero velocity gradient, which characterizes axisymmetric flow. At the central axis of the artery in Figure 1.9, flow velocity remains constant, with a uniform flow that lacks radial variance. The yellow-colored area at the artery walls represents the no-slip condition. This means that blood sticks to the walls, resulting in zero velocity at the interface due to viscosity. Stenosis creates an area of resistance to blood flow, causing acceleration and higher speeds at the edges of the constriction and this acceleration is followed by a deceleration downstream of the stenosis.

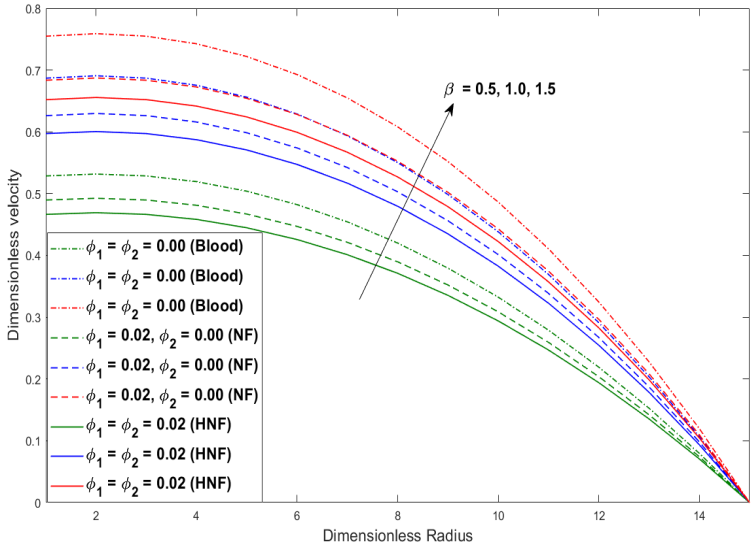

FIGURE 1.10: Blood, Cu-blood and Cu-Al_2O_3-blood velocity profiles against variation in Casson Model Parameter (β).

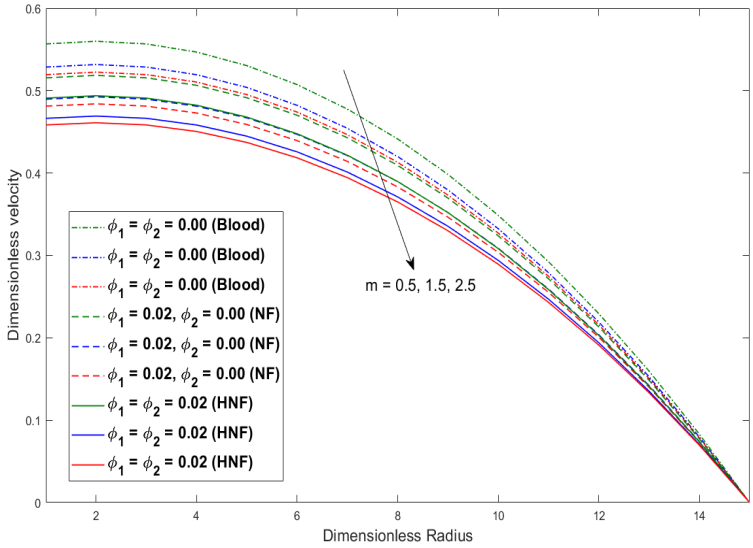

FIGURE 1.11: Blood, Cu-blood and Cu-Al_2O_3-blood velocity profiles against variation in Hall current Parameter (m).

A noticeable trend from the graph 1.10 is the escalation in velocity with the rise in the Casson model parameter, β. This trend holds across the three different mediums: the base fluid (blood without nanoparticles, $\phi_1 = \phi_2 = 0.00$), the nanofluid (blood with Cu nanoparticles, $\phi_1 = 0.02, \phi_2 = 0.00$) and the hybrid nanofluid (blood with both Cu and Al_2O_3 nanoparticles, $\phi_1 = \phi_2 = 0.02$). The incremental increase in velocity with respect to β across all mediums suggests a decrease in the effective viscosity of the blood, which allows for a more streamlined flow through the constricted region. Interestingly, the graph also reveals that the mass transfer is higher for the base fluid when compared to the hybrid nanofluid as β increases. This observation

may seem counterintuitive as nanoparticles are often thought to enhance mass transfer due to their influence on the effective viscosity and thermal conductivity of the blood. However, the higher mass transfer in the base fluid could be attributed to the complex interactions between the blood components and the hybrid nanoparticles. Non-Newtonian velocity profiles are illustrated in Figure 1.11 for ordinary fluid, nanofluid, and hybrid nanofluid against the variation in the strength of Hall current parameter m. With increasing values of m, a decrease in the dimensionless velocity is observed for the base fluid representing blood, Cu-blood, and Cu-Al_2O_3-Blood. This indicates that the Hall current acts to slow down the flow due to the interaction between the induced electric field and the charge carriers in the blood, which creates a force opposing the flow. Furthermore, the graph indicates that mass transfer is higher in the base fluid compared to the hybrid nanofluid as the Hall current parameter increases. The Hall effect cause a redistribution of charge carriers that hampers the usual mass transfer enhancements expected from nanoparticle additives.

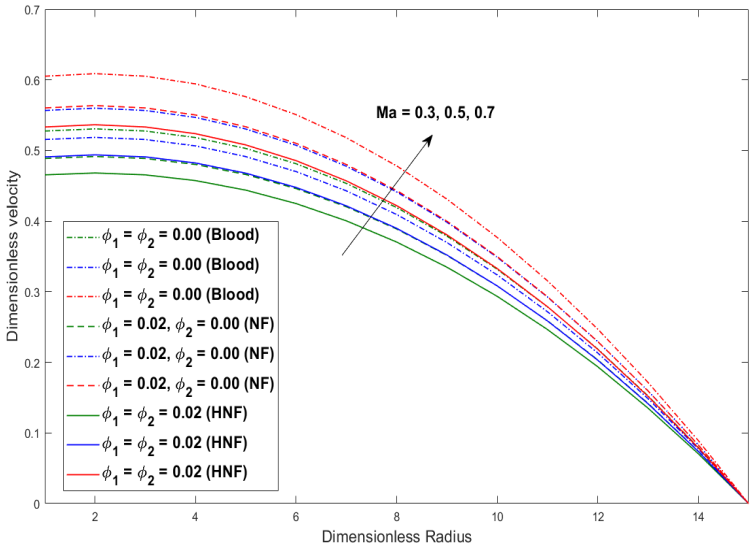

FIGURE 1.12: Blood, Cu-blood and Cu-Al_2O_3-blood velocity profiles against variation in dimensionless Hartmann number (Ma).

Velocity profiles of non-Newtonian blood flow through a stenotic artery against magnetic parameter (Ma) are traced in Figure 1.12. The Magnetic parameter, also known as the Hartmann number is a dimensionless quantity in magnetohydrodynamics that characterizes the influence of a magnetic field on the flow of an electrically conducting fluid. As shown, there is an observed increase in velocity with an increase in the Hartmann number across all fluids examined (ordinary fluid, nanofluids, and hybrid nanofluids). This phenomenon is well-documented and caused by magnetic damping at higher Ma values. The magnetic field imposes a force on the moving charged particles within the fluid, which aligns the flow and reduces the velocity gradients, leading to a more streamlined flow profile. Hybrid nanofluid provides a higher mass transfer rate than the base fluid due to improved thermal and electrical conductivities brought by nanoparticles. The graph shows evidence of magnetohydrodynamic (MHD) flow control in biomedical applications. The Hartmann number plays a significant role in regulating flow behavior. It offers a potential mechanism for targeted drug delivery systems. A magnetic field can

enhance the transportation of medication to specific sites in the body.

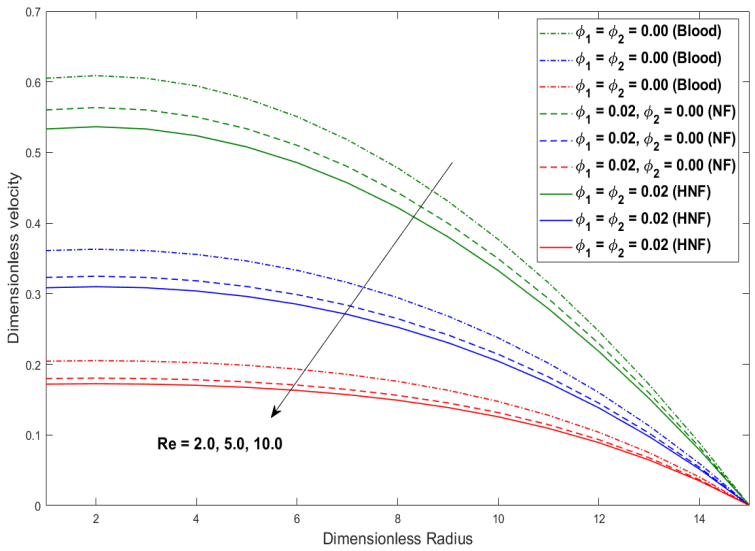

FIGURE 1.13: Blood, Cu-blood and Cu-Al_2O_3-blood velocity profiles against variation in dimensionless Reynolds number (Re).

Figure 1.13 provides an analysis of the laminar velocity profiles and mass transfer characteristics. It can be noticed that for increasing values of Reynolds number $(Re = 2.0, 5.0, 10.0)$, the momentum profile declines for all fluids. Reynolds number is the ratio of inertial to viscous forces. An increase in Reynolds number causes a reduction in viscous forces, which, in turn, decreases the velocity profiles. The graph also illustrates that mass transfer is higher for the ordinary fluid (blood, $\phi_1 = \phi_2 = 0.0$) compared to the hybrid nanofluids (Cu-Al_2O_3-blood, $\phi_1 = \phi_2 = 0.02$), as indicated by the higher velocity profiles of the dotted lines representing the base fluid.

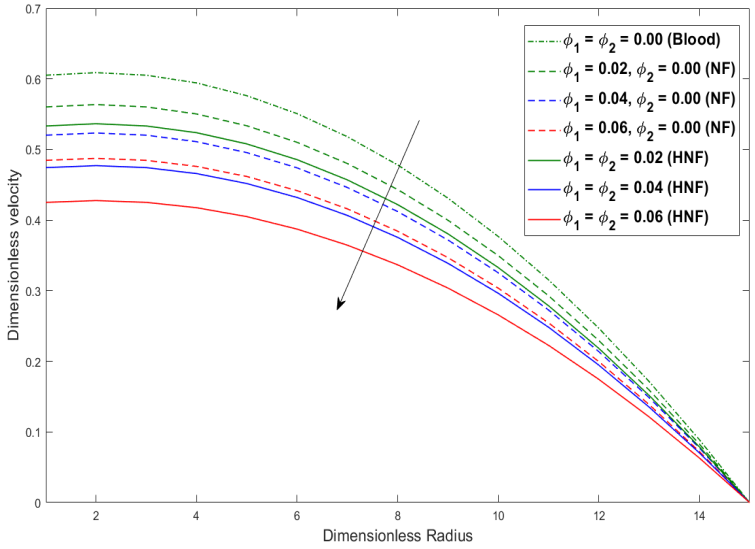

FIGURE 1.14: Blood, Cu-blood and Cu-Al_2O_3-blood velocity profiles against variation in volume fraction ϕ_1, ϕ_2 for Cu and Al_2O_3.

Investigation for the effect of incorporating the copper Cu nanoparticles and hybridized nanoparticles $Cu - Al_2O_3$ into the base liquid (blood) is demonstrated in Figure 1.14. The velocity is indicated to be maximal for the base fluid, which, in this context, is blood without any nanoparticles, as shown by the small green dotted line. As Cu nanoparticles are added to the blood, with an increasing nanoparticle volume fraction $(\phi_1 = 0.02, 0.04, 0.06, \phi_2 = 0.00)$, a reduction in the velocity profile is observed. Scientific literature has thoroughly explored the impact of introducing nanoparticles to blood, which has been found to increase its viscosity. Nanoparticles interact with blood plasma and cells, resulting in heightened resistance to flow, particularly at high concentrations. This effect leads to an increase in blood viscosity and can cause a reduction in its mobility and thickness. Further, the addition of hybrid nanoparticles (Cu-Al2O3) into the blood and the subsequent increase in their volume fraction $(\phi_1 = \phi_2 = 0.02, 0.04, 0.06)$ results in an even greater decline in the velocity profiles, plotted by three straight lines.

1.10.2 Plots for temperature profile

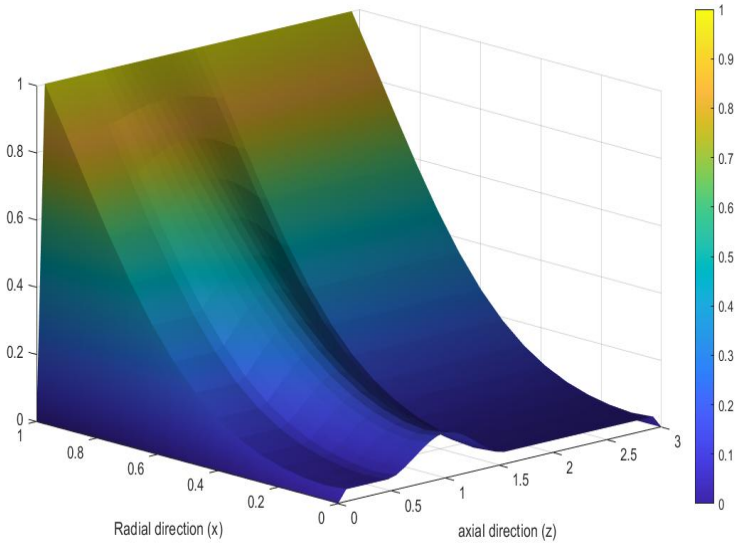

FIGURE 1.15: Surface plot for the temperature distribution of hybrid nanofluid in a 36% axisymmetric constricted stenotic artery.

A 3D surface plot illustrating the temperature distribution of blood as it flows through an axisymmetric elliptical-shaped stenotic artery is featured in Figure 1.15, which has implications for the function and health of the vascular system. The blue region along the axis indicates a zero temperature gradient, implying constant temperature across the radial dimension due to symmetry. This means no net heat transfer across the flow perpendicular to it, consistent with axisymmetric flow conditions. Yellow regions at the artery's periphery represent walls with constant temperature boundary conditions of 1. The progression from blue at the center to yellow at the walls suggests a radial temperature gradient, with heat transferring from the wall toward the center of the artery.

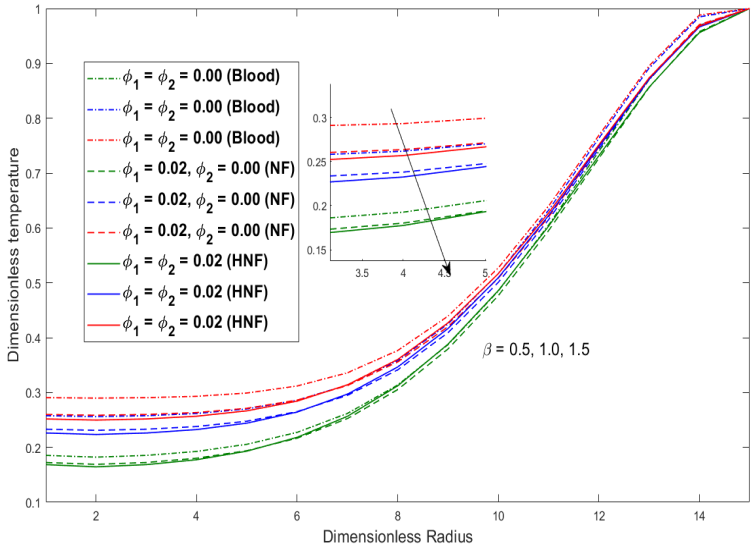

FIGURE 1.16: Blood, Cu-blood and Cu-Al_2O_3-blood temperature profiles against variation in Casson model parameter (β).

From Figure 1.16, it is evident that increasing the Casson model parameter $(\beta = 0.5, 1.0, 1.5)$ leads to a decrease in the dimensionless temperature across all fluids: ordinary fluid, nanofluids, and hybrid nanofluids. This indicates that when the blood exhibits more non-Newtonian properties and behaves like a Casson fluid, its capacity to retain heat increases. This is because reduced fluidity hinders convective heat transfer from the heated area. It can also be noticed that the base fluid (blood) has a higher heat transfer compared to the hybrid nanofluid as β increases.

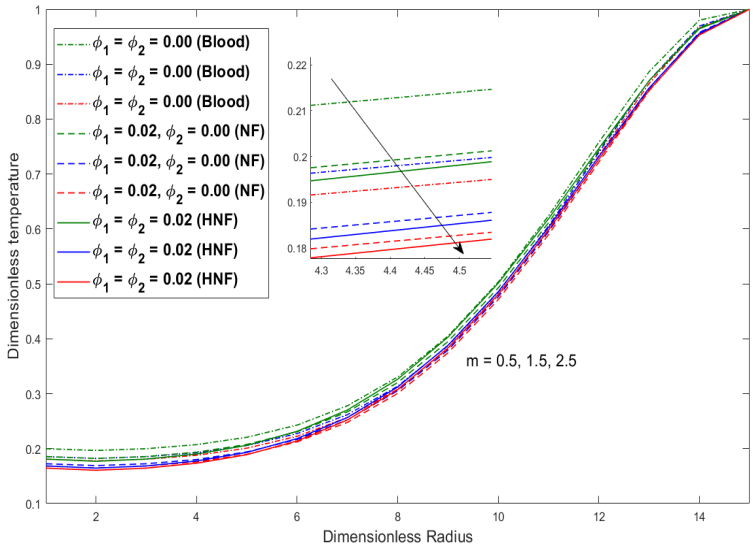

FIGURE 1.17: Blood, Cu-blood and Cu-Al_2O_3-blood temperature profiles against variation in Hall current parameter (m).

The influence of Hall current (m) on the temperature profile of non-Newtonian blood flow with and without the addition of nanoparticles (Cu, Al_2O_3) is evinced by

Figure 1.17. An increase in the Hall current parameter generated by the electromotive force (EMF) transverse to current in conducting fluid corresponds to a decrease in the dimensionless temperature for the base fluid/blood, the nanofluid/(Cu-blood), and the hybrid nanofluid/(Cu-Al_2O_3-blood). This suggests that the Hall effect induces changes within the fluid flow that enhance the convective heat transfer, leading to a cooler fluid temperature profile.

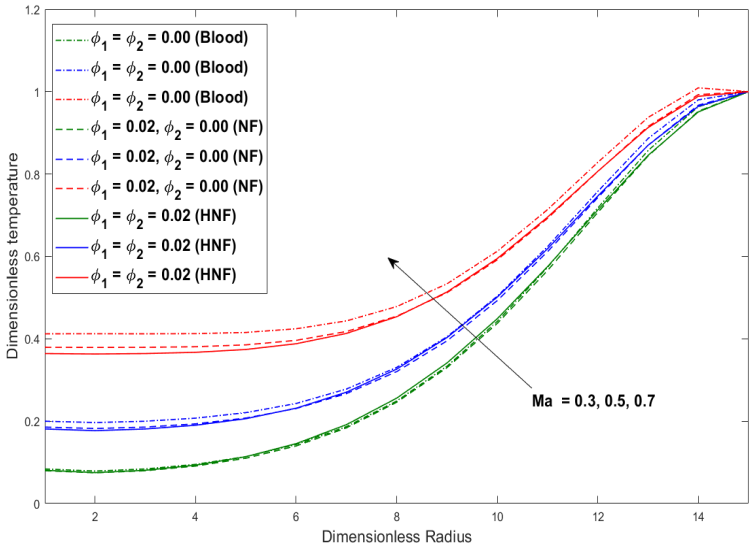

FIGURE 1.18: Blood, Cu-blood and Cu-Al_2O_3-blood temperature profiles against variation in dimensionless Hartmann number (Ma).

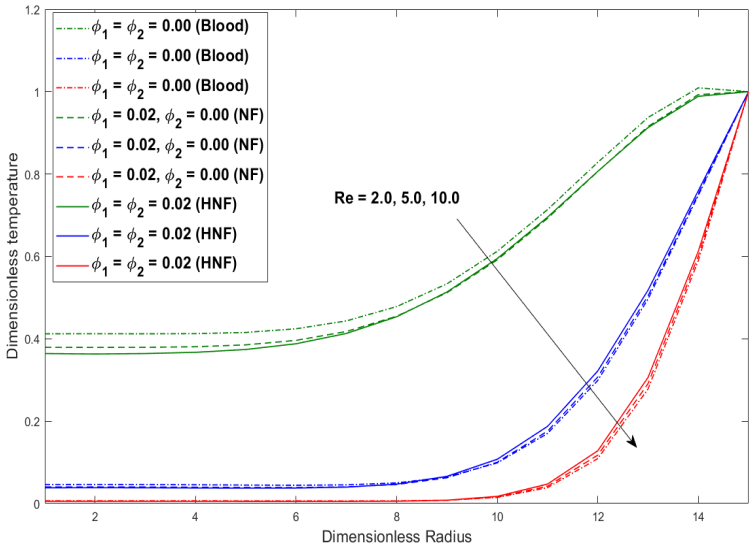

FIGURE 1.19: Blood, Cu-blood and Cu-Al_2O_3-blood temperature profiles against variation in dimensionless Reynolds number (Re).

The magnetic parameter, also known as the Hartmann number (Ma), is employed to understand the effects of a magnetic field on the temperature profiles in

Figure 1.18. From the graph, we observe an increase in temperature with an increasing Hartmann number for all fluid types. A magnetic field applied to a conducting fluid induces a perpendicular Lorentz force that can decrease turbulence and lead to laminar flow. Laminar flow has less mixing and surface contact, resulting in reduced heat dissipation from the fluid and a higher temperature. Reduction in temperature profiles against non-dimensional Reynolds number (Re) is represented in Figure 1.19. The data indicates a decrease in temperature with an increase in the non-dimensional Reynolds number for blood, Cu-blood and Cu-Al_2O_3-blood. This trend suggests that, for higher Reynolds number $(Re = 2.0, 5.0, 10.0)$, the convective heat transfer is enhanced, leading to more efficient heat dissipation from the fluid and, thus, a lower temperature. Additionally, the graph illustrates that heat transfer is more effective for the hybrid nanofluid Cu-Al_2O_3-blood as compared to the ordinary fluid as Re increases. Consequently, higher values of Re promote thinner thermal boundary layers and better mixing of fluid layers and allow for quicker heat dissipation from warmer to cooler regions, potentially reducing the overall temperature profile.

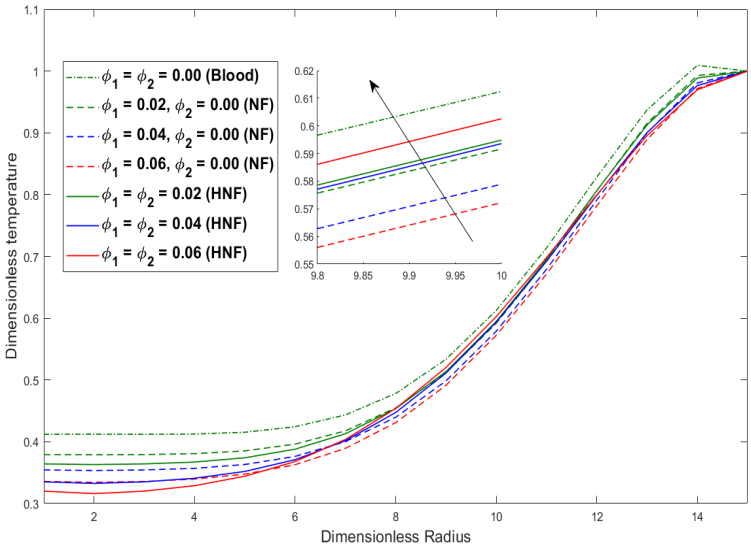

FIGURE 1.20: Blood, Cu-blood and Cu-Al_2O_3-blood temperature profiles against variation in volume fraction ϕ_1, ϕ_2 of Cu and Al_2O_3.

Figure 1.20 demonstrates the temperature profiles for the varying concentrations of Cu and Al_2O_3 nanoparticles. The temperature profile of the blood is shown to increase with the volume fraction of nanoparticles, indicating that the addition of nanoparticles affects the thermal properties of the blood. For the nanofluid with Cu nanoparticles and the hybrid nanofluid with Cu and Al_2O_3 nanoparticles, there is a clear trend of increasing temperature with higher volume fractions $(\phi_1, \phi_2 = 0.00, 0.02, 0.04, 0.06)$. This behavior can be explained by the enhanced thermal conductivity that nanoparticles impart to the base fluid. Nanoparticles generally have a higher thermal conductivity than the fluids in which they are dispersed, and their presence can significantly improve the fluid's ability to conduct heat. The graph shows that heat transfer is more efficient in the hybrid nanofluid compared to the base fluid. This is likely due to the combined effect of Cu and Al_2O_3 nanoparticles' thermal conductivities, which enhance the overall thermal conductivity of the hybrid nanofluid more than the single type of nanoparticles in the nanofluid.

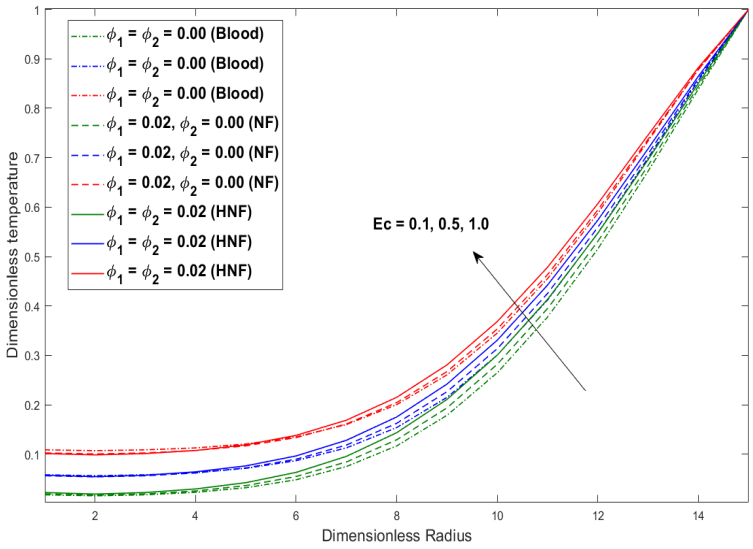

FIGURE 1.21: Blood, Cu-blood and Cu-Al_2O_3-blood temperature profiles against variation in dimensionless Eckert number (Ec).

In Figure 1.21, there is a noticeable increase in temperature profile for the fluid (base fluid, nanofluids, and hybrid nanofluids) for variation in dimensionless Eckert number (Ec), which describes the ratio of kinetic energy in the flow to enthalpy changes due to temperature differences, essentially relating the flow velocity to thermal effects. This trend is indicative of viscous dissipation – the conversion of the fluid's kinetic energy into heat – which is more pronounced at higher velocities or flow rates (higher Ec). The fluid's temperature increases as the blood's kinetic energy is dissipated as heat due to friction and viscous forces within the fluid.

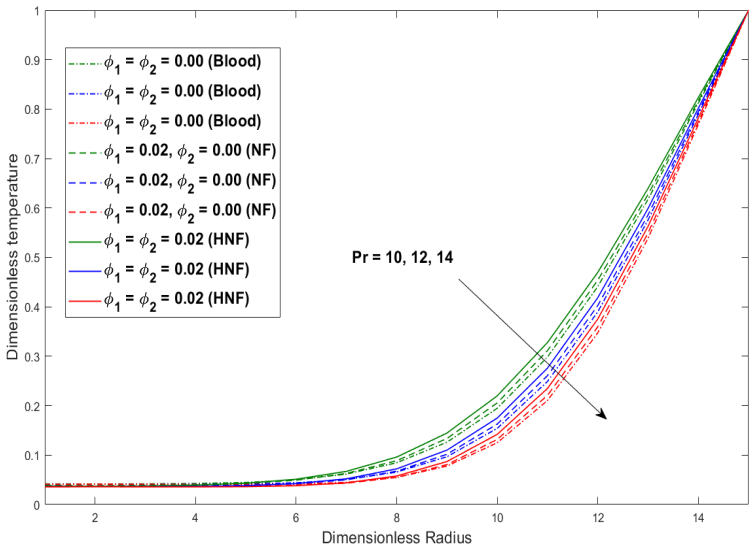

FIGURE 1.22: Blood, Cu-blood and Cu-Al_2O_3-blood temperature profiles against variation in dimensionless Prandtl number (Pr).

A diminution in temperature is indicated by the Figure 1.22 against variation in the values of dimensionless Prandtl number $(Pr = 10.0, 12.0, 14.0)$. An increase

in the *Pr* suggests that momentum diffusivity (viscosity) dominates over thermal diffusivity. Therefore, as Pr increases, the thermal boundary layer becomes thicker relative to the velocity boundary layer. In practical terms, this means heat is less efficiently diffused away from the heated surface (e.g., the arterial wall), potentially leading to lower temperatures in the fluid's bulk.

1.10.3 Plots for flow properties

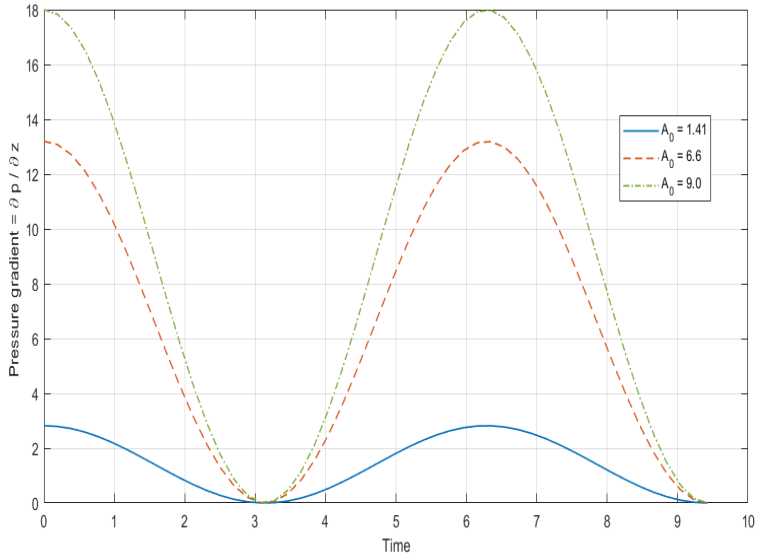

FIGURE 1.23: Pulsatile pressure gradient against variation in average crossectional area A_0.

Figure 1.23 shows the pressure gradient over time in an artery at different values of the mean cross-sectional area, represented by A_0. The blue line, representing $A_0 = 1.41$, shows smaller oscillations in the pressure gradient over time. This indicates that the artery has a smaller diameter and requires less pressure gradient to maintain blood flow. On the other hand, the red dashed line and the green dotted line, which correspond to larger A_0 values of 6.6 and 9.0, respectively, exhibit higher oscillations in the pressure gradient. This indicates that larger arteries with more substantial cross-sectional areas require higher pressure gradients to maintain blood flow. This is because a larger cross-sectional area allows for a greater blood flow volume, necessitating a higher pressure difference to overcome the viscous forces and inertia within the fluid. The peak values of the pressure gradient occur at similar times for each A_0 value, indicating that the pressure changes are synchronized with the heartbeats.

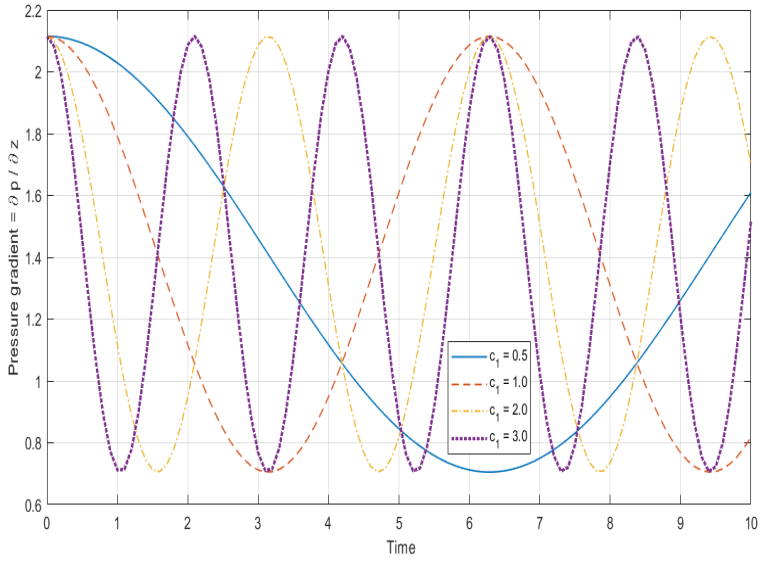

FIGURE 1.24: Pulsatile pressure gradient against variation in frequency parameter c_1.

The graph in Figure 1.24 depicts the variation of pressure gradient within an artery over time with changes in the frequency parameter c_1, which influences the pulsatile nature of the blood flow. Multiple curves correspond to different values of c_1 (0.5 to 3.0). c_1 is a frequency parameter that regulates how quickly the pressure gradient oscillates in response to heartbeats in the context of pulsatile blood flow in the cardiovascular system. With the rising value of the c_1 parameter, the rate at which the pressure gradient oscillates also increases, reflecting a more dynamic response to the pulsatile nature of blood flow.

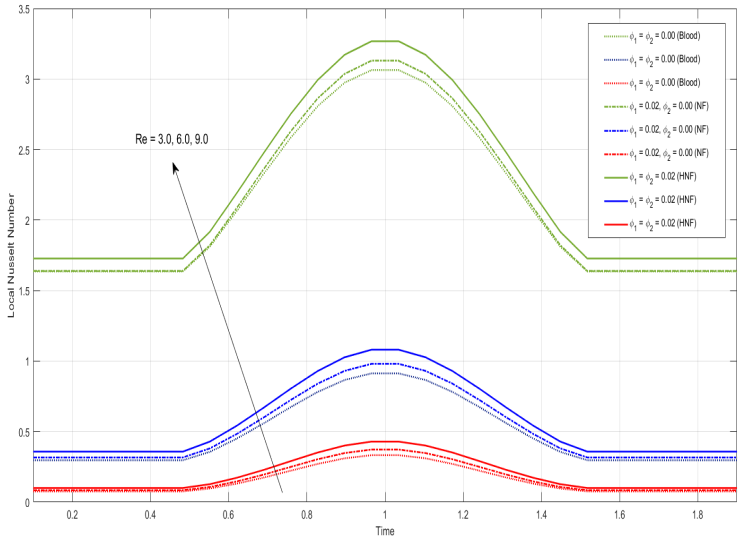

FIGURE 1.25: Local Nusselt number response to varying Reynolds number for blood, nanofluid, and hybrid nanofluid.

Figure 1.25 reveals the influence of the Reynolds number on the local Nusselt number (Nu_l), which represents the rate of heat transfer from the arterial wall to

the blood, normalized by the rate of conductive heat transfer. As Reynolds number increases, fluid's convection heat transfer improves due to increased mixing and disruption of the thermal boundary layer. Local Nusselt number, a dimensionless parameter, signifies this heat transfer efficiency, and its increase indicates better convective performance. In narrow arteries, increased blood flow velocity reduces the thickness of the fluid layer closest to the artery wall, which increases the temperature gradient at the wall. This gradient leads to higher heat transfer, reflected in a higher local Nusselt number.

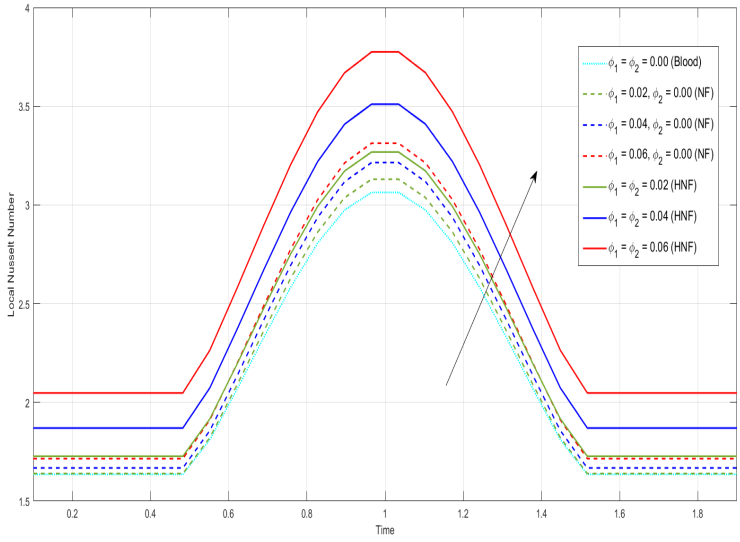

FIGURE 1.26: Local Nusselt number response to varying concentrations of Cu and Cu-Al_2O_3 nanoparticles.

The enhancement of the local Nusselt number with increasing volume fractions of Cu nanoparticles and Cu-Al_2O_3 hybrid nanoparticles in a blood flow through a stenotic artery is featured in Figure 1.26. The increased volume fraction of these nanoparticles means a greater number of particles are available to facilitate heat transfer through mechanisms such as Brownian motion and thermophoresis, leading to an enhanced local Nusselt number. Brownian motion increases the energy exchange between particles and the surrounding fluid, while thermophoresis drives particles from hotter to cooler regions, contributing to the heat transfer process. The graph indicates that the impact of hybrid nanoparticles on the local Nusselt number is more pronounced than that of single-component nanoparticles. This suggests that the synergistic effect of combining Cu and Al_2O_3 nanoparticles optimizes the heat transfer characteristics of the nanofluid more effectively than either type of nanoparticle alone.

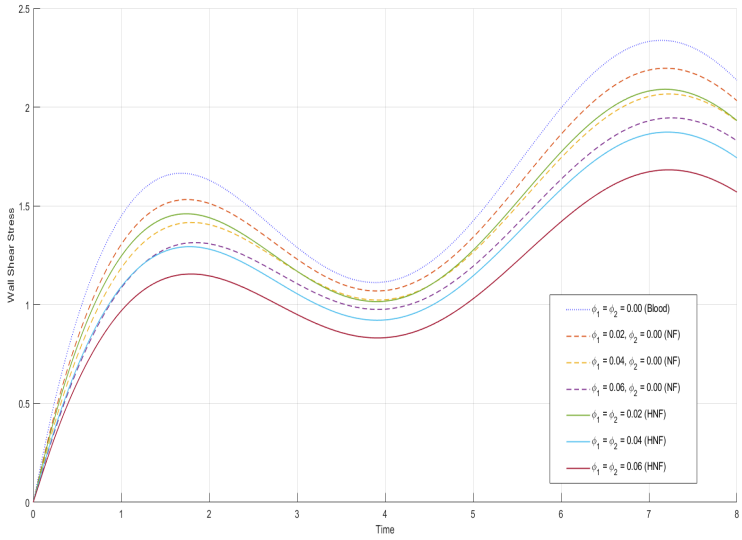

FIGURE 1.27: Wall Shear Stress response to varying concentrations of Cu and Cu-Al_2O_3 nanoparticles.

The addition of nanoparticles and hybrid nanoparticles at increasing volume fractions $(\phi_1, \phi_2 = 0.02, 0.04, 0.06)$ to the blood leads to a significant reduction in wall shear stress. Cu nanoparticles enhance the fluid's effective viscosity due to the increased particle-fluid interaction, which can dampen the flow velocity near the vessel walls, hence reducing the wall shear stress. The synergy between Cu and Al_2O_3 nanoparticles could lead to a further increase in the effective viscosity and density of the fluid, which can significantly alter the velocity profile, especially in the boundary layers. Consequently, the wall shear stress experiences a more notable reduction.

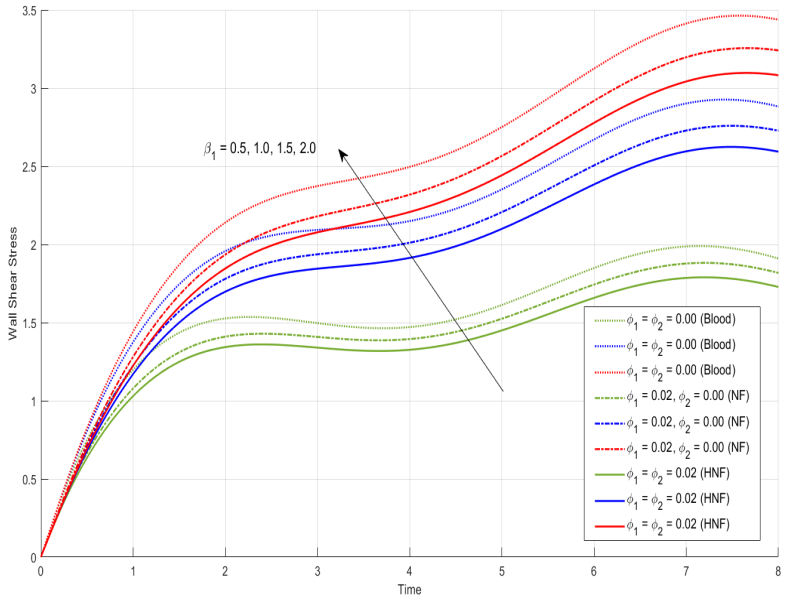

FIGURE 1.28: Wall shear stress response to varying Casson model parameter for blood, nanofluid, and hybrid nanofluid.

It is evident from Figure 1.28 that as the Casson model parameter increases $(\beta =$

0.5, 1.0, 1.5), the wall shear stress also increases for all types of fluids: ordinary blood, nanofluid, and hybrid nanofluid. This trend suggests that the fluid's resistance to flow increases with β, requiring greater stress to maintain the same flow rate. The graph also reveals that the wall shear stress is highest for ordinary blood, followed by nanofluid, and is lowest for the hybrid nanofluid. The hybrid nanofluids further enhanced viscosity and yield stress behavior, resulting in a more pronounced decrease in wall shear stress.

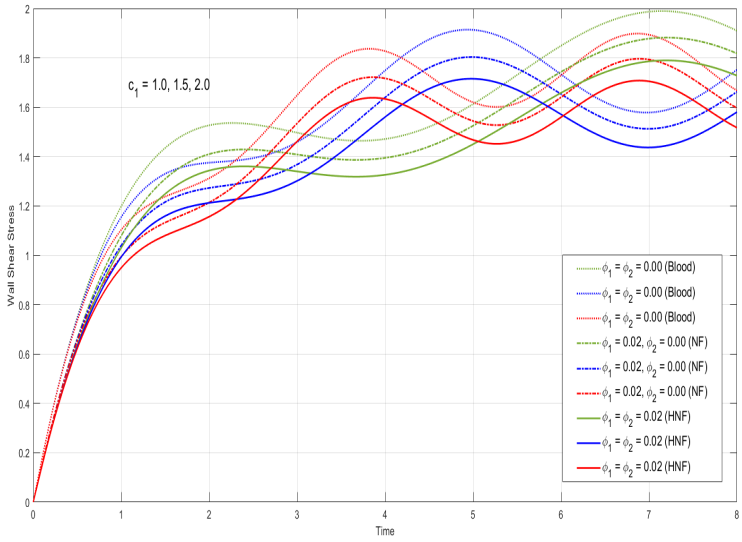

FIGURE 1.29: Wall shear stress response to varying C_1 for blood, nanofluid, and hybrid nanofluid.

Figure 1.29 presents wall shear stress (τ_w) responses to variations in the circular frequency parameter (c_1) of a pulsatile pressure gradient within an artery. As the circular frequency parameter increases from 1.0 to 2.0, the wall shear stress for all fluids – blood, nanofluid, and hybrid nanofluid – exhibits a decrease. This trend suggests that as the pulsation of the flow becomes more frequent, the average force exerted by the fluid on the arterial wall over a cycle diminishes. This effect is noticeable for the ordinary fluid, but the introduction of nanoparticles in the nanofluid and hybrid nanofluid cases appears to accentuate the effect.

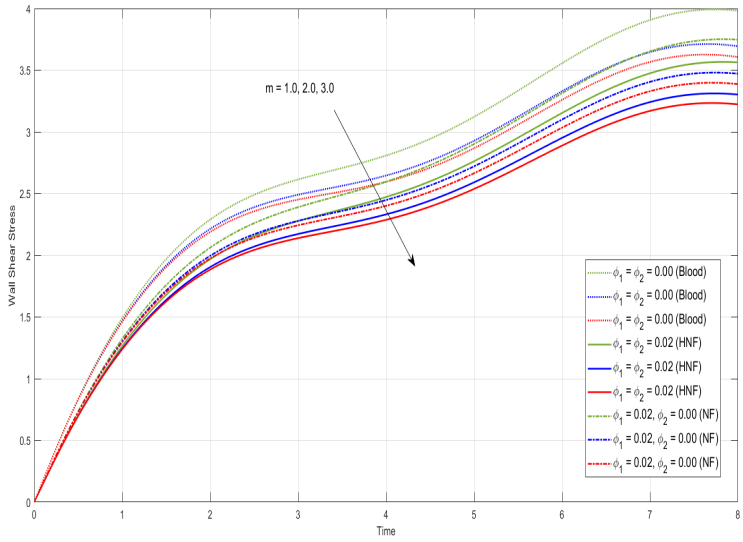

FIGURE 1.30: Wall shear stress response to varying Hall current parameter for blood, nanofluid, and hybrid nanofluid.

A decline in wall shear stress is shown in Figure 1.30 for increment in the Hall current parameter (m). As m increases from 1.0 to 3.0, the wall shear stress decreases for all fluid types. This decline indicates that the magnetic field's interaction with the electrically charged particles in the flow is exerting a force that opposes the fluid motion. In the case of blood flow, this could lead to a reduction in the velocity gradient at the vessel wall, thereby decreasing the wall shear stress.

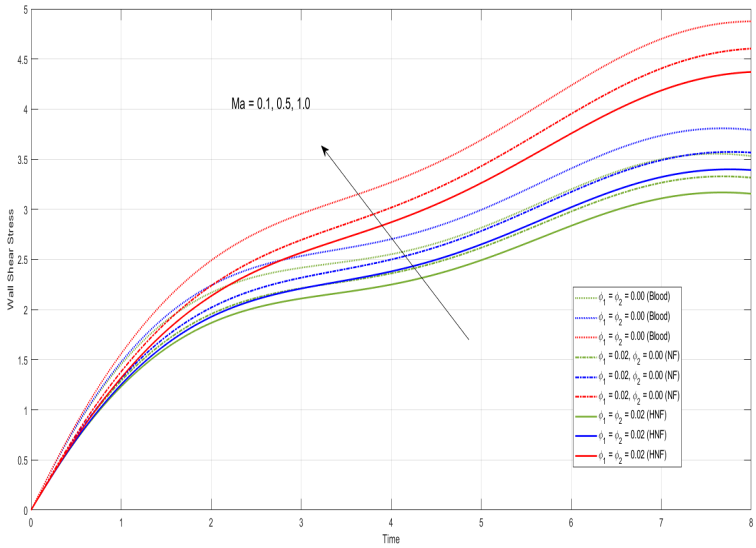

FIGURE 1.31: Wall shear stress response to varying Hartmann number for blood, nanofluid, and hybrid nanofluid.

The impact of the dimensionless Hartmann number increases from 0.1 to 1.0, there is a corresponding increase in wall shear stress (τ_w) for blood $(\phi_1 = \phi_2 = 0.0)$, Cu-blood $(\phi_1 = 0.02, \phi_2 = 0.0)$ and Cu-Al_2O_3-blood $(\phi_1 = \phi_2 = 0.02)$. This increase in Figure 1.31 is due to the magnetic field's influence, which interacts with the

charged particles in the fluid. For conducting fluids like blood, the imposed magnetic field generates a Lorentz force that opposes the motion of the fluid. Ordinary blood, without the presence of nanoparticles, possesses a lower electrical conductivity compared to nanofluids, leading to a more significant impact by the magnetic field and, therefore, higher shear stresses. Also, the nonlinear relationship between electromagnetic effects and viscous forces in these complex fluids can be perceived, suggesting that the effect of the magnetic field is more pronounced at higher values of the Hartmann number (Ma).

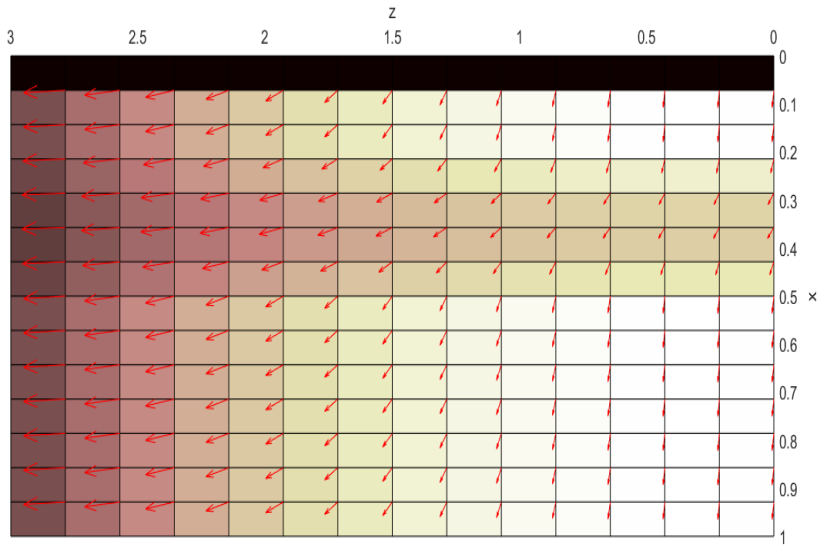

FIGURE 1.32: Quiver plot of velocity gradient in Cu-Al_2O_3-blood hybrid nanofluid flow through a stenotic artery.

The quiver plot in Figure 1.32 represents the flow profile of a hybrid nanofluid (Cu-Al_2O_3-blood) in a stenotic artery. The horizontal axis (z) represents the axial direction along the length of the artery, and the vertical axis (x) represents the radial direction from the center of the artery towards the wall. The vectors (arrows) point predominantly to the left, indicating the direction of the flow is along the axial direction of the artery. The length of the vectors represents the magnitude of the velocity at different points within the artery. Longer vectors suggest faster flow. It is noteworthy that fluid moves faster at the center of the artery due to frictional forces at the walls. This creates a velocity profile where vectors are longer in the center and shorter near the walls. Viscous fluids in cylindrical channels exhibit a velocity gradient due to no-slip condition at channel walls, with zero velocity at the walls and maximum at the center.

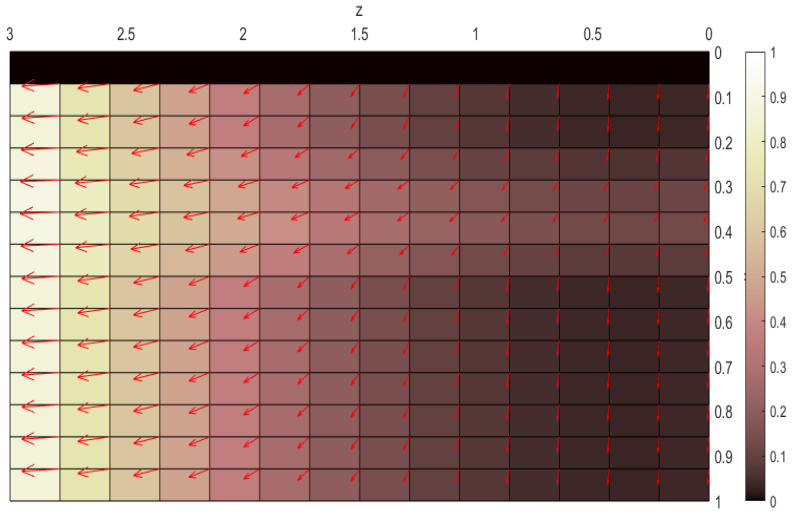

FIGURE 1.33: Quiver plot of yemperature gradient in Cu-Al_2O_3-blood hybrid nanofluid flow through a stenotic artery.

Figure 1.33 renders the temperature profile of a hybrid nanofluid flowing through a stenotic artery. The vectors (arrows) show the direction and magnitude of the temperature gradient, which can be interpreted as the direction of heat flow. The arrows' length corresponds to the temperature gradient's magnitude at different points in the artery. Longer arrows indicate steeper temperature gradients, which means that the heat transfer is more intense in those areas. Shorter arrows, on the other hand, suggest more uniform temperature areas where the heat transfer is less intense.

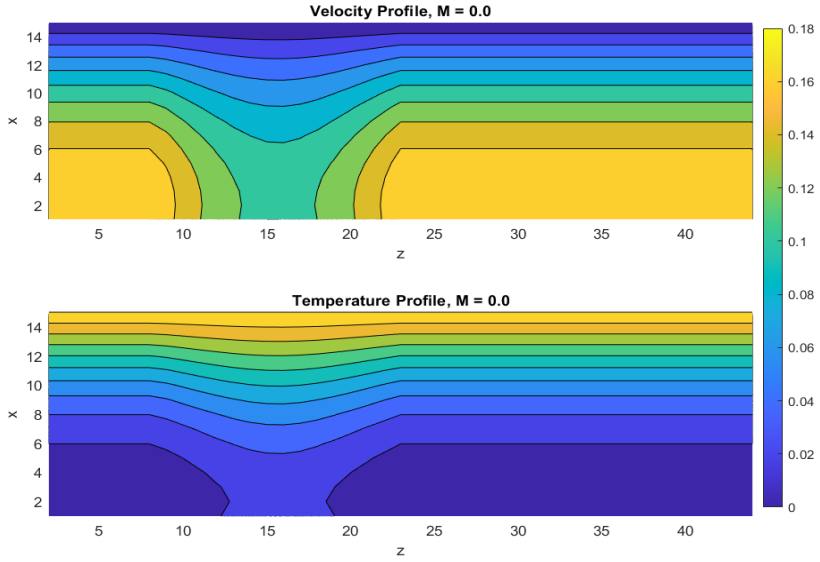

FIGURE 1.34: Velocity and temperature contours of hybrid nanofluid flow in the absence of magnetic impact $M = 0.0$.

Contour plots for dimensionless velocity and temperature profiles, with the exception of magnetic parameter M are plotted in Figure 1.34. The upper contour plot visualizes the velocity profile of a Cu-Al_2O_3-blood hybrid nanofluid as it flows

through a stenotic artery. The horizontal axis represents the axial direction (z), depicting the length of the artery, while the vertical axis (x) represents the radial direction from the artery center to its wall. In the absence of a magnetic field $(M = 0.0)$, the velocity profile exhibits a parabolic shape, characteristic of laminar flow within cylindrical vessels. Velocity is highest at the center of the artery and decreases towards the walls due to the no-slip boundary condition. Contour lines show variations in velocity magnitude, which may indicate changes caused by stenosis. The temperature distribution of the hybrid nanofluid within the stenotic artery shows a more uniform distribution compared to the velocity profile. The absence of a magnetic field $(M = 0.0)$ implies that any temperature gradients are solely due to the fluid's thermal properties and the boundary conditions. The uniformity in the temperature profile suggests effective thermal mixing, which could be enhanced by the thermal conductivity of the nanoparticles present in the hybrid nanofluid.

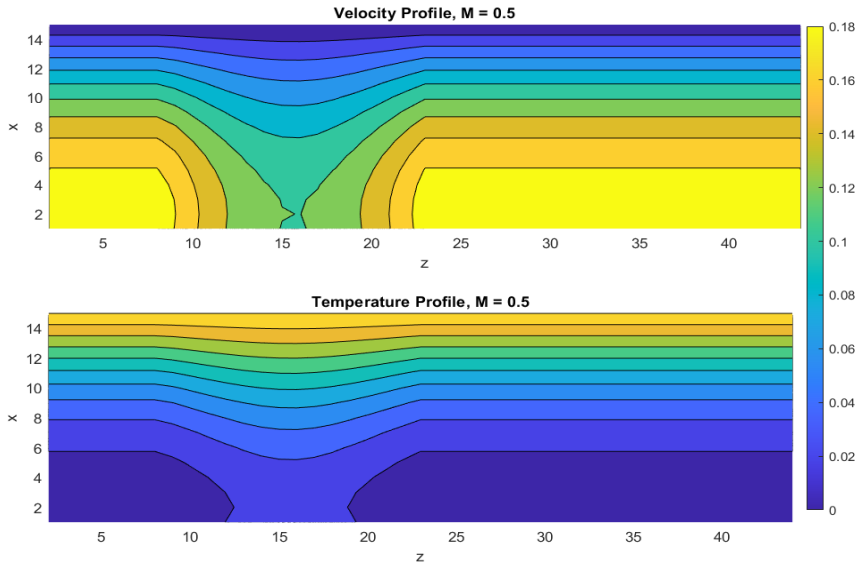

FIGURE 1.35: Velocity and temperature contours of hybrid nanofluid flow in the presence of magnetic impact $M = 0.5$.

Figure 1.35 depicts the magnetic field distribution across the flow of a hybrid nanofluid (Cu-Al_2O_3-blood). The upper contour plot illustrates the velocity profile of the hybrid nanofluid when subjected to a magnetic field characterized by a Hartmann number of 0.5. The application of the magnetic field introduces a Lorentz force that acts perpendicularly to both the magnetic field and the direction of the electric current, which in the case of blood flow, is induced by the movement of charged particles. The presence of this force typically flattens the velocity profile, reducing velocity gradients, especially near the centerline, which is consistent with the contour plot. The lower contour plot presents the temperature distribution within the artery, also under a magnetic field with $M = 0.5$. The interaction between the magnetic field and the electrically conductive fluid can influence heat transfer processes. The Lorentz force can enhance mixing within the fluid, reducing temperature gradients and leading to a more uniform temperature distribution, which can be seen in the plot.

TABLE 1.6: Table for radial distribution for the axial velocity of the ordinary fluid, Cu-blood, and Cu-Al_2O_3-blood along the radius.

$\frac{r}{R(z)}$	Blood	Cu-blood	Cu-Al_2O_3-blood
0.0	0.619304	0.515954	0.488037
0.1	0.622360	0.518325	0.490295
0.2	0.610065	0.508765	0.481193
0.3	0.594437	0.496542	0.469561
0.4	0.542609	0.455489	0.430546
0.5	0.505500	0.425676	0.402252
0.6	0.460258	0.388930	0.367416
0.7	0.343539	0.292511	0.276153
0.8	0.271405	0.231995	0.218953
0.9	0.099306	0.085530	0.080677
1.0	0.000000	0.000000	0.000000

Table 1.6 presents a comparison of axial velocity profiles for blood, Cu-blood nanofluid, and Cu-Al_2O_3-blood hybrid nanofluid within a stenotic artery. The velocity is seen to decrease with increasing radial distance, approaching zero at the artery wall. This trend is consistent with the no-slip condition at the boundary, where the fluid has zero velocity relative to the wall. The presence of nanoparticles in the nanofluid and hybrid nanofluid appears to enhance this effect, causing a more pronounced reduction in velocity compared to pure blood.

TABLE 1.7: Table for radial distribution for the temperature of the ordinary fluid, Cu-blood, and Cu-Al_2O_3-blood along radius.

$\frac{r}{R(z)}$	Blood	Cu-blood	Cu-Al_2O_3-blood
0.0	0.000667	0.000530	0.000654
0.1	0.000319	0.000258	0.000331
0.2	0.001572	0.001273	0.001535
0.3	0.003382	0.002890	0.003481
0.4	0.013923	0.013642	0.016396
0.5	0.028143	0.028920	0.034216
0.6	0.056496	0.059414	0.068576
0.7	0.203746	0.212628	0.230915
0.8	0.350292	0.359815	0.379618
0.9	0.785681	0.786146	0.794586
1.0	1.000000	1.000000	1.000000

Quantitative assessment for temperature profiles across the radial direction is stated in the Table 1.7. It is observed that for all fluids, the temperature increases with the radial distance from the centerline of the artery to the arterial wall. This increase is indicative of heat transfer from the arterial wall into the fluid, which is typically warmer at the wall due to the metabolic heat transfer from the surrounding tissues. The profiles for the nanofluid and hybrid nanofluid exhibit a similar trend but with slightly different values, suggesting that the nanoparticles may influence

the thermal conductivity and heat transfer characteristics of the fluid. The Cu-Al_2O_3-blood hybrid nanofluid shows a marginally higher temperature at corresponding radial positions compared to the Cu-blood nanofluid and pure blood.

TABLE 1.8: Comparison of axial velocity profiles for hybrid nanofluid along the radius at $z = 0.71$ and $t = 1.15$: Present study versus (Tripathi, Vasu, and Bég, 2021) and (Algehyne et al., 2023).

x	(Tripathi, Vasu, and Bég, 2021)	(Algehyne et al., 2023)	Present
0.0	0.5881	0.5890	0.5085
0.1	0.5829	0.5828	0.5109
0.2	0.5725	0.5727	0.5103
0.3	0.5518	0.5539	0.4890
0.4	0.5215	0.5259	0.4481
0.5	0.4802	0.4865	0.4185
0.6	0.4257	0.4334	0.3820
0.7	0.3549	0.3608	0.2868
0.8	0.2634	0.2689	0.2273
0.9	0.1473	0.1481	0.0836
1.0	0.0000	0.0000	0.0000

TABLE 1.9: Comparison of temperature profiles for hybrid nanofluid along the radius at $z = 0.71$ and $t = 1.15$: Present study versus (Basha et al., 2022a).

x	(Basha et al., 2022a)	Present
0.0	0.093989	0.0006628
0.1	0.101855	0.000314
0.2	0.126176	0.001481
0.3	0.168902	0.003339
0.4	0.232505	0.015540
0.5	0.318937	0.032469
0.6	0.428428	0.065463
0.7	0.558456	0.224699
0.8	0.703227	0.373057
0.9	0.853959	0.792288
1.0	1.000000	1.000000

Table 1.8 and Table 1.9 present the axial velocity and temperature values of a hybrid nanofluid along the radial direction, denoted by x and compared with the previously published results cited as (Tripathi, Vasu, and Bég, 2021), (Algehyne et al., 2023) and (Basha et al., 2022a). The values from the present study are within a close range of those reported in the literature, which suggests that the present study's methodology and results are reliable and in line with established research. The comparison indicates that the behavior of the Cu-Al_2O_3-blood hybrid nanofluid in terms of axial velocity follows a similar pattern to that observed in previous studies.

1.11 Concluding statements

In conclusion, the investigation into unsteady axisymmetric hybrid nanofluid consisting Cu-Al_2O_3-blood flow through an elliptical-shaped stenotic arteries has yielded valuable insights into the complex dynamics of blood flow in the context of cardiovascular health. By employing the Casson fluid model to characterize the non-Newtonian behavior of blood and considering the influence of factors such as pulsatile pressure gradients, magnetic fields, and nanoparticle additives, we have gained a comprehensive understanding of the multifaceted nature of flow phenomena within stenotic arteries. The subdivision of the analysis into two cases allowed for a focused exploration, with Case 1 providing a detailed examination of flow dynamics under the long-wavelength approximation, while Case 2 remains open for future exploration. Numerical computations using MATLAB, stability analyses, and graphical studies of emerging parameters have enriched our understanding of the system's behavior, revealing intricate relationships between various factors and flow characteristics.

Key Outcomes:

- **Flow characteristics:** The velocity distribution (Figure 1.9) within the artery demonstrates a maximum along the axis, gradually diminishing towards the arterial walls. In contrast, the temperature profile (Figure 1.15) exhibits the opposite behavior, with minimum values at the axis and increasing temperatures towards the walls.

- **Effect of parameters:** The study reveals significant impacts of different parameters on flow behavior. For instance, an increase in the non-Newtonian Casson model parameter amplifies velocity (Figure 1.10) while reducing the temperature profile (Figure 1.16). Higher Hall current parameter and Reynolds number reduce both velocity (Figure 1.11 and 1.13) and temperature (Figure 1.17 and 1.19) in hybrid nanofluid flow. Conversely, the magnetic field tends to enhance both velocity (Figure 1.12) and temperature (Figure 1.18). Incorporating copper (Cu) and aluminum oxide (Al_2O_3) nanoparticles into the fluid results in a decrease in velocity (Figure 1.14) and an increase in temperature (Figure 1.20).

- **Thermal enhancement:** Parameters such as the Eckert number contribute to improved thermal profiles (Figure 1.21), while the Prandtl number influences temperature reduction in hybrid nanofluid flow (Figure 1.22).

- **Local Nusselt number and wall shear stress:** Local Nusselt number improves with increases in Reynolds number (Figure 1.25) and volume fraction of nanoparticles (Figure 1.26). Increasing the volume fraction of nanoparticles (Figure 1.27), pulsatile frequency (Figure 1.29), and Hall current parameter (Figure 1.30) decreases wall shear stress, while Casson model (Figure 1.28) and magnetic parameter (Figure 1.31) increase wall shear rate.

- **Tabled findings:** Comparative tables reveal the accuracy of present results with previously published data, confirming the validity of the findings (Table 1.8 and 1.9). Axial velocity and temperature tables along the radial direction demonstrate reduced velocity but slightly increased temperature in hybrid nanofluid compared to ordinary blood and nanoparticle-infused fluids (Table 1.6 and 1.7).

These findings not only advance our understanding of blood flow dynamics in stenotic arteries but also offer valuable insights for potential biomedical applications

such as drug delivery systems. Future investigations, particularly focusing on the unfinished Case2 and further exploring the impact of nanoparticle properties, hold promise for extending our knowledge in this vital field of study.

Chapter 2

Zero Equation Turbulence Model For Cu-Al_2O_3-Blood Flow

Overview

Turbulence is the disorderly motion of fluid characterized by intense and unpredictable mixing between layers. It's often modeled using RANS equations, which have time-averaged quantities and an added Reynolds-stress tensor representing extra stress caused by velocity fluctuations. Solving the Reynolds-stress tensor is known as a closure problem.
The current chapter analyzes the blood flow hybridized by copper (Cu) and aluminum oxide (Al_2O_3) nanoparticles, with the addition of the concept of magnetohydrodynamics that includes the impact of a magnetic field using Hall current. The pulsatory axisymmetric non-Newtonian blood flow with no-slip boundary conditions is analyzed by considering the nature of the pressure gradient. The flow equations for the laminar case have been comprehensively explained in the previous chapter 1, taking into account all relevant factors.
In section 2.2, the Reynolds averaged Navier Stokes (RANS) method simplifies turbulent flows that are highly transient by averaging fluid flow variables over time. As a result, the focus is on mean flow instead of fluctuating components. The process of turbulent flow analysis involves transforming the ordinary NSEs into Reynolds averaged Navier Stokes equations (RANS), which is covered in subsection 2.2.1. The mean and fluctuating components of instantaneous flow variables, such as axial and radial velocity, are decomposed and simplified using the averaging properties are also described.
The set of equations for turbulent flow is modified to include molecular heat fluxes and eddy shear stress, which is explained using Boussinesq's eddy-viscosity concept in subsection 2.2.2. section 2.3 simplifies the flow equations by using the zero equation turbulent paradigm to simplify the fluctuation terms. The set of equations that were acquired are non-dimensionalized in section 2.4. Following the explanation in the previous chapter, these equations are then simulated numerically using the forward time central space (FTCS) method. The analysis carried out in subsection 2.5.1 and subsection 2.5.2 involved studying the fluid's momentum and wall shear stress. The conclusive findings of this study can be found in section 2.6.

2.1 Introduction

Due to the existence of unsteady and irregular motions in nature, turbulent flows are essential in many industrial equipment and engineering processes. Reynolds (Osborne, 1883) introduced a non-dimensional number that can be used when laminar flow transitions to turbulent eventuated. Reynolds number is defined as $Re = lu/\nu$, where l is the characteristic length, u is the fluid velocity, and ν is the kinematic viscosity. These occurrences happen at high values of Reynolds number and involve energy dissipation (Sarkar, Sutanu, and Lakshmanan, 1991)-(Richardson, 2010). (Boussinesq, 1877b) introduced the eddy viscosity concept as a solution to the closure problem, which involves developing a mathematical explanation of turbulent stresses.

The text discusses the recent research in non-Newtonian flow analysis using Reynolds Averaged Navier-Stokes (RANS) equations. The RANS equations are derived from the time averaging of the Navier-Stokes equations and are widely used for turbulent flow simulations. The applicability of these equations to non-Newtonian fluids requires special considerations due to the complex fluid behavior in various industrial applications. Multiple studies have developed RANS models for non-Newtonian fluids in various flow configurations. (Pinho, Oliveira, and Miranda, 2001) highlighted the importance of capturing normal stress effects in predicting viscoelastic fluid flows. (Oliveira and Pinho, 1998) demonstrated the capability of a RANS model based on nonlinear elasticity with a Peterlin approximation constitutive equation to predict shear thinning and elastic effects. Scientists have applied RANS models to specific non-Newtonian flow problems besides developing constitutive models. For instance, (Mitsoulis and Zisis, 2001) used RANS simulations to investigate the flow of viscoelastic fluids in extrusion processes, while (Chalampiari, Paras, and Karabelas, 2009) employed RANS models to study the flow of non-Newtonian fluids in stirred vessels. In their study, (Afonso, Pinho, and Oliveira, 2012) evaluated several RANS turbulence models for non-Newtonian fluid flows and pointed out the advantages and disadvantages of each model. (Comminal et al., 2019) suggested a hybrid RANS/LES (Large Eddy Simulation) method for non-Newtonian flows to merge the computational efficiency of RANS with the improved accuracy of LES in portraying turbulent structures.

Extensive research has been conducted on the application of the Prandtl mixing length and zero equation models for numerical analysis of turbulent flow in various fields, such as aerospace, mechanical engineering, and environmental fluid mechanics. These models offer an attractive approach for modeling turbulence due to their relative simplicity and computational efficiency, which makes them practical for engineering applications (Figure 2.1). However, their accuracy and limitations have been continually researched and improved upon. Among the earliest and most fundamental turbulence models was the Prandtl mixing length model, developed by Ludwig Prandtl in the early 20th century. Using the mixing length, the model relates the distance over which turbulent eddies transport momentum and scalar quantities (Schlichting and Gersten, 2016). An algebraic expression is used to relate Reynolds stress to mean velocity gradient (Wilcox et al., 1998). A number of modifications and extensions to the mixing length model are available, including the Van Driest damping function (Van Driest, 1956) and the Cebeci-Smith model (Cebeci and Smith, 1968). The zero equation model, also known as Baldwin Lomax, is an algebraic turbulence model that improves upon Prandtl's mixing length concept (Spalart and Allmaras, 1992) to account for solid boundaries' effects on turbulence. Its simplicity

and efficiency make it ideal for aerodynamic applications like airfoil and wing designs (Rumsey et al., 2004). (Versteeg, 2007) reviewed models and their applications, highlighting strengths and weaknesses. (Lilley, 1994) improved the zero equation model's accuracy in boundary layer flows.

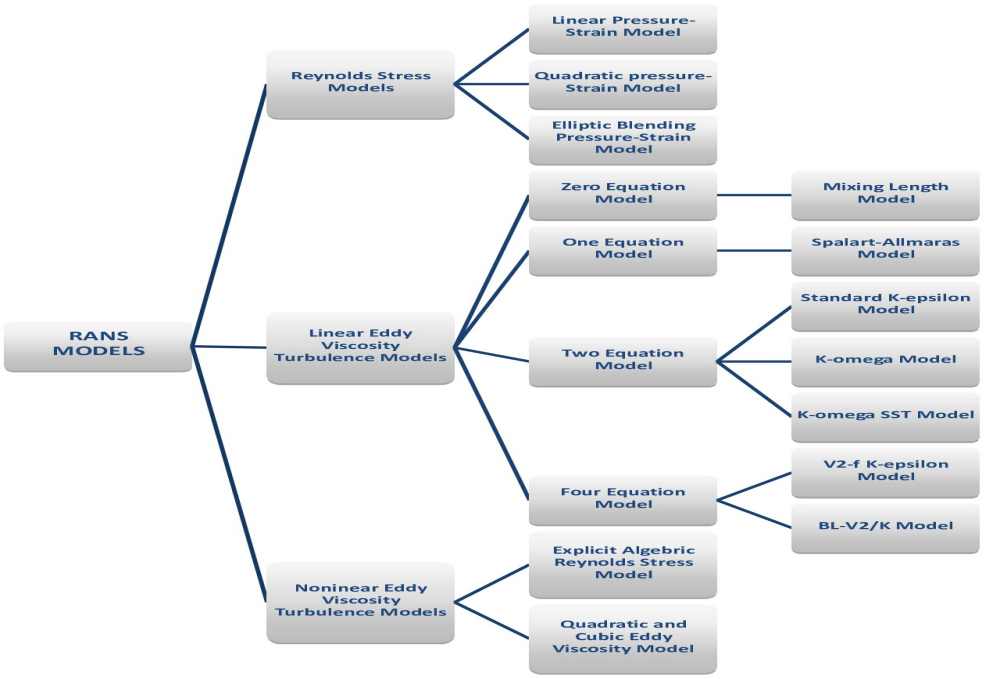

FIGURE 2.1: RANS turbulence Models

2.2 Reynolds averaged Navier Stokes equation (RANS)

A turbulence model is a collection of equations, either algebraic or differential, that help determine the transport terms of turbulence in the mean flow equations, thereby closing the system of equations. The basis of turbulence modeling is built on assumptions about turbulent processes and requires empirical input in the form of model constants or functions. Turbulence models simulate the effect of turbulence on the mean flow behavior and not the details of turbulent motion. Some of the fundamental concepts that underpin turbulence modeling include Reynolds averaging and the conservation equations.
The most popular method for handling turbulent flows is Reynolds averaging, which provides information about overall mean flow properties since the inflow's transient turbulent motions. For adding the turbulence effects, the flow variables like velocity and temperature are decomposed into the average component $\overline{\zeta}$ and the perturbed component $\acute{\zeta}$ and their sum as:

$$\zeta(x,z,t) = \overline{\zeta(x,z,t)} + \acute{\zeta}(x,z,t),$$

The average value for stationary turbulent is given by:

$$\overline{\zeta(x,z,t)} = \lim_{\Delta t \to 0} \frac{1}{\Delta t} \int_0^{\Delta t} \zeta(x,z,t)dt$$

The assumption is made that the time scale of the turbulent fluctuations is much less than Δt and Δt is much less than the time scale relative to the mean flow. The properties of averaging are:

- The average value (scalar or vector) of a constant is the constant itself.
- The time average of a time-averaged quantity is equivalent to its time average.

$$\overline{\overline{u}} = \overline{u}, \overline{\overline{w}} = \overline{w},$$

- As time averaging is a linear operator, the average of a sum equals the sum of the averages since it involves a definite integral.

$$\begin{aligned} \overline{u\acute{w}} &= \overline{u}\overline{\acute{w}} + \overline{\acute{u}\acute{w}}, \\ \overline{w^2} &= \overline{w}^2 + \overline{\acute{w}^2}, \\ \overline{u + w} &= \overline{u} + \overline{w}. \end{aligned} \tag{2.1}$$

- The time average of a fluctuating quantity is zero.

$$\overline{\acute{u}} = \overline{\acute{w}} = 0,$$

- The time average of a spatial derivative is given by

$$\begin{aligned} \overline{\frac{\partial u}{\partial z}} &= \frac{\partial \overline{u}}{\partial z}, \\ \overline{u\frac{\partial u}{\partial z}} &= \overline{u}\overline{\frac{\partial u}{\partial z}} + \overline{\acute{u}\frac{\partial \acute{u}}{\partial z}}, \\ \overline{u\acute{w}} = \overline{\acute{u}\overline{w}} &= \overline{\acute{u}\overline{u}} = \overline{\acute{w}\overline{w}}, \end{aligned}$$

2.2.1 Averaged flow equations

Considering all the dimensional variables in the flow equations are without the $(\sim)$ sign. With the concept of Reynolds time-averaging and the above expression in turbulence perturbation to the governing fluid flow equations (1.3)-(1.6) in Chapter 1. Based on the Reynolds time-average continuity equation (1.3) becomes:

$$\frac{\partial(\overline{u} + \acute{u})}{\partial r} + \frac{(\overline{u} + \acute{u})}{r} + \frac{\partial(\overline{w} + \acute{w})}{\partial z} = 0,$$

$$\overline{\frac{\partial(\overline{u} + \acute{u})}{\partial r}} + \overline{\frac{(\overline{u} + \acute{u})}{r}} + \overline{\frac{\partial(\overline{w} + \acute{w})}{\partial z}} = 0,$$

Implementing ensemble average and using properties in equation (2.1):

$$\frac{\partial \overline{u}}{\partial r} + \cancelto{0}{\frac{\partial \acute{u}}{\partial r}} + \frac{\overline{u}}{r} + \cancelto{0}{\frac{\acute{u}}{r}} + \frac{\partial \overline{w}}{\partial z} + \cancelto{0}{\frac{\partial \acute{w}}{\partial z}} = 0,$$

$$\boxed{\frac{\partial \overline{u}}{\partial r} + \frac{\overline{u}}{r} + \frac{\partial \overline{w}}{\partial z} = 0} \tag{2.2}$$

Now multiplying dimensional continuity equation (1.3) by u,

$$\frac{u^2}{r} + u\frac{\partial u}{\partial r} + u\frac{\partial w}{\partial z} = 0, \tag{2.3}$$

adding the incompressible momentum equation (1.4) and equation (2.3):

$$\frac{\partial u}{\partial t} + 2u\frac{\partial u}{\partial r} + \frac{u^2}{r} + u\frac{\partial w}{\partial z} + w\frac{\partial u}{\partial z} = -\frac{1}{\rho_{hnf}}\frac{\partial p}{\partial r} + \frac{\sigma_{hnf}\beta_0^2}{\rho_{hnf}(m^2+1)}(u+mw) + \frac{\mu_{hnf}}{\rho_{hnf}}\left(1+\frac{1}{\beta}\right)\left[\frac{\partial^2 u}{\partial r^2} + \frac{1}{r}\frac{\partial u}{\partial r} + \frac{\partial^2 u}{\partial z^2} - \frac{u}{r^2}\right], \tag{2.4}$$

simplifying using the chain rule,

$$\frac{\partial u}{\partial t} + \frac{\partial u^2}{\partial r} + \frac{u^2}{r} + \frac{\partial uw}{\partial z} = -\frac{1}{\rho_{hnf}}\frac{\partial p}{\partial r} + \frac{\sigma_{hnf}\beta_0^2}{\rho_{hnf}(m^2+1)}(u+mw) + \frac{\mu_{hnf}}{\rho_{hnf}}\left(1+\frac{1}{\beta}\right)\left[\frac{\partial^2 u}{\partial r^2} + \frac{1}{r}\frac{\partial u}{\partial r} + \frac{\partial^2 u}{\partial z^2} - \frac{u}{r^2}\right]. \tag{2.5}$$

To simulate the effects of turbulent instabilities and to simplify the analysis by taking average properties into account:

$$\overline{\frac{\partial(\overline{u}+\acute{u})}{\partial t}} + \overline{\frac{\partial(\overline{u}+\acute{u})^2}{\partial r}} + \overline{\frac{(\overline{u}+\acute{u})^2}{r}} + \overline{\frac{\partial(\overline{u}+\acute{u})(\overline{w}+\acute{w})}{\partial z}} = -\frac{1}{\rho_{hnf}}\frac{\partial p}{\partial r} + \frac{\sigma_{hnf}\beta_0^2}{\rho_{hnf}(m^2+1)}\left(\overline{(\overline{u}+\acute{u})} + m\overline{(\overline{w}+\acute{w})}\right) + \frac{\mu_{hnf}}{\rho_{hnf}}\left(1+\frac{1}{\beta}\right)\left[\frac{\partial^2\overline{(\overline{u}+\acute{u})}}{\partial r^2} + \frac{1}{r}\frac{\partial\overline{(\overline{u}+\acute{u})}}{\partial r} + \frac{\partial^2\overline{(\overline{u}+\acute{u})}}{\partial z^2} - \frac{\overline{(\overline{u}+\acute{u})}}{r^2}\right], \tag{2.6}$$

which can be re-written as

$$\frac{\partial\overline{u}}{\partial t} + \frac{\partial\overline{u}^2}{\partial r} + \overline{\frac{\partial\acute{u}^2}{\partial r}} + \frac{\overline{u}^2}{r} + \frac{\overline{\acute{u}^2}}{r} + \frac{\partial\overline{u}\overline{w}}{\partial z} + \overline{\frac{\partial(\acute{u}\acute{w})}{\partial z}} = -\frac{1}{\rho_{hnf}}\frac{\partial p}{\partial r} + \frac{\sigma_{hnf}\beta_0^2}{\rho_{hnf}(m^2+1)}(\overline{u}+m\overline{w}) + \frac{\mu_{hnf}}{\rho_{hnf}}\left(1+\frac{1}{\beta}\right)\left[\frac{\partial^2\overline{u}}{\partial r^2} + \frac{1}{r}\frac{\partial\overline{u}}{\partial r} + \frac{\partial^2\overline{u}}{\partial z^2} - \frac{\overline{u}}{r^2}\right] \tag{2.7}$$

or

$$\frac{\partial\overline{u}}{\partial t} + 2\overline{u}\frac{\partial\overline{u}}{\partial r} + \frac{\overline{u}^2}{r} + \overline{u}\frac{\partial\overline{w}}{\partial z} + \overline{w}\frac{\partial\overline{u}}{\partial z} + \overline{\frac{\partial(\acute{u}\acute{w})}{\partial z}} = -\frac{1}{\rho_{hnf}}\frac{\partial p}{\partial r} + \frac{\sigma_{hnf}\beta_0^2}{\rho_{hnf}(m^2+1)}(\overline{u}+m\overline{w}).$$

Multiplying equation (2.2) by $\overline{u}$:

$$\overline{u}\frac{\partial\overline{u}}{\partial r} + \frac{\overline{u}^2}{r} + \overline{u}\frac{\partial\overline{w}}{\partial z} = 0 \tag{2.8}$$

Based on the equation (2.8) and the equation (2.7), we can conclude the following:

$$\boxed{\begin{aligned}&\frac{\partial \overline{u}}{\partial t}+\overline{u}\frac{\partial \overline{u}}{\partial r}+\overline{w}\frac{\partial \overline{u}}{\partial z}=-\frac{1}{\rho_{hnf}}\frac{\partial p}{\partial r}+\frac{\sigma_{hnf}\beta_0^2}{\rho_{hnf}(m^2+1)}(\overline{u}+m\overline{w})\\&+\frac{\mu_{hnf}}{\rho_{hnf}}\left(1+\frac{1}{\beta}\right)\left[\frac{\partial^2\overline{u}}{\partial r^2}+\frac{1}{r}\frac{\partial \overline{u}}{\partial r}+\frac{\partial^2\overline{u}}{\partial z^2}-\frac{\overline{u}}{r^2}\right]-\rho_{hnf}\frac{\partial}{\partial z}\overline{(\acute{u}\acute{w})}\end{aligned}} \tag{2.9}$$

Now multiplying dimensional continuity equation (1.3) by w and adding to equation (1.5),

$$\begin{aligned}\frac{\partial w}{\partial t}+u\frac{\partial w}{\partial r}+w\frac{\partial u}{\partial r}+\frac{uw}{r}+2w\frac{\partial w}{\partial z}=&-\frac{1}{\rho_{hnf}}\frac{\partial p}{\partial z}+\frac{\sigma_{hnf}\beta_0^2}{\rho_{hnf}(m^2+1)}(w-mu)\\&+\frac{\mu_{hnf}}{\rho_{hnf}}\left(1+\frac{1}{\beta}\right)\left[\frac{\partial^2 w}{\partial r^2}+\frac{1}{r}\frac{\partial w}{\partial r}+\frac{\partial^2 w}{\partial z^2}\right],\end{aligned} \tag{2.10}$$

or

$$\begin{aligned}\frac{\partial w}{\partial t}+\frac{\partial uw}{\partial r}+\frac{uw}{r}+2w\frac{\partial w^2}{\partial z}=&-\frac{1}{\rho_{hnf}}\frac{\partial p}{\partial z}+\frac{\sigma_{hnf}\beta_0^2}{\rho_{hnf}(m^2+1)}(w-mu)\\&+\frac{\mu_{hnf}}{\rho_{hnf}}\left(1+\frac{1}{\beta}\right)\left[\frac{\partial^2 w}{\partial r^2}+\frac{1}{r}\frac{\partial w}{\partial r}+\frac{\partial^2 w}{\partial z^2}\right],\end{aligned} \tag{2.11}$$

After applying the average to both sides of the equation mentioned above, we add turbulence perturbations:

$$\begin{aligned}\overline{\frac{\partial(\overline{w}+\acute{w})}{\partial t}}+\overline{\frac{\partial(\overline{u}+\acute{u})(\overline{w}+\acute{w})}{\partial r}}+\overline{\frac{\partial(\overline{w}+\acute{w})^2}{\partial z}}+\overline{\frac{(\overline{u}+\acute{u})(\overline{w}+\acute{w})}{r}}=&-\frac{1}{\rho_{hnf}}\frac{\partial p}{\partial z}+\\\frac{\sigma_{hnf}\beta_0^2}{\rho_{hnf}(m^2+1)}\left(\overline{(\overline{w}+\acute{w})}-m\overline{(\overline{u}+\acute{u})}\right)+\frac{\mu_{hnf}}{\rho_{hnf}}\left(1+\frac{1}{\beta}\right)&\left[\frac{\partial^2\overline{(\overline{w}+\acute{w})}}{\partial r^2}+\right.\\\left.\frac{1}{r}\frac{\partial\overline{(\overline{w}+\acute{w})}}{\partial r}+\frac{\partial^2\overline{(\overline{w}+\acute{w})}}{\partial z^2}\right],\end{aligned} \tag{2.12}$$

Using the properties provided in equation (2.1) and reducing the complexities in the same manner as done for the momentum equation along the radial direction.

$$\begin{aligned}\frac{\partial\overline{w}}{\partial t}+\frac{\partial(\bar{u}\bar{w})}{\partial r}+\frac{\partial(\overline{\acute{u}\acute{w}})}{\partial r}+\frac{\overline{uw}}{r}+\frac{\overline{\acute{u}\acute{w}}}{r}+\frac{\partial(\overline{\acute{w}^2})}{\partial z}+\frac{\partial(\overline{w^2})}{\partial z}=&-\frac{1}{\rho_{hnf}}\frac{\partial p}{\partial z}+\\\frac{\sigma_{hnf}\beta_0^2}{\rho_{hnf}(m^2+1)}(\overline{w}-m\overline{u})+\frac{\mu_{hnf}}{\rho_{hnf}}\left(1+\frac{1}{\beta}\right)&\left[\frac{\partial^2\overline{w}}{\partial r^2}+\frac{1}{r}\frac{\partial\overline{w}}{\partial r}+\frac{\partial^2\overline{w}}{\partial z^2}\right],\end{aligned} \tag{2.13}$$

or,

$$\begin{aligned}\frac{\partial\overline{w}}{\partial t}+\overline{u}\frac{\partial\overline{w}}{\partial r}+\overline{w}\frac{\partial\overline{u}}{\partial r}+\frac{\bar{u}\bar{w}}{r}+2\overline{w}\frac{\partial\overline{w}}{\partial z}+\frac{\partial(\overline{\acute{u}\acute{w}})}{\partial r}=&-\frac{1}{\rho_{hnf}}\frac{\partial p}{\partial z}+\\\frac{\sigma_{hnf}\beta_0^2}{\rho_{hnf}(m^2+1)}(\overline{w}-m\overline{u})+\frac{\mu_{hnf}}{\rho_{hnf}}\left(1+\frac{1}{\beta}\right)&\left[\frac{\partial^2\overline{w}}{\partial r^2}+\frac{1}{r}\frac{\partial\overline{w}}{\partial r}+\frac{\partial^2\overline{w}}{\partial z^2}\right],\end{aligned} \tag{2.14}$$

multiplying equation (2.2) by $\overline{w}$,

$$\overline{w}\frac{\partial \overline{u}}{\partial r} + \frac{\overline{uw}}{r} + \overline{w}\frac{\partial \overline{w}}{\partial z} = 0 \tag{2.15}$$

After subtracting equation (2.15) from equation (2.14), we obtain a new expression:

$$\begin{aligned}\frac{\partial \overline{w}}{\partial t} + \overline{u}\frac{\partial \overline{w}}{\partial r} + \overline{w}\frac{\partial \overline{w}}{\partial z} &= -\frac{1}{\rho_{hnf}}\frac{\partial p}{\partial z} + \frac{\sigma_{hnf}\beta_0^2}{\rho_{hnf}(m^2+1)}(\overline{w} - m\overline{u}) \\ &+ \frac{\mu_{hnf}}{\rho_{hnf}}\left(1+\frac{1}{\beta}\right)\left[\frac{\partial^2 \overline{w}}{\partial r^2} + \frac{1}{r}\frac{\partial \overline{w}}{\partial r} + \frac{\partial^2 \overline{w}}{\partial z^2}\right] - \rho_{hnf}\frac{\partial}{\partial r}\overline{(\acute{u}\acute{w})}\end{aligned} \tag{2.16}$$

2.2.2 Concept of eddy viscosity

The above equations (2.2), (2.9), and (2.16) are called Reynolds Averaged Navier Stokes (RANS) equations. The term $\overline{(\acute{u}\acute{w})}$ refers to eddy shear stress. Boussinesq's eddy-viscosity concept assumes that turbulent stresses are proportional to the mean velocity gradient, similar to viscous stresses in laminar flows. Instead of molecules, eddies are used to carry thermal energy and momentum. The concept of eddy viscosity is best understood in comparison to molecular transport of momentum.
Eddy shear stress is typically defined as the Reynolds-stress tensor divided by the density term, and it accounts for the influence of turbulent motion on mean stresses. The Reynolds-stress tensor is symmetric, the diagonal components are normal stresses, and the off-diagonal components are shear stresses and expressed as:

$$\overline{(\acute{u}\acute{w})} = \begin{bmatrix} \overline{\acute{u}^2} & \overline{\acute{u}\acute{v}} & \overline{\acute{u}\acute{w}} \\ \overline{\acute{v}\acute{u}} & \overline{\acute{v}^2} & \overline{\acute{v}\acute{w}} \\ \overline{\acute{w}\acute{u}} & \overline{\acute{v}\acute{w}} & \overline{\acute{w}^2} \end{bmatrix}$$

The normal stress is denoted in the diagonal terms, while the shear stress is denoted in the symmetric upper and lower diagonal terms. Consequently, six independent elements are created by Reynold averaging. Reynold normal stresses $(\overline{\acute{u}^2}, \overline{\acute{v}^2}, \overline{\acute{w}^2})$ and Reynold shear stresses $(\overline{\acute{u}\acute{v}}, \overline{\acute{v}\acute{w}}, \overline{\acute{u}\acute{w}})$ are six independent elements and is called as a closure problem. It is necessary to model the Reynolds stresses in terms of mean flow quantities in order to resolve this issue. The challenge with closing the Reynolds-averaged Navier-Stokes equations is to express the Reynolds-stress tensor as a function of the mean-field and/or other variables, mainly through models. In general, turbulence models are developed to represent high-order moments of the velocity fluctuations in terms of lower-order moments. This can be achieved directly, as in the case of eddy-viscosity models, or indirectly, through models that solve additional partial differential equations.

2.3 Zero equation turbulence model

The zero equation model is a type of Reynolds-averaged Navier-Stokes (RANS) or Large Eddy Simulation (LES) model that estimates turbulence properties based on flow characteristics without solving any set of PDEs for turbulent quantities such as turbulent kinetic energy or turbulent dissipation. This model can be combined with the Prandtl mixing length and Boussinesq approximation to model turbulence in simplified flow situations. These models rely on the same fundamental assumptions and simplifications, which makes them suitable for straightforward cases but not for

capturing complex turbulence behaviors. The Reynolds stress term is modeled with their momentum for a distance l and turbulent velocity v_t by:

$$-\rho\acute{u}\acute{w} = \rho v_t l \frac{d\overline{u}}{dr}$$

This model postulates that the mixing velocity v_t is of the same order of magnitude as the horizontal fluctuating velocities of the eddies.

$$v_t \approx u' \approx w' \approx l \left| \frac{du}{dr} \right| \tag{2.17}$$

In terms of a shear flow, the eddy or turbulent viscosity can be considered

$$\mu_t = \rho v_t l \left| \frac{du}{dr} \right|$$

According to Prandtl, momentum is transferred by eddies that transport in the z-direction at a certain distance (l) without interactions and then get mixed with the existing fluid at new locations (McComb, 1990). Prandtl deduced that:

$$\rho\acute{u}\acute{w} = -\rho l^2 \left(\frac{\partial \overline{u}}{\partial r} \right)^2$$

$l = nr$ where $n = 0.4$ is known as Von-Karman constant (McComb, 1990). so we have

$$-\rho\acute{u}\acute{w} = \rho n^2 r^2 \left(\frac{\partial \overline{u}}{\partial r} \right)^2 \tag{2.18}$$

Incorporating Prandtl mixing length (PML) hypothesis in equation (2.18) in equations (2.9), and (2.16), we have

$$\frac{\partial \overline{u}}{\partial t} + \overline{u}\frac{\partial \overline{u}}{\partial r} + \overline{w}\frac{\partial \overline{u}}{\partial z} = -\frac{1}{\rho_{hnf}}\frac{\partial p}{\partial r} + \frac{\sigma_{hnf}\beta_0^2}{\rho_{hnf}(m^2+1)}(\overline{u} + m\overline{w}) + \frac{\mu_{hnf}}{\rho_{hnf}}\left(1 + \frac{1}{\beta}\right)\left[\frac{\partial^2 \overline{u}}{\partial r^2} + \frac{1}{r}\frac{\partial \overline{u}}{\partial r} + \frac{\partial^2 \overline{u}}{\partial z^2} - \frac{\overline{u}}{r^2}\right] + \frac{\partial}{\partial z}\left(n^2 z^2 \left(\frac{\partial \overline{u}}{\partial z}\right)^2\right), \tag{2.19}$$

$$\frac{\partial \overline{w}}{\partial t} + \overline{u}\frac{\partial \overline{w}}{\partial r} + \overline{w}\frac{\partial \overline{w}}{\partial z} = -\frac{1}{\rho_{hnf}}\frac{\partial p}{\partial z} + \frac{\sigma_{hnf}\beta_0^2}{\rho_{hnf}(m^2+1)}(\overline{w} - m\overline{u}) + \frac{\mu_{hnf}}{\rho_{hnf}}\left(1 + \frac{1}{\beta}\right)\left[\frac{\partial^2 \overline{w}}{\partial r^2} + \frac{1}{r}\frac{\partial \overline{w}}{\partial r} + \frac{\partial^2 \overline{w}}{\partial z^2}\right] + \frac{\partial}{\partial r}\left(n^2 r^2 \left(\frac{\partial \overline{u}}{\partial r}\right)^2\right), \tag{2.20}$$

Equation (2.2) and (2.19) and (2.20) are the dimensional ultimate form of Reynolds Navier Stokes equation.

2.4 Dimensionless scaling

For dimensional analysis, the following set of dimensionless variables are considered:

$$r = \frac{\bar{r}}{l_0}, \quad z = \frac{\bar{z}}{l_0}, \quad u = \frac{\bar{u}}{u_0}, \quad w = \frac{\bar{w}}{u_0}, \quad t = \frac{\mu_0 \bar{t}}{l_0}, \quad p = \frac{\bar{p}}{\rho u_o}$$

Where r and z are the dimensional radial and axial axes, respectively, u and w are the corresponding radial and axial velocity profiles, t is dimensional time, p is dimensional pressure, u_0 is the reference velocity, and l_0 is the reference length. By applying the radial coordinate transformation to equation (2.19) and equation (2.20), we arrive at:

$$\frac{\partial u}{\partial t} = -\left(\frac{u}{R(z)}\frac{\partial u}{\partial x} + w\frac{\partial u}{\partial z}\right) + \frac{\rho_f}{\rho_{hnf} Re}\left[\frac{\mu_{hnf}}{\mu_f}\left(1+\frac{1}{\beta}\right)\left(\frac{1}{R(z)^2}\left(\frac{\partial^2 u}{\partial x^2} + \frac{1}{x}\frac{\partial u}{\partial x}\right) + \frac{\partial^2 u}{\partial z^2} - \frac{u}{xR(z)}\right) + \frac{\sigma_{hnf} M^2 u}{\sigma_f (m^2+1)}\right] + \frac{2n^2}{R(z)}\left[x\left(\frac{\partial u}{\partial x}\right)^2 + x^2 \frac{\partial u}{\partial x}\frac{\partial^2 u}{\partial x^2}\right] \quad (2.21)$$

$$\frac{\partial w}{\partial t} = -\left(\frac{u}{R(z)}\frac{\partial w}{\partial x} + w\frac{\partial w}{\partial z}\right) + \frac{\rho_f}{\rho_{hnf}}\left(A_0(1+ecos(c_1 t))\right) + \frac{\rho_f}{\rho_{hnf} Re}\left[\frac{\mu_{hnf}}{\mu_f}\left(1+\frac{1}{\beta}\right)\left(\frac{1}{R(z)^2}\left(\frac{\partial^2 w}{\partial x^2} + \frac{1}{x}\frac{\partial w}{\partial x}\right) + \frac{\partial^2 w}{\partial z^2}\right) + \frac{\sigma_{hnf} M^2 w}{\sigma_f (m^2+1)}\right] + \frac{2n^2}{R(z)}\left[x\left(\frac{\partial w}{\partial x}\right)^2 + x^2 \frac{\partial w}{\partial x}\frac{\partial^2 w}{\partial x^2}\right] \quad (2.22)$$

2.5 Flow analysis

The study focuses on a 2D time-dependent turbulent flow of a hybrid nanofluid containing Cu and Al_2O_3 nanoparticles. The non-Newtonian Casson model was used to describe blood flow through a constricted arterial section. The Reynolds-averaged Navier-Stokes equations were modified to incorporate the eddy shear stress term, which is modeled using the Zero equation turbulent model. The resulting equations are nondimensionalized for simplicity. Numerical computation is done using forward time central space (FTCS) in two-dimensional space and one-dimensional time, a differentiation scheme already mentioned in detail in Section 1.9 of Chapter 1. The equations 2.21 and 2.22 for 2D in space are as follows:

$$w(j,m,n+1) = w(j,m,n) + \Delta t \frac{\rho_f}{\rho_{hnf}}\left[A_0\left(1+e\cos(c_1 t(n))\right) + \frac{\mu_{hnf}}{\mu_f Re}\frac{1}{(R(m))^2}\left(1+\frac{1}{\beta}\right)\times \left(\frac{w(j+1,m,n) - w(j,m,n) + w(j-1,m,n)}{\Delta x^2} + \frac{1}{x(j)}\frac{w(j+1,m,n) - w(j-1,m,n)}{2\Delta x}\right) + \frac{M^2}{m^2+1}\frac{\sigma_{hnf}}{\sigma_f Re} w(j,m,n)\right] - \Delta t\left[\frac{u(j,m,n)}{2\Delta x R(m)}\left(w(j+1,m,n) - w(j-1,m,n)\right)\right] + \frac{2\Delta t n^2}{R(m)}\left[\frac{x(j)}{4(\Delta x)^2}\left(\left(w(j+1,m,n)\right)^2 + \left(w(j-1,m,n)\right)^2 - 2w(j+1,m,n)w(j-1,m,n)\right) + \frac{x(j)^2}{2(\Delta x)^3}\left(w(j+1,m,n) - w(j-1,m,n)\right)\times\left(w(j+1,m,n) - w(j,m,n) + w(j-1,m,n)\right)\right]$$

with initial and boundary conditions:

$$w(j,m,1) = 0at \qquad t = 0,$$

$$w(j+1,m,n) = w(j,m,n), \qquad at \;\; x = 0,$$

$$w(J,n) = 0 \qquad at \;\; x = 1. \tag{2.23}$$

This segment delves into the graphical analysis of the fluid momentum, together with the associated wall shear stress, for turbulent flows, using mean velocity as a key parameter. Additionally, the impact of emerging parameters is examined for high Reynolds number.

2.5.1 Analysis of momentum

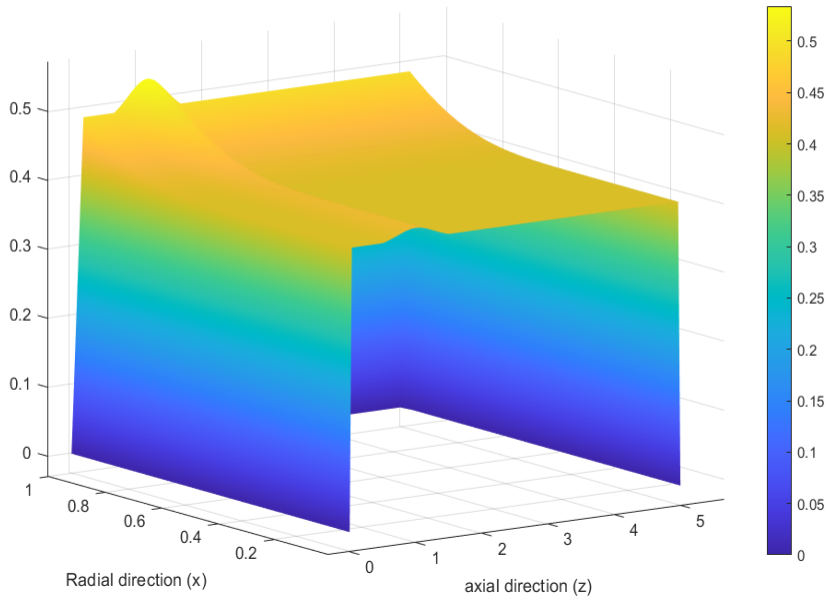

FIGURE 2.2: Simulated Axial Velocity Profile (U_x) at Stenosis in a non-Newtonian Blood Flow with Parabolic Inlet Conditions.

Figure 2.2 illustrates a three-dimensional representation of the velocity field within a stenotic artery, considering an axisymmetric, time-dependent Casson blood flow. The simulation incorporates complex dynamics using the Reynolds-Averaged Navier-Stokes (RANS) equations and is further refined by the Prandtl mixing length turbulence model. This advanced model captures the velocity distribution along both radial (x) and axial (z) directions within the artery. The velocity magnitude within the artery can be inferred from the color gradient, where warmer colors indicate higher velocities. The flattening of the velocity profile in the central axial region indicates a developed turbulent flow, with reduced velocity gradients suggesting significant momentum exchange due to turbulence. The abrupt decrease in velocity near the

radial edges indicates the existence of a turbulent boundary layer, where the flow encounters viscous forces near the arterial walls.

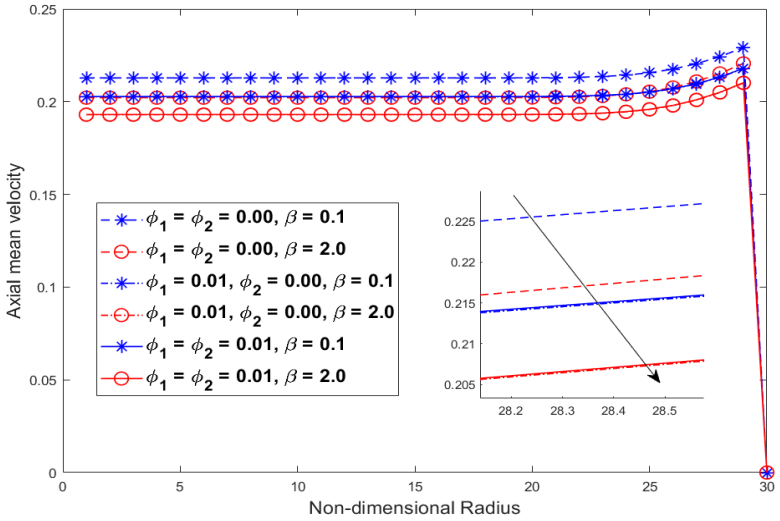

FIGURE 2.3: Blood, Cu-blood and Cu-Al_2O_3-blood axial mean velocity profiles against variation in Casson model parameter.

Axial mean velocity profiles of blood modeled as a Casson fluid through a stenotic artery with variation in casson model parameter $\beta = 0.1, 2.0$ is demonstrated in Figure 2.3. As the Casson fluid parameter rises, indicating an increase in non-Newtonian effects, the velocity profile reduces noticeably. This pattern suggests that when blood is modeled as a non-Newtonian fluid with Casson properties, it shows greater resistance to flow, especially when nanoparticles (NF) and hybrid nanoparticles (HNF) are present, as compared to regular fluids.

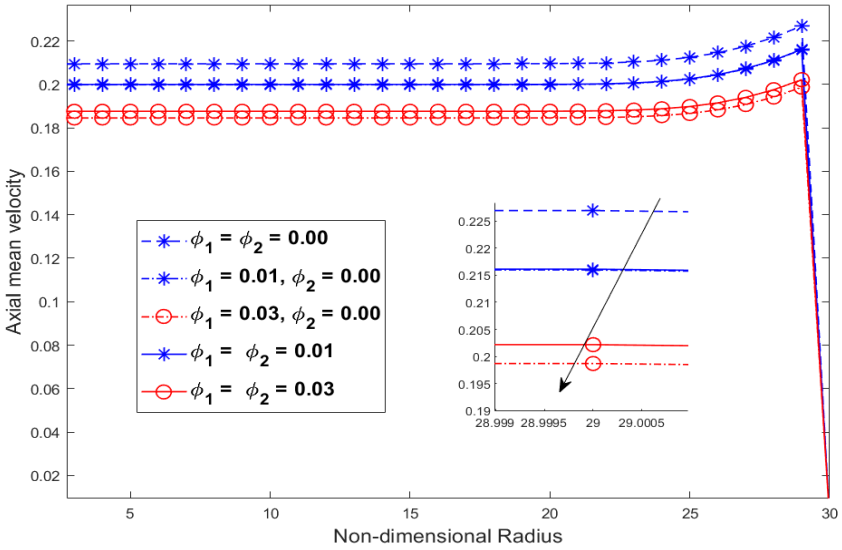

FIGURE 2.4: Axial Velocity Profile against volume fraction of Cu and Al_2O_3 nanoparticles.

The graph presented in Figure 2.4 depicts the velocity of blood within an artery with $Re = 4200$. The graph indicates that the addition of copper and aluminum oxide nanoparticles to the fluid results in a decrease in its speed, indicating an increase in the fluid's effective viscosity. However, the presence of nanoparticles also leads to a rise in the fluid's resistance to turbulent motion, which results in a reduction of velocities in the NF and HNF regions compared to the ordinary fluid. The turbulence intensity is reduced and the turbulent viscosity is changed as the volume fraction of nanoparticles increases, resulting in a continuous decrease in velocity. This modification is particularly noticeable near the wall, where the velocity gradient is the most significant due to the no-slip condition.

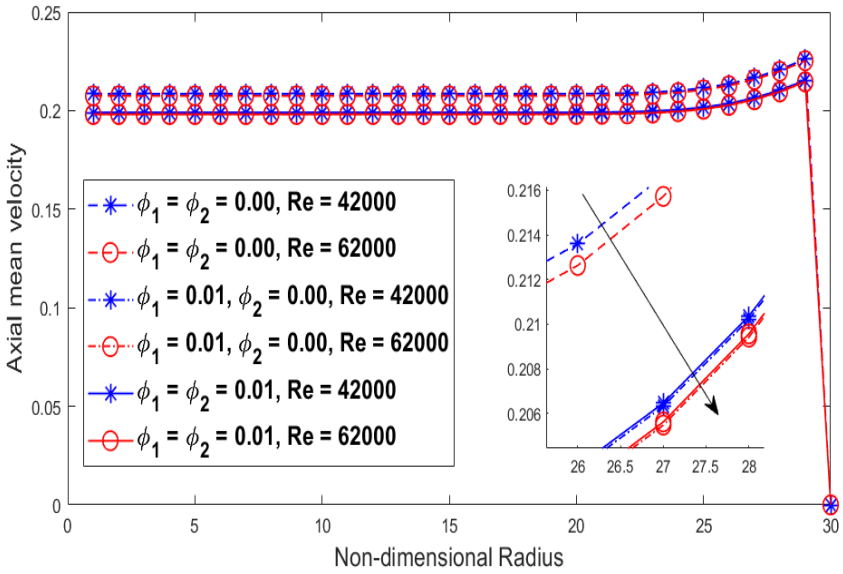

FIGURE 2.5: Axial Velocity Profile against volume fraction of Cu and Al_2O_3 nanoparticles.

The data presented in Figure 2.5 indicates that the axial mean velocity profile decreases as the Reynolds numbers of 42000 and 62000 increase. This suggests that turbulence has a greater impact on the velocity profiles of nanofluids (NF) and hybrid nanofluids (HNF) as compared to ordinary fluids, especially at higher Reynolds numbers. It is interesting to note that ordinary fluids exhibit a lesser reduction in velocity with increasing Reynolds number than their nanoparticle-containing counterparts, which implies that the addition of nanoparticles makes the flow more susceptible to changes in Reynolds number. At higher Reynolds numbers, turbulence intensifies these effects, leading to a flatter velocity profile in the core of the flow and steeper gradients near the wall due to the presence of a turbulent boundary layer. The effect of turbulence on the velocity profiles of nanofluids and hybrid nanofluids suggests that the particles may be interacting with the turbulent eddies, thereby enhancing energy dissipation and reducing the flow velocity more significantly than in ordinary fluids.

TABLE 2.1: Table for radial distribution for the mean axial velocity of the ordinary fluid, Cu-blood, and Cu-Al_2O_3-blood along the radius.

$\frac{r}{R(z)}$	Blood	Cu-blood	Cu-Al_2O_3-blood
0.0	0.354290	0.337628	0.337858
0.1	0.354290	0.337628	0.337858
0.2	0.354290	0.337628	0.337858
0.3	0.354290	0.337628	0.337858
0.4	0.354291	0.337629	0.337859
0.5	0.354332	0.337658	0.337888
0.6	0.355041	0.338215	0.338447
0.7	0.359801	0.342241	0.342483
0.8	0.376372	0.356995	0.357261
0.9	0.412034	0.389828	0.390132
1.0	0.000000	0.000000	0.000000

Table 2.1 provided delineates the mean axial velocities of three different fluid types as they flow through an axisymmetric stenotic artery across various radial positions from the central axis $(r/R = 0)$ to the arterial wall $(r/R = 1)$. For fully developed turbulent flow, the velocity profile across the artery radius is flatter than that of laminar flow. The reason for the flattening is that turbulent flows have an increased mixing and momentum transfer throughout the flow. This is due to the existence of eddies and swirls, which transport fluid particles across the streamlines. The impact of this effect is most significant in areas that are further away from the walls, where the flow is not directly impacted by the no-slip conditions.

TABLE 2.2: Comparison of laminar and turbulent velocity profiles for hybrid nanofluid $(Cu$-$Al_2O_3)$-Blood flow in a stenotic artery.

$\frac{r}{R(z)}$	Laminar velocity for HNF	Turbulent mean velocity for HNF
0.0	0.354290	0.337858
0.1	0.354290	0.337858
0.2	0.354290	0.337858
0.3	0.354290	0.337858
0.4	0.354291	0.337859
0.5	0.354332	0.337888
0.6	0.355041	0.338447
0.7	0.359801	0.342483
0.8	0.376372	0.357261
0.9	0.412034	0.390132
1.0	0.000000	0.000000

From Table 2.2, the increase in velocity from $r/R(z) = 0.4$ to 0.9 can be attributed to the turbulent eddies that are active in this region. These eddies tend to move momentum from the high-velocity core toward the lower-velocity regions near the wall. However, as the flow approaches the wall, the influence of viscosity becomes more

significant, the turbulent fluctuations are damped, and the flow aligns more with the no-slip boundary condition, leading to a rapid decrease in velocity as $r/R(z)$ approaches 1.

2.5.2 Analysis of wall shear stress

In the zero-equation turbulence model, turbulent wall shear stress is estimated without resolving additional turbulence-specific transport equations. This model uses a mixing length theory to compute turbulent viscosity, ν_t based on the distance from the wall and the velocity gradient. The wall shear stress τ_w, for an axisymmetric flow can be expressed as:

$$\tau_w = \rho.(\nu + \nu_t)\frac{dw}{dr}\Big|_{r=0}. \tag{2.24}$$

According to zero-equation turbulence model, the turbulent viscosity ν_t is defined by:

$$\nu_t = l_m^2\left|\frac{dw}{dr}\right|.$$

where l_m is characteristic/mixing length scale and dw/dr is velocity gradient near the wall.

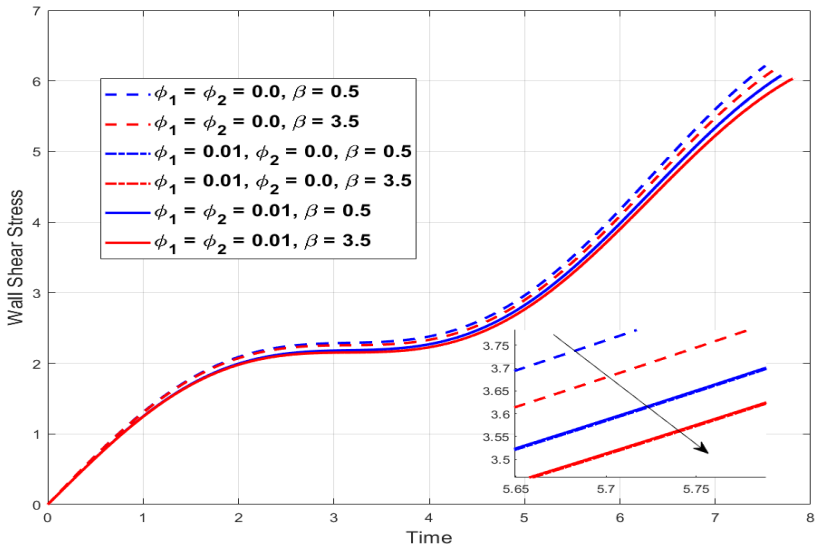

FIGURE 2.6: Turbulent wall shear stress against Casson model parameter.

The WSS evolution in a turbulent flow through a stenotic artery over time is shown in Figure 2.6. Due to the pulsatile nature of the flow, the WSS generally increases with time. However, an increase in the Casson model parameter results in a decrease in WSS. This parameter characterizes the non-Newtonian behavior of blood and indicates that as blood becomes more viscous, the force on the artery wall decreases. Moreover, the turbulence near the wall is affected by the presence of nanoparticles and hybrid nanofluids, which results in a lower WSS compared to the ordinary fluid. These additives increase the fluid's resistance to flow.

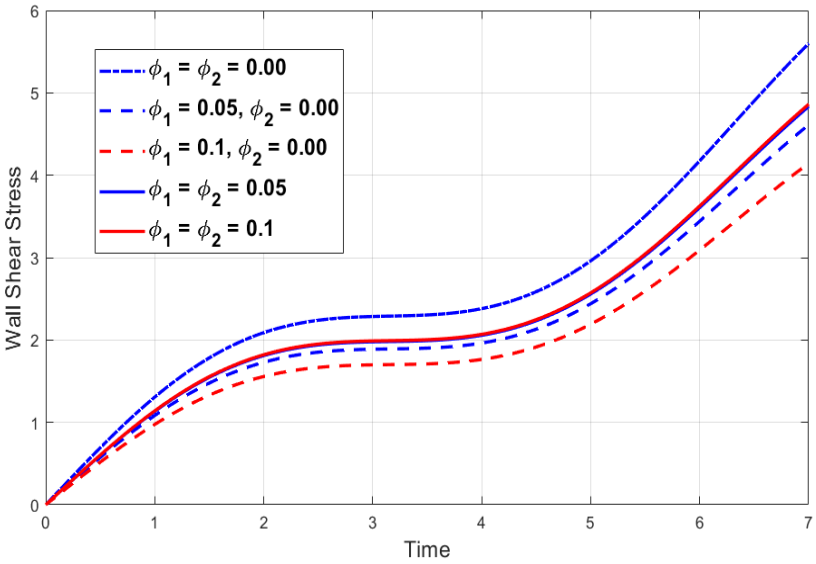

FIGURE 2.7: Turbulent wall shear stress against volume fraction of Cu and Al_2O_3 nanoparticles.

The temporal profile of the wall shear stress (WSS) in an artery with Casson blood flow under a turbulent regime can be seen in Figure 2.7. It has been observed that the WSS increases over time, which reflects the pulsatile nature of blood flow and is often related to the rhythmic pumping action of the heart. It is noteworthy that the WSS is greater for ordinary blood when compared to blood with nanoparticles (nanofluid) and hybrid nanofluid. Turbulence typically intensifies WSS by introducing complex flow patterns that increase momentum exchange at the arterial wall. However, the presence of nanoparticles seems to tone down this effect, potentially by augmenting the fluid's viscosity or altering flow structures, which in turn reduces the turbulence-induced shear forces on the vessel walls.

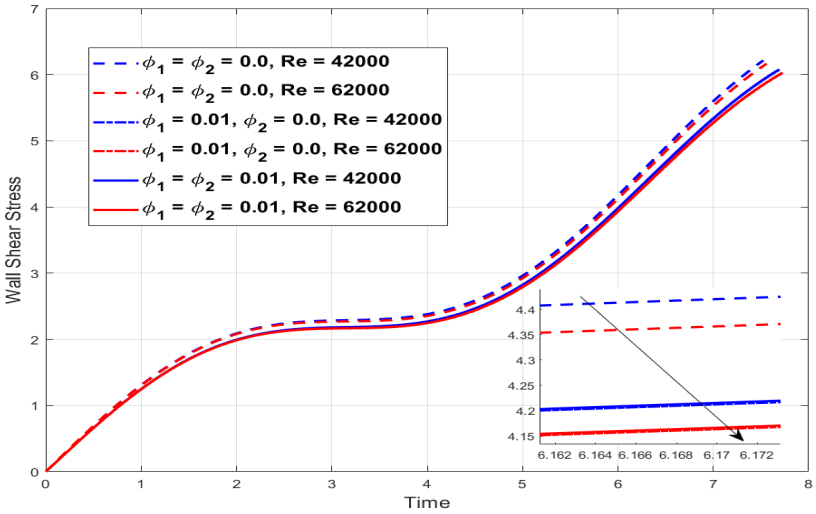

FIGURE 2.8: Turbulent wall shear stress against dimensionless Reynolds number.

The wall shear stress (WSS) variations in a stenotic artery subjected to turbulent

blood flow are illustrated in Figure 2.8. The findings indicate that the WSS decreases as the Reynolds numbers increase, implying that the relative influence of viscous forces (which directly affect WSS) is reduced with faster blood flow (higher inertia). Furthermore, the presence of nanoparticles or hybrid nanofluids in a fluid results in lower WSS than an ordinary fluid. This suggests that the flow dynamics are affected by the presence of particles, perhaps by increasing blood viscosity and damping turbulence-induced stresses.

2.6 Concluding statments

This chapter describes the simulation of unsteady, two-dimensional, non-Newtonian blood flow through a blocked arterial section. The Casson model, which characterizes the relationship between blood viscosity and shear rate, is employed to represent the blood. The study investigates the effects of including copper and alumina nanoparticles with low-volume fractions in the base liquid (blood), as well as the pulsatile nature of the pressure gradient along the radial direction. Additionally, a magnetic field with Hall current is introduced. Axisymmetric boundary conditions for flow through the arterial segment are assumed. To model turbulence flow, the ordinary Navier-Stokes equations (NSE) are converted to Reynolds-averaged Navier-Stokes (RANS) equations, which are then simplified for eddy viscosity using the zero equation turbulence model. The resulting set of dimensionless partial differential equations (PDEs) for fully developed turbulent flow are then numerically solved using the forward time central space differential scheme.
Key Outcomes:

- **Momentum analysis:** The distribution of fluid velocity within the artery, as shown in Figure 2.2, demonstrates how the velocity changes across both the radial and axial directions. The velocity decrease near the arterial walls suggests the presence of a turbulent boundary layer caused by viscous forces.
- **Effects of parameters:** A decline in the mean velocity profile can be observed in Figure 2.3, Figure 2.4 and Figure 2.5 for the variations in Casson model parameter, particle volume fraction and dimensionless Reynolds number, respectively.
- **Wall shear stress:** Reduction in turbulent wall shear plotted against time is observed in Figure 2.6, Figure 2.7 and Figure 2.8 as Casson model parameter, particle volume fractions, and Reynolds number vary.

Chapter 3

Computational Analysis for Momentum Transport

Overview

The accumulation of plaque can cause stenosis, which is a narrowing of the arteries, particularly the left coronary artery. This condition is often associated with coronary artery disease, which results from unhealthy lifestyle choices. If left untreated, stenosis can cause serious complications such as blood clots, strokes, and heart attacks, especially when significant blockages occur in the arteries.
The subject of this discourse is the analysis of computational fluid dynamics (CFD) applied to Newtonian blood flow in a symmetrically stenosed left coronary artery. This analysis employs OpenFOAM, an open-source software package that is specifically designed for CFD projects. In Section 3.2, you can find an overview of the study, which includes the solvers and configurations utilized in the analysis. Section 3.3 outlines the process of developing a detailed 3D model of the arterial lumen, with a 70% stenosis and dimensions of approximately 100 mm in length and 2.9 mm in diameter, using AutoCAD, a commercial software. The following sections provide detailed information on the CFD analysis procedure. In Section 3.4, the process of generating a mesh for the artery model is explained, which involves using the STL file from AutoCAD and employing blockMesh and snappyHexMesh utilities. In Section 3.5, the finite volume method is explained, which is implemented using the icoFoam solver. This method is specially designed to analyze the incompressible, laminar flow of Newtonian fluids. Additionally, the section provides a detailed overview of the required initial and boundary conditions for blood flow analysis. In Section 3.6, the velocity and pressure conditions of the parabolic inlet are elaborated. Various profiles and plots are included in this section to demonstrate the distribution of velocity and pressure. Section 3.7 deals with the simulation of laminar flow by focusing on constant inlet and pressure conditions. This section presents an extensive range of outcomes for velocity and pressure analyses. The final section 3.8 provides a summary of the chapters, highlighting the crucial insights acquired from the computational fluid dynamics analysis of blood flow through a stenosed coronary artery.

3.1 Introduction

Several recent studies have concentrated on the mechanism of blood flow within multiple areas of stenosis. The explanation of arterial blood flow problems is critical in identifying the origin of these stenotic regions, which, in turn, can aid in their treatment. By understanding the blood flow mechanism within stenotic regions, researchers can also pinpoint the cause of the development of arterial stenotic regions. Blood circulation is significantly affected by these arterial stenotic regions, and studying blood flow in these arterial segments provides essential information about the origin and shape of stenotic segments. This information can be used to develop effective treatments for arterial stenotic regions. The use of numerical techniques to solve such issues offers advantages, including the ability to consider complex geometrical models of arterial stenotic segments, as well as the capability to analyze severe stenotic cases without any limitations.
Arterial blood flow was examined by (Haldar, 1985b), who analyzed the different types of stenosis formations and their impact on flow resistance. The study revealed that the greatest flow resistance was found in cases of symmetric stenosis. A mathematical model was created by (Chakravarty and Mandal, 1994a) to address the problem of blood flow in an arterial stenotic region. The blood flow within the carotid artery was studied by (Tang, Yang, and Ku, 1999) using a model that accounted for both symmetric and asymmetric stenotic cases. The numerical interpretation of the non-Newtonian blood flow, which was modeled by Power law fluid, was conducted inside a tapered stenotic region by (Mandal, 2005a).

According to a study conducted by (Elhanafy, Elsaid, and Guaily, 2020a), blood flow characteristics were numerically evaluated in an arterial stenotic section with multiple degrees of stenosis. Additionally, (Yan et al., 2020a) researched the rheology of hemodynamics within an arterial segment with a cone-shaped stenosis. (Tripathi, Vasu, and Bég, 2021) performed a computational analysis on blood flow through a symmetrical arterial stenotic region, while (Moradicheghamahi, Sadeghiseraji, and Jahangiri, 2019) considered numerical solutions of blood flow analysis within a bifurcated arterial stenotic segment.

The modeling of flow behavior in stenosed arteries has become a significant concern within the research community. Computational fluid dynamics (CFD) has emerged as a crucial tool in biomedical and fluid dynamics applications, enabling researchers to model flow behavior in arteries with varying geometries and conditions. CFD has become increasingly utilized in practical applications, ensuring superior product quality and more robust design. Furthermore, CFD has found increasingly extensive applications in the cardiovascular system. CFD is utilized in a wide range of cardiovascular diseases, risk prediction, and virtual treatment planning (Morris et al., 2016). There is a divergence of opinion among scholars regarding the nature of blood flow in coronary arteries. Some researchers posit that the flow is laminar (Doutel et al., 2019; Liu et al., 2015; Chaichana, Sun, and Jewkes, 2013; Gaudio et al., 2018; Carvalho et al., 2020a), and others have studied the flow of blood as a Newtonian fluid (Siogkas et al., 2015; Biglarian et al., 2020; Wu et al., 2015).

3.2 Interoduction to OpenFOAM

`OpenFOAM` is a software package used for Computational Fluid Dynamics (CFD). It is an open-source program with a collection of libraries that can be used to solve various CFD problems. The program uses the finite volume method, where the

computational domain is discretized into small volumes, and the equations to be solved are rewritten to conform to the finite volume approach (Basha et al., 2022b; Chakraborty et al., 2024). OpenFOAM has become increasingly popular among users with diverse scientific and industrial backgrounds. This software offers several features, such as solvers for compressible and incompressible flows, conjugate heat transfer, two-phase flows, laminar flows, and turbulence modeling (RANS, LES, and DNS), among others. Some useful utilities for the CFD workflow, from pre-processing, mesh generation, and mesh format conversion to post-processing of simulation results, are summarized within the context of fluid flow through channel or pipe and are highlighted in Table 3.1. OpenFOAM provides a wide range of solvers with an algorithm to find the solution to a specific set of equations. A table of commonly used solvers available in OpenFOAM for compressible and incompressible flows, along with a short description of their applicability, is presented in Table 3.2.

TABLE 3.1: Description of useful utilities in OpenFOAM

Simulations in OpenFOAM	
Pre-processing	Involves importing geometry, generating mesh and defining boundary conditions.
Mesh Generation	Involves the use of blockMesh and snappyHexMesh.
Post-processing	Involves simulation execution, data extraction, visualization, analysis, and report generation.

3.2.1 OpenFoam case structure

The OpenFOAM simulation setup is linked to the system of equations and domain regions used for modeling the physical system. In conjugate heat transfer problems, fluid and solid regions are considered when configuring the simulation. The case structure and typical configuration for single-phase and incompressible flows are shown in Figure 3.1. There are three main directories named as `0`, `constant` and `system` for every case. In the `0` directory, the initial conditions defined to initiate the simulations and text file in this directory are associated with a particular flow property, e.g., `U` stands for velocity and `p` stands for pressure. The `constant` directory usually contains a subdirectory and a few files. These files contain the material properties that stay unchanged during the simulations. The subdirectory `polyMesh` contains the mesh information, and all the files within the `polyMesh` are generated automatically as the mesh is generated or imported (Direct, 2015). Lastly, in the `system` directory, simulation can be defined or controlled by editing three of the text files, `fvSchemes`, `fvSolution` and `controlDict` containing discretization scheme, setting for the coupling methods for the velocity and pressure. `controlDict` file contains the controlling parameters for simulation stability like starting time of simulation (`startFrom`), finishing time (`stopAt`), time step (`deltaT`) and data saving interval (`writeInterval`), etc.

TABLE 3.2: Accessible solvers in OpenFOAM

Incompressible Flow Solvers	
simpleFoam	Solver for steady-state, incompressible flow that uses the SIMPLE algorithm.
pisoFoam	Transient, incompressible flow solver based on the PISO algorithm.
icoFoam	Solver that calculates transient and incompressible flow using the PISO algorithm.
pimpleFoam	Solver that deals with incompressible flows that are temporary in nature. It uses the SIMPLE algorithm and has a co-located grid.
interFoam	Solver is needed for incompressible two-phase flow which employs a Volume of Fluid (VoF) approach to capture the interface.
Compressible Flow Solvers	
rhoCentralFoam	Transient solver for compressible flow using central differencing scheme.
rhoPimpleFoam	Transient solver for compressible flow using PISO algorithm.
rhoSimpleFoam	Steady-state solver for compressible flow using the SIMPLE algorithm.

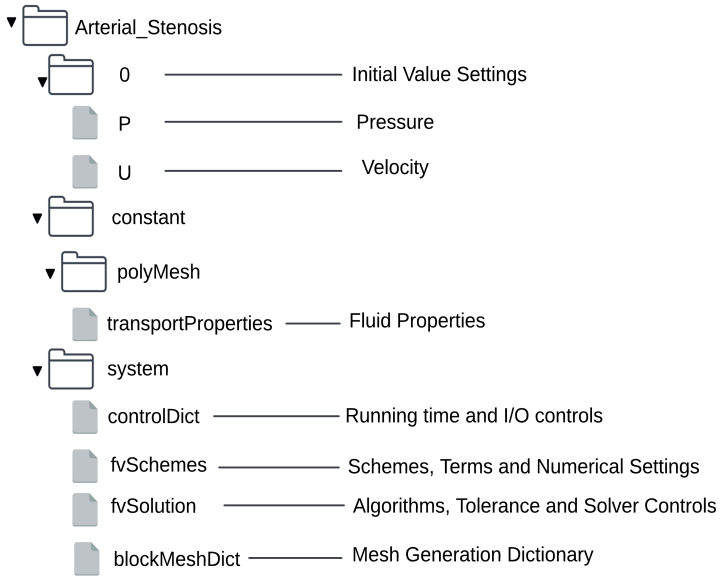

FIGURE 3.1: OpenFOAM's Basic Case Structure Hierarchy

3.3 3D geometry extraction

In order to examine the flow of blood, it is necessary to obtain the three-dimensional shape of the inside of the coronary artery. To do this, a model of a stenosed (narrowed) coronary artery was created for use in computational fluid dynamics simulations. The artery was designed to be a cylindrical tube with a total length of 100mm and a diameter of 2.9mm, which is similar to the size of an average human coronary artery (Zhou, 2017). To simulate a pathological condition, a narrowed region was introduced into the lumen with a 70% reduction in its cross-sectional area. This reduction was added symmetrically in the axial direction, making it anatomically accurate. According to (Rabby, Razzak, and Molla, 2017; Buradi and Mahalingam, 2018; Mahalingam et al., 2016), the length of the stenosis is defined as twice the normal diameter. Additionally, the entrance length was chosen to establish velocity profiles fully proximal to the stenosis. The geometry was constructed using AutoCAD software, which enabled precise control over the dimensions and allowed for a high degree of customization of the artery model. The generated model was then converted into *.STL* format, which is compatible with OpenFOAM for mesh generation and subsequent flow simulation. The stenosis model developed and its geometric parameters are represented in Figures 3.2 and 3.3.

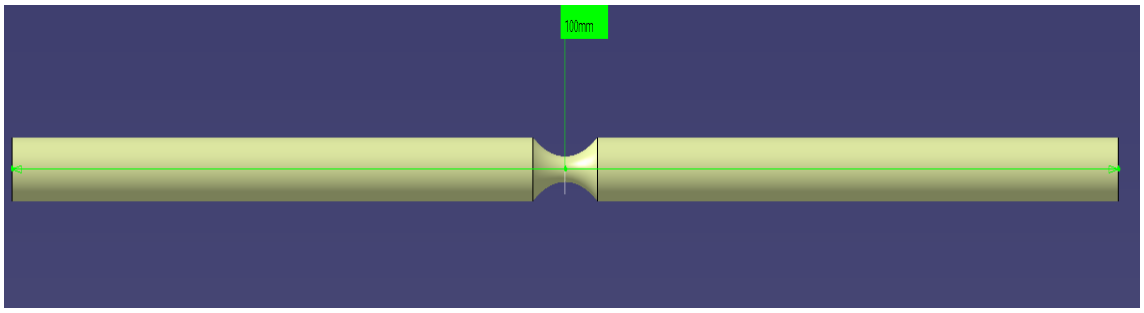

FIGURE 3.2: Longitudinal section view of a 3D model of a stenotic artery, designed in AutoCAD with a total length of 100mm.

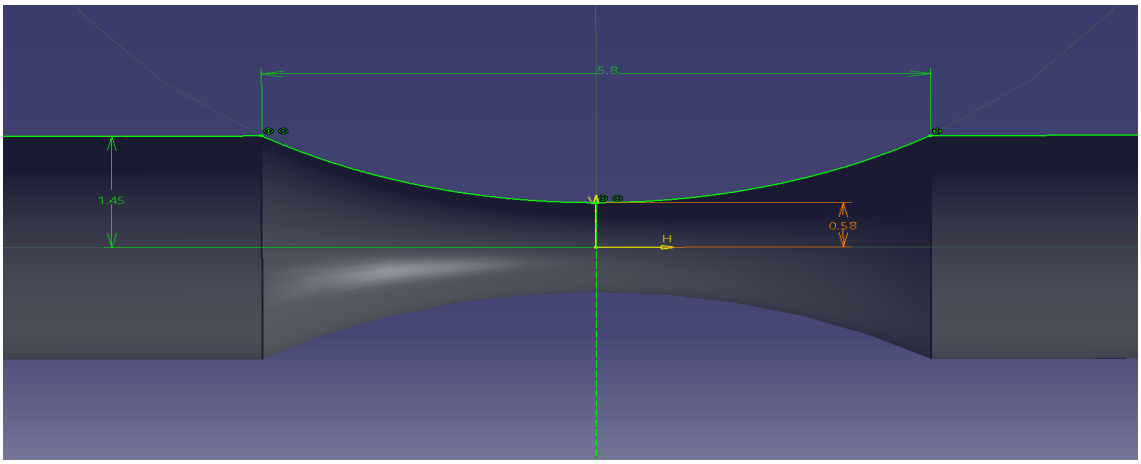

FIGURE 3.3: STL file for 3D stenotic artery model, with an artery diameter of 2.9mm, showcasing a 70% stenosis narrowing.

3.4 Computational mesh generation

The computational volume mesh is created using OpenFOAM utilities, in particular, `blockMesh` and `snappyHexMesh` as a part of pre-processing. First of all, through the `blockMesh` utility, a simple background mesh is created by defining a single hexahedral block that spans the entire domain of STL file produced by AutoCAD software (Figure 3.2, 3.3) using the cell counts provided by the $\$xCells$, $\$yCells$, and $\$zCells$.

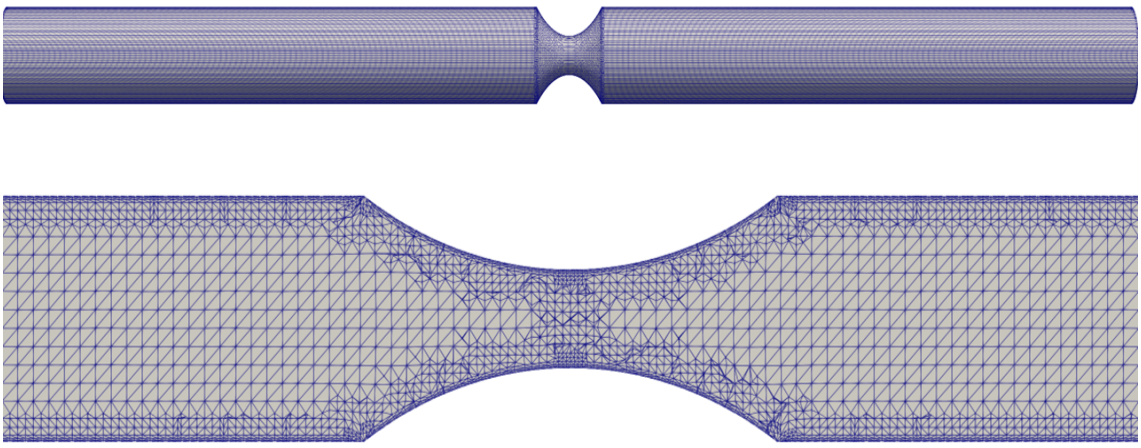

FIGURE 3.4: Based on `snappyHexMesh`, a stenotic artery simulation shows localized refinement at the constriction.

The quality and quantity of cells obtained after the meshing procedure depend on the construction of the background mesh, which is actually important despite being very simple. The overall domain was defined by the bounding box with coordinates ranging from (-35, -1.01, -1.01) to (35, 1.01, 1.01). `snappyHexMesh` is a utility that generates the three-dimensional mesh and approximates the STL surface according to parameters specified in the related dictionary. It takes a background mesh from `blockMesh` and refines it near the surfaces where higher resolution is needed. The process consists of three phases.
The initial phase involves creating a castellated mesh to generate an initial grid made up of hexahedral cells only. The second phase is referred to as the "snap" stage. The final phase is the "add layer" phase, during which additional cells are introduced near the walls. In Figure 3.4, `snappyHexMesh` is utilized to capture the complex geometry of the stenosis, automatically refining the mesh where the geometry dictates and ensuring that there is a smooth transition from coarser to finer grids. The cylindrical body of the mesh has uniform hexahedral cells, which are efficient for solving fluid flow equations, while the stenosis is resolved with increased mesh density to accurately simulate the intricate flow details in that region.
From Figure 3.5a, the structured grid distribution is clearly visible, showcasing the finer mesh resolution at the stenotic region, which is crucial for accurately capturing the complex flow patterns and gradients expected in such narrowed passages. A cross-sectional view of the arterial mesh as generated by `snappyHexMesh`, before the incorporation of boundary layers can be seen in Figure 3.5b. This base mesh, composed of hexahedral elements, represents the initial step in creating a computational model that can be refined to simulate blood flow. The uniform grid structure across the diameter sets the stage for subsequent mesh refinement, where additional layers will be introduced to capture the boundary layer physics more accurately. A refined cross-sectional view of the mesh at the location of the artery's stenosis is characterized by Figure 3.5c. Boundary layers have been added to the mesh, allowing for a more precise simulation of the flow near the artery wall where velocity gradients are most pronounced. The simulation accurately reflects flow dynamics within the boundary layer to capture essential physics driving disease progression in stenotic arteries. Table 3.3 summarizes some information about the quality of the mesh obtained.

TABLE 3.3: Mesh quality parameters

Number of nodes	449412
Number of faces	1234882
Number of cells	393733
Maximum aspect ratio	7.40688
Maximum non-orthogonality	61.3063
Average non-orthogonality	8.79933
Maximum skewness	1.80883

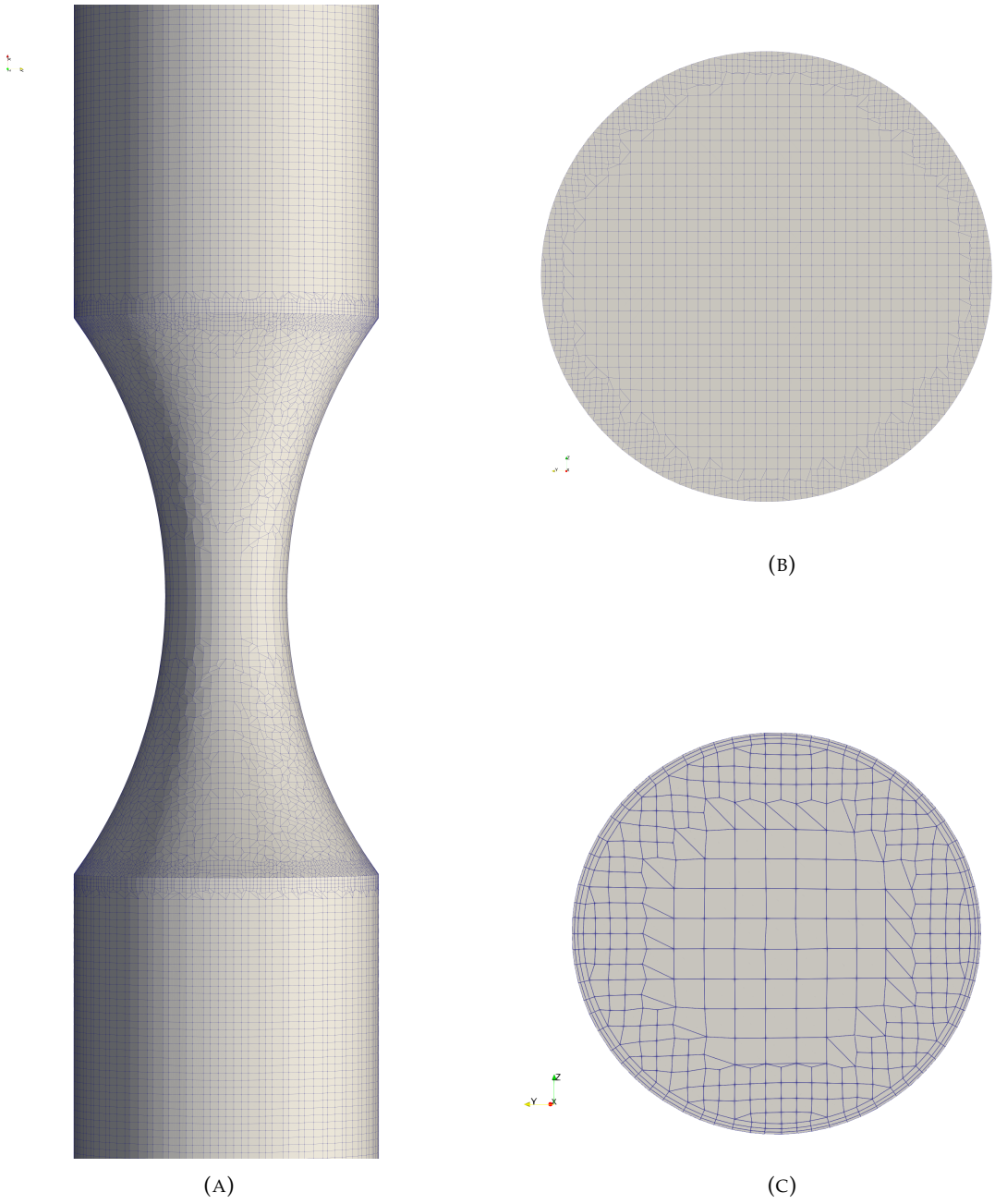

(A) (B) (C)

FIGURE 3.5: **(A)** Meshed geometry of a 70% stenosed artery section showing the structured grid distribution through the narrowed lumen. **(B)** Cross-sectional view of the arterial mesh using `snappyHexMesh` without boundary layers, highlighting the base hexahedral mesh structure across the arterial diameter. **C** Refined mesh in a cross-section of the stenotic artery with boundary layers added to capture the velocity gradient near the wall.

3.5 The finite volume (FV) method

The `icoFoam` solver is a computational tool that is specifically designed to handle the incompressible and laminar regime of flow. This means that the effects of turbulence are not taken into account in the model. This approach is suitable for flows where the Reynolds number is low enough that the flow is smooth and steady, with no

eddies or swirls that characterize turbulent flow. Compared to turbulent models, the laminar flow model is less computationally intensive since it does not require the resolution of the turbulent scales or the use of turbulence closure models. In mathematical terms, NSE is represented as:

$$\nabla \cdot V = 0, \tag{3.1}$$

$$\frac{\partial V}{\partial t} + (V \cdot \nabla)V = -\frac{1}{\rho}\nabla P + \nu \nabla^2 V \tag{3.2}$$

where,t is time, V is the velocity vector, P is the fluids pressure, ρ is the fluid density and ν is the kinematic viscosity. The term $(V \cdot \nabla)V$ represents the convective acceleration (nonlinear term), and $\nu \nabla^2 V$ is the viscous diffusion term. In `icoFoam`, the pressure-velocity coupling is typically handled using the SIMPLE algorithm or its variants, which iteratively solve the momentum and pressure equations to ensure mass conservation is satisfied while reaching a converged solution for both the velocity and pressure fields.
`icoFoam` in OpenFOAM uses the Finite Volume (FV) method [6] allowing the integration of a set of partial differential equations in a volume domain. On the boundaries of this domain, different boundary conditions are applied. To perform this integration, the domain volume is divided into smaller elemental volumes. Each of these volumes surrounds a discrete node point on the mesh. The required fields and values are calculated at each node point. With the FV method, every volume integral that appears in the partial differential equations is transformed into a surface integral via Gauss theorem. The transformed integral is evaluated as a flux at the surfaces of every finite volume. As the name suggests, the sub-volumes are finite and not infinitesimal. The FV method itself was originally developed as a special version of the Finite Difference approach. This approach describes the unknowns of the flow problem via samples at the node points of a grid of coordinate lines.

3.5.1 Courant-Friedrichs-Lewy (CFL) condition

The stability of numerical solutions to partial differential equations solved using explicit time-marching methods depends on the Courant-Friedrichs-Lewy (CFL) condition, which is a crucial criterion for convergence. In computational fluid dynamics (CFD), this condition is often referred to as the Courant number, and it is especially important when solving the equations for fluid flow simulations.
In the `icoFoam` solver within OpenFOAM, the CFL condition demands that the time step size be small enough to prevent numerical errors from amplifying during simulation. In particular, the CFL condition necessitates that the time step (Δt) is below a certain threshold to ensure that fluid particles do not travel more than one computational cell per time step. In a one-dimensional scenario, with u as fluid velocity and Δx as the spatial discretization step the CFL condition can be defined as:

$$CFL = u\frac{\Delta t}{\Delta x} \leq 1$$

The CFL condition is not a strict stability criterion for the `icoFoam` solver, which is intended for incompressible flow because the solver is implicit. Nonetheless, it is advisable to keep a low CFL number as a good practice to ensure that the computational domain accurately captures the physical diffusion and convection processes.

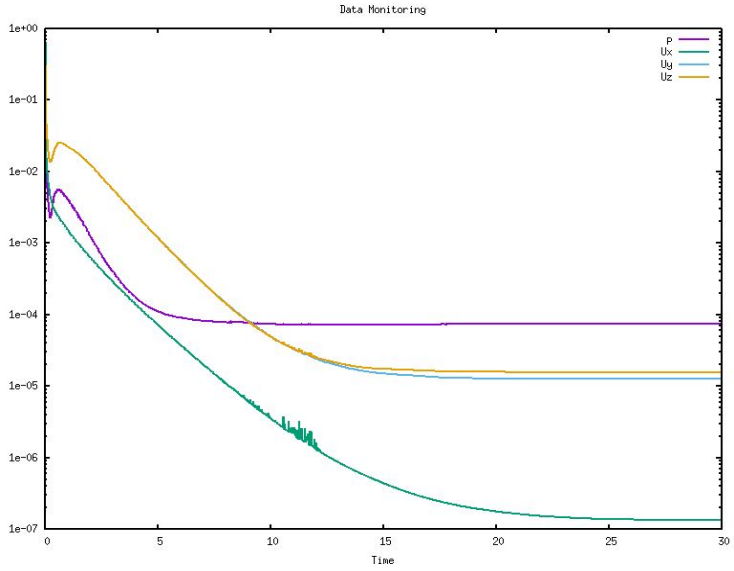

FIGURE 3.6: Residual error for Newtonian blood flow with parabolic inlet velocity through a stenotic arterial section.

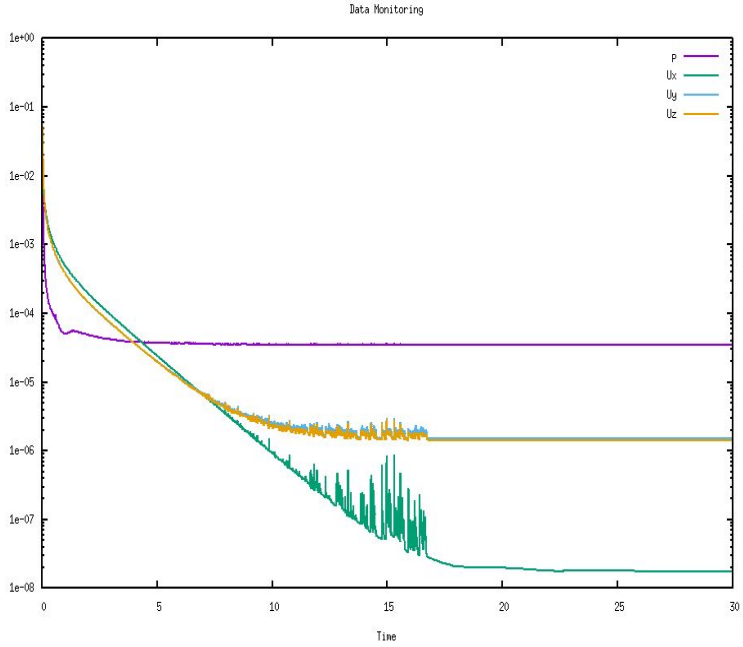

FIGURE 3.7: Residual error for Newtonian blood flow with constant inlet velocity through a stenotic arterial section.

The graphs in Figure 3.6 and 3.7 illustrate the residual errors for pressure (p) and velocity components (U_x, U_y, U_z) over a 30-second simulation of Newtonian blood flow with a parabolic and constant inlet velocity through a stenotic arterial section. The residuals, plotted on a logarithmic scale on the y-axis, indicate the convergence of the simulation over time, shown on the x-axis. Initially, the residuals are high, reflecting the initial transient conditions. Over time, the residuals for the velocity components (U_x, U_y, U_z) drops significantly faster than the pressure residual (p). The velocity components' residuals fluctuate around $1e^{-06}$ before stabilizing, indicating that the velocity field is converging. In contrast, the pressure residual (p)

decreases more slowly and stabilizes at a higher magnitude of around $1e^{-04}$. Consequently, the numerical stability and accuracy of the simulation are ensured by the gradual decrease and eventual stabilization of residuals.

3.6 Parabolic inlet condition

A parabolic inlet velocity profile was used in the numerical simulation of blood flow through a stenotic artery with a 70% constriction. The `codedFixedValue` was prescribed for this purpose. The simulation was based on the principles of Newtonian physics. boundary condition in OpenFOAM. This condition was defined within the `icoFoam` solver framework to emulate the fully developed, laminar flow entering the artery. The profile was centered around the point $(0.045, 0.195)$ in the cross-sectional plane, with a radius $R = 0.015m$. The maximum inlet velocity U_b was set to $0.003m/s$. The radial position r for any point within the inlet face was calculated as the Euclidean distance from the profile's center in the cross-sectional plane, and the axial velocity component was determined by the expression (Figure 3.8)

$$U_z = -2U_b \left(1 - \left(\frac{r}{R}\right)^2\right)$$

This velocity profile ensures a gradual reduction to zero velocity at the walls due to the no-slip boundary condition. The outlet boundary condition is specified as `zeroGradient`, which means the flow is allowed to develop and exit the simulation domain without any additional constraints on the velocity gradient at the outlet. The `noSlip` condition at the wall ensures that the velocity is zero at the artery wall, adhering to the physical behavior of viscous fluids. This approach provided a realistic representation of the blood's velocity distribution as it entered the region of interest, capturing the essential hemodynamic features for the simulation of flow through a stenotic artery.
For incompressible flow simulations, a common method for solid boundaries is to utilize a pressure boundary condition of `zeroGradient` at the inlet. This assumption implies that the normal gradient of pressure at the inlet boundary is negligible, which is frequently the case for fully developed inlet flow. On the outlet, a `fixedValue` condition is set, with a uniform value of 0. This value is a reference pressure level, which is usually taken as atmospheric pressure for internal flows or as an arbitrary datum in incompressible flow simulations since only pressure differences drive the flow. Lastly, a `zeroGradient` pressure condition is also applied at the walls, indicating that the simulation assumes no significant pressure change normal to the walls.

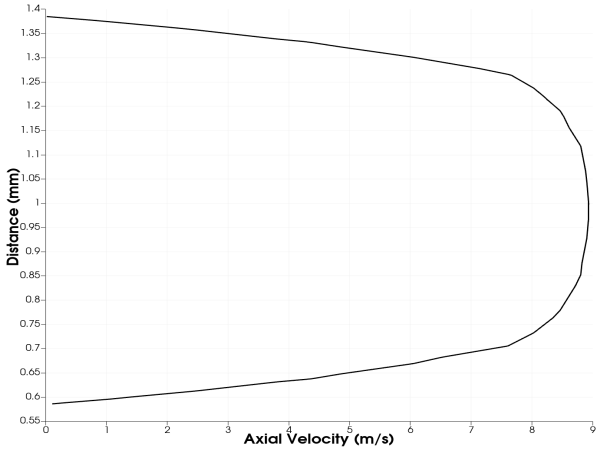

FIGURE 3.8: Simulated Axial Velocity Profile (U_x) at Stenosis in a Newtonian Blood Flow with Parabolic Inlet Conditions.

3.6.1 Parabolic inlet velocity flow analysis

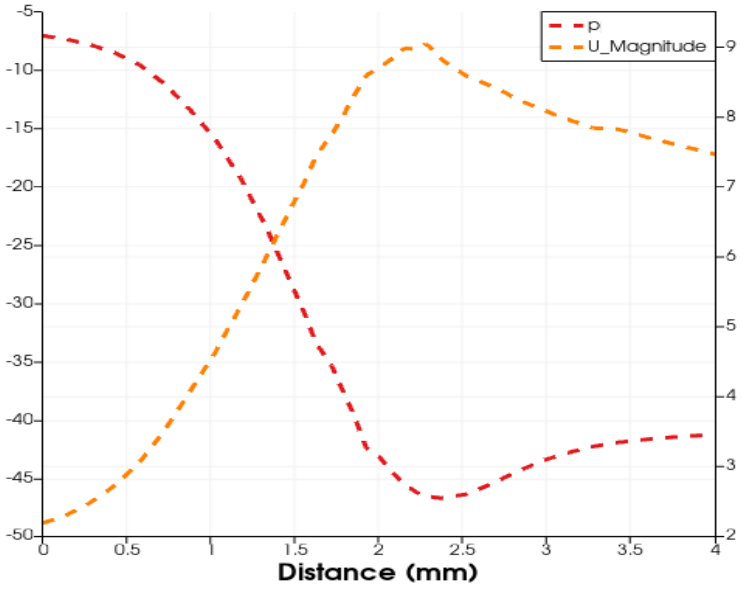

FIGURE 3.9: Simulated velocity magnitude $(U_{magnitude})$ at stenosis in a Newtonian blood flow with parabolic inlet conditions.

The plot in Figure 3.9 shows the velocity and pressure profiles of Newtonian blood flow at the stenosis in an arterial section under conditions of laminar flow with a parabolic inlet velocity profile. The dashed orange line signifies the axial velocity's magnitude $(U_{Magnitude})$. It reaches its highest point where the stenosis restricts the flow and decreases proportionally towards the edges, forming a parabolic profile. The velocity distribution is established by the inlet condition, which is designed to imitate the physiological velocity distribution in a vessel. In this distribution, the maximum velocity is situated at the center and gradually diminishes towards the arterial wall, following a quadratic function. Along the same section, the pressure (p) is indicated by the dotted red line. The stenosis causes a clear drop in pressure, which can be understood by the fluid dynamics principle that explains how velocity

increases as the cross-sectional area decreases, resulting in a corresponding reduction in pressure.

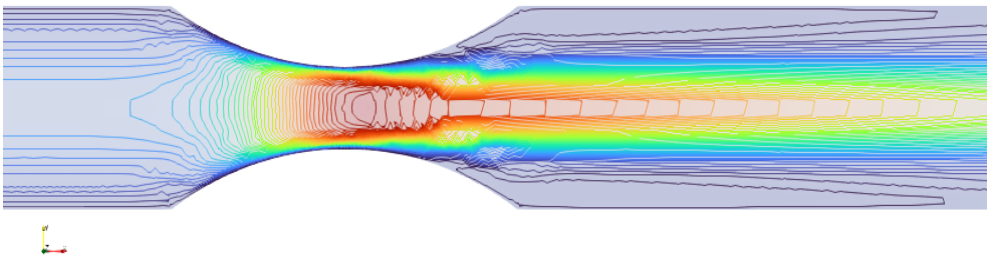

FIGURE 3.10: Velocity contours of Newtonian blood flow through a stenotic artery.

Figure 3.10 showcases the velocity contours for Newtonian blood flow distribution from the pre-stenotic region, through the stenosis, and into the post-stenotic region. The velocity magnitude is represented by the color gradient in the contours. Red stands for areas of higher velocity while blue represents regions of slower flow. The flow starts to accelerate just upstream of the stenosis and converges towards the center of the artery as it approaches the stenotic region. The highest velocities are observed at the stenotic region as the blood flow must speed up to maintain the flow rate through the narrower lumen. Following the stenosis, there is a noticeable separation of flow that can be seen through a change in contour lines. This separation is highlighted by the recirculation zone that forms. The deceleration of flow in this area is evident by the spread of lower-velocity blue contours. As the flow reattaches and stabilizes downstream, it returns to a more organized pattern, and the velocity gradually increases again.

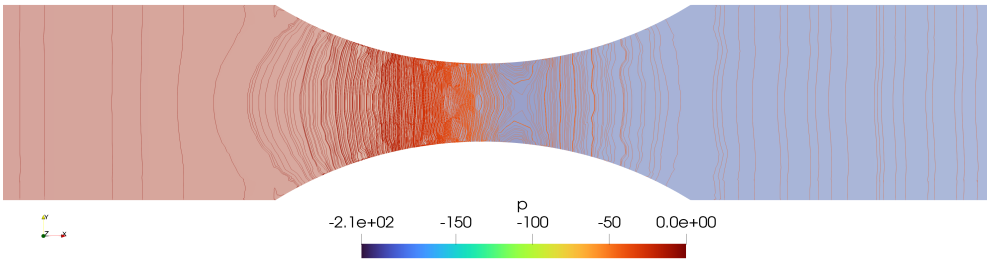

FIGURE 3.11: Pressure contours of Newtonian blood flow through a stenotic artery.

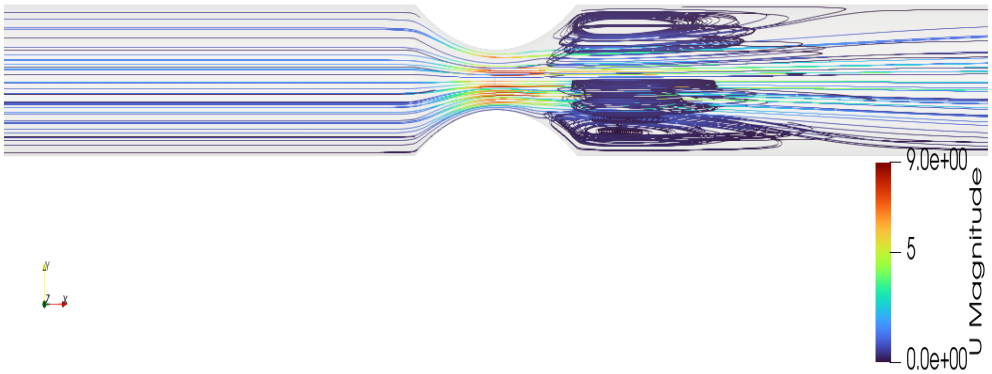

FIGURE 3.12: Streamline visualization depicting velocity magnitudes and flow patterns through the constriction.

Figure 3.11 shows the gradient in pressure distribution along the artery. The uniform color banding observed within the arterial segment preceding the stenosis indicates a constant pressure, which is maintained due to the `zeroGradient` condition at the inlet. This observation suggests the flow entering the stenotic section lacks any initial pressure variation across the cross-section. When blood enters a stenotic constriction, pressure contours begin to compress. By reducing the cross-sectional area caused by the stenosis, flow acceleration results in a lower pressure at the narrowest point, consistent with Bernoulli's principle. At the stenosis, red contours indicate the lowest pressure regions. Pressure contours beyond the stenosis diverge, indicating recovery due to the widened cross-sectional area. The `fixedValue` condition at the outlet maintains constant pressure, influencing the pressure recovery downstream. Streamline visualization in Figure 3.12 shows how blood speed changes in laminar flow as it passes through different diameters of an artery. In the regions far from the stenosis, the streamlines are straight, parallel, and uniformly blue, indicating a steady, low-velocity flow with minimal mixing or disturbance. As the blood approaches the stenotic region, the streamlines begin to converge, signaling an increase in velocity as the artery narrows. The color transition from blue to green and then to yellow reflects this acceleration. At the narrowest point, or the throat of the stenosis, the streamlines are tightly packed and shift towards orange and red hues, marking the highest velocities within the constriction. After a constriction, blood flow decelerates and creates complex flow patterns. Swirling patterns and looped streamlines indicate the emergence of recirculation zones, which are often associated with areas of low wall shear stress. The flow downstream realigns and elongates, suggesting a return to steady flow. Colors shift back to blue, indicating a decrease in velocity.

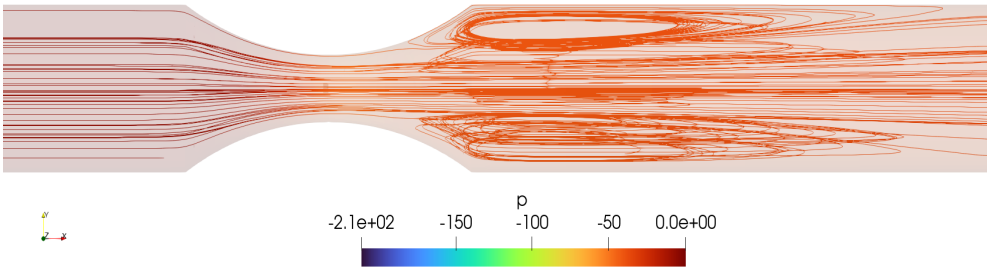

FIGURE 3.13: Streamline visualization depicting pressure magnitudes and flow patterns through the constriction.

Figure 3.13 visualizes the spatial distribution and magnitude of pressure along a stenotic artery's flow path. The pressure streamlines are evenly spaced and exhibit a calm gradient, indicative of a steady pressure distribution in the laminar flow regime. As the flow reaches the stenotic region, the streamlines converge, demonstrating a significant pressure drop across the stenosis. This convergence is closely associated with the flow acceleration due to the decreased cross-sectional area. At the stenosis site, pressure streamlines diverge, indicating pressure recovery as flow decelerates. Despite overall laminar flow, complex patterns and swirls suggest turbulent-like behavior due to rapid changes in flow conditions causing localized instabilities or recirculation zones.

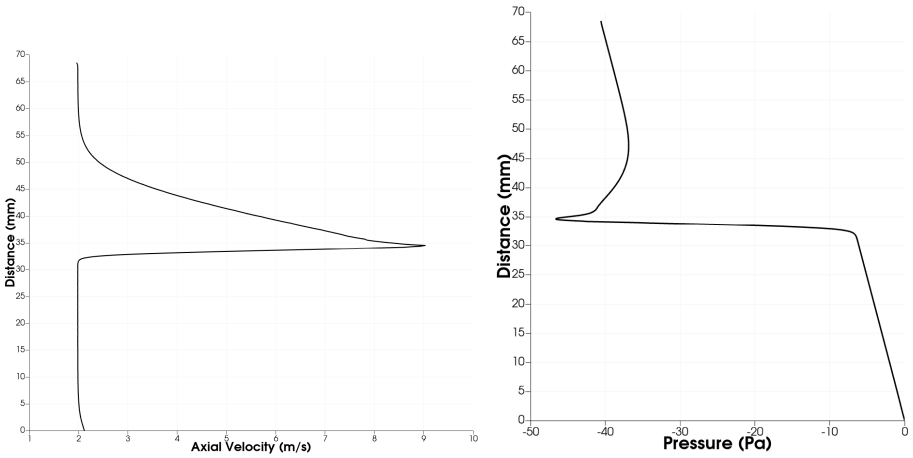

(A) (B)

FIGURE 3.14: Axial velocity profile (U_x) and pressure of Newtonian blood flow in a stenotic artery with parabolic inlet conditions.

Figure 3.14a presents the distribution of axial velocity U_x plotted against the distance from the beginning of the artery, covering both the pre-stenotic and post-stenotic regions. In the pre-stenotic section $(0mm - 31mm)$, the axial velocity remains relatively low and constant. This suggests a stable and undisturbed flow before encountering the narrowing of the artery. As the blood approaches the stenotic region, there is a significant increase in velocity. This sharp rise is attributed to the conservation of mass, requiring the flow rate to increase to compensate for the reduced cross-sectional area at the constriction. The peak in the graph corresponds to the narrowest point of the stenosis. Beyond the stenosis, the axial velocity abruptly

decreases, illustrating the post-stenotic deceleration of the flow. This deceleration is a consequence of the blood entering a wider portion of the artery after the stenotic region, allowing it to spread out and slow down. The extended high-velocity tail beyond the stenosis suggests the persistence of disturbed flow patterns, which may include separation and the potential formation of vortices or recirculation zones.
The distribution of pressure along the axial distance of an artery is displayed in Figure 3.14b, indicating pressure variation from the pre-stenotic region through the stenosis and into the post-stenotic area. Initially, the pressure stays relatively stable, corresponding to the unobstructed part of the artery where the blood flow hasn't yet reached the stenosis. When the flow approaches the stenosis, there's a sudden drop in pressure, marked by the steep decline in the graph. This decline indicates the increased resistance the blood encounters as the artery narrows. It's a phenomenon known as the pressure gradient, which is necessary to push the flow through the reduced diameter. As fluid enters the narrow area, the pressure keeps decreasing until it reaches its lowest point at the narrowest spot. This phenomenon is known as the Venturi effect, which results in the acceleration of the fluid velocity at the constriction, leading to a drop in pressure. After the stenosis, there's a slight pressure rise, marking the beginning of a wider artery and slower flow.

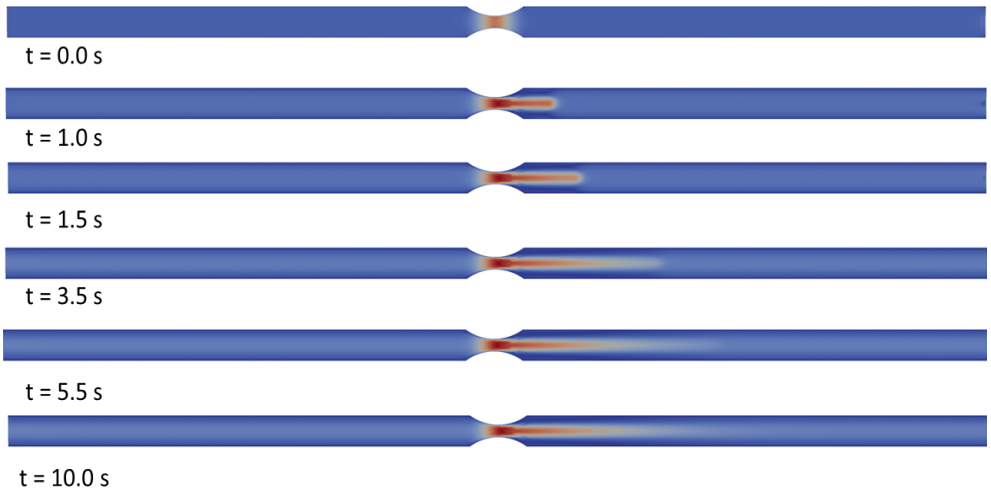

FIGURE 3.15: Temporal evolution of axial velocity for parabolic inlet velocity.

Figure 3.15 shows a sequence of time-lapse visualizations that demonstrate the axial velocity of Newtonian blood flow passing through an elliptically shaped stenotic artery. The time steps in each visualization capture the transient nature of blood flow as it responds to arterial stenosis. The dynamics of the flow become intricate due to the narrowing, and this can be seen in the visualizations.
At t=0.0s, the initial condition reflects the imposed parabolic velocity profile, with no disturbances yet from the stenotic region. The flow is uniform and undisturbed, representing the baseline state before interacting with the stenosis. By t=1.0s, the blood has begun to interact with the stenotic region, as indicated by slight perturbations in the flow pattern. The velocity in the vicinity of the stenosis starts to increase, conforming to the narrowing geometry of the artery. Due to the constricted lumen, the flow acceleration becomes more pronounced at t=1.5s. As expected, the

highest velocities occur at the throat of the stenosis, in accordance with the conservation of mass. After 3.5 seconds, an established post-stenotic flow pattern manifests. Downstream of the stenosis, distinct separation zones can be observed, characterized by a complex pattern of recirculating flow. These zones can be easily identified by changes in contour lines and the emergence of lower velocities, depicted by cooler colors, near the high-velocity streaks. The evolution of the flow persists and recirculation is observed at t=5.5s. It seems from Figure 3.15 that at t=10.0s, the flow has entered into a state of quasi-steadiness, with the patterns of post-stenotic disturbances appearing to be consistent with those observed at t=5.5s.

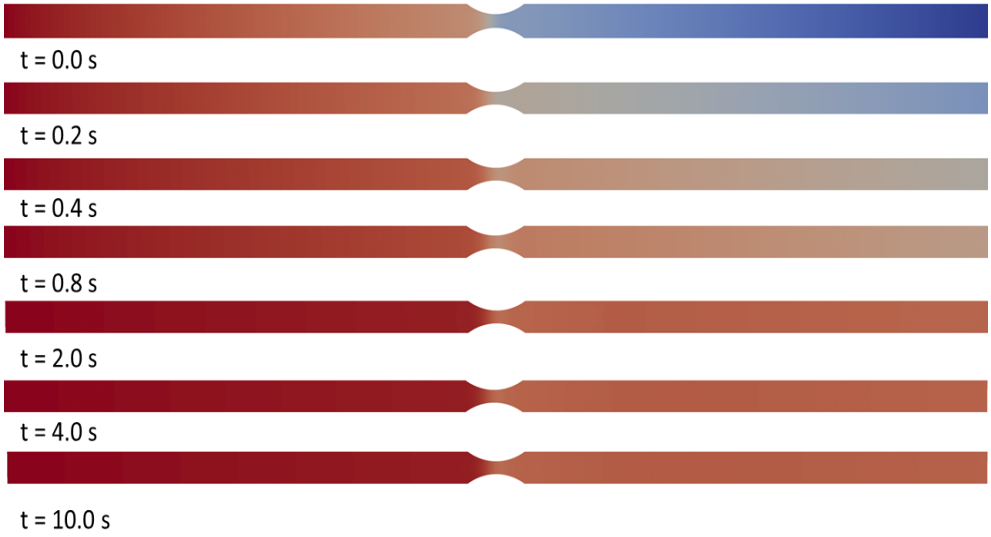

FIGURE 3.16: Temporal evolution of pressure for parabolic inlet velocity.

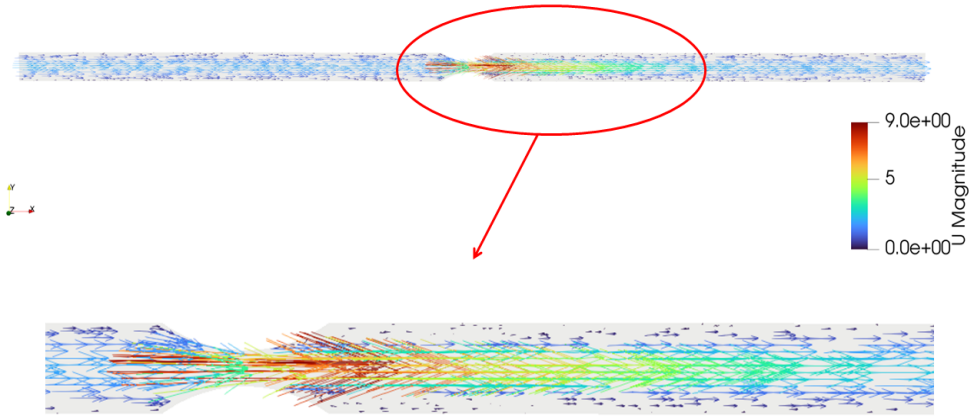

FIGURE 3.17: Axial velocity vectors through an artery with stenosis, displaying flow acceleration and post-stenotic disturbances.

In Figure 3.16, the pressure field evolution for laminar blood flow with parabolic inlet velocity can be noticed. The pressure across the artery is uniform and at a baseline level at $t = 0.0s$. This is indicated by the uniform internal field set to 0. As time progresses to $t = 0.2s$ and $t = 0.4s$, we start to see the effects of the flow beginning from the inlet. A high-pressure region is expected at the inlet due to the `zeroGradient` boundary condition. By $t = 0.8s$, the pressure has started to develop along the length of the artery. Higher pressures upstream are represented by darker colors, and there is a gradient towards the outlet where the pressure is fixed at 0 (lighter colors). At $t = 2.0s$, the pressure distribution becomes more pronounced. There is a clear gradient from high pressure at the inlet to lower pressure at the outlet as a result of the flow resistance. Moving to $t = 4.0s$, the pressure field shows further development. There is also the formation of a distinct pressure drop across the stenosis. Finally, by $t = 10.0s$, the pressure field appears to reach a quasi-steady state. The highest pressures are at the inlet and there is a smooth gradient to the outlet. The stenotic region continues to exhibit a localized low-pressure zone due to the accelerated flow speeds in the constriction.
The sequence of velocity vector plots in Figure 3.17 displays the behavior of Newtonian blood flow in a stenotic artery. The vectors show the velocity at different points in the artery and are colored by magnitude to depict the flow's dynamism. In the unblocked area before the stenosis, the flow is steady and consistent, indicating low inertial forces and a low Reynolds number. As the flow passes through the stenosis, the velocity vectors change significantly. The vectors extend and vary in color, indicating an increase in velocity due to the reduced cross-sectional area. The range of colors reveals the variation in velocity, with the highest speeds occurring at the throat of the constriction. Significant changes in the flow are observed within and immediately downstream of the stenosis. This phenomenon is characterized by divergent vectors, which demonstrate the potential for flow separation and the formation of vortices - common occurrences in stenotic flows.

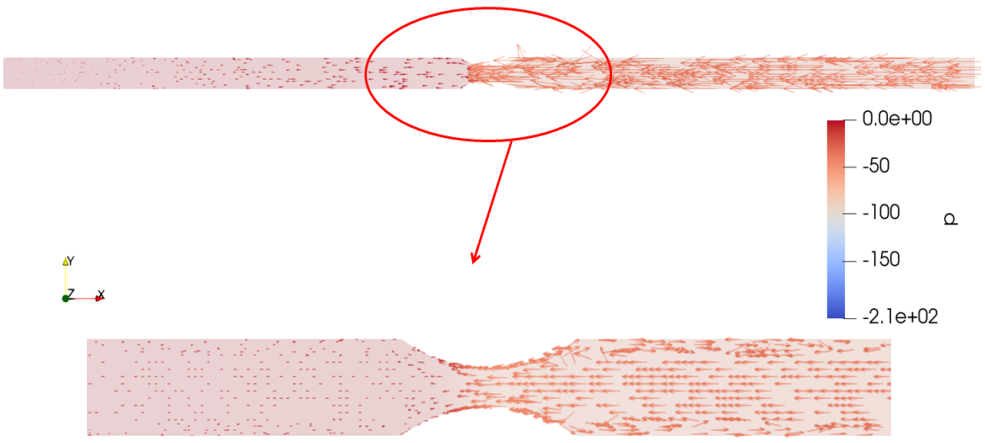

FIGURE 3.18: Pressure vectors through an artery with a stenosis, displaying flow acceleration and post-stenotic disturbances.

The figure labeled as 3.18 presents the pressure distribution and vectors along an arterial segment simulated for laminar Newtonian blood. The pressure field is

initially set to zero, and the `zeroGradient` condition at the inlet allows the pressure to develop naturally from the flow conditions. As the artery narrows at the stenosis point, the pressure vectors become more concentrated and pronounced, indicating an increase in the pressure gradient due to the flow path restriction. Once the vessel widens downstream of the stenosis point, the pressure vectors spread out more evenly again as the flow decelerates.

3.7 Constant inlet condition

The initial and boundary conditions for the velocity field of the simulation are set by the `U` file in the `0` directory. For the analysis of Newtonian blood flow with viscosity $\nu = 10^{-6} m^2/s$ and $Re \approx 200$, the inlet boundary is set to a `fixedValue` type with a uniform velocity defined by the `Uinlet` variable, which is specified as $0.0137 m/s$. This ensures that the fluid enters the simulation domain with a steady velocity in the axial direction of the artery and with no components in the transverse directions, resulting in a fully developed flow profile at the inlet. The `noSlip` condition on the wall ensures that the velocity of the fluid at the boundary is zero, realistically representing the viscous behavior of fluids adhering to solid surfaces. The outlet is defined with a `zeroGradient` condition, meaning that the gradient of the velocity at the outlet is assumed to be zero. It is frequently assumed when the outlet pressure or velocity profile is not known precisely or when the flow has stabilized sufficiently downstream from any disturbances.
To simulate pressure-driven blood flow, the `internalField` is set to zero. This creates a uniform pressure gradient throughout the flow field, a common starting condition for incompressible flow simulations. The pressure differences that propel the flow are more important than the absolute pressure level. Therefore, to replicate pressure-driven blood movement, the `internalField` is initialized to zero. This uniform value signifies that the simulation starts with a zero pressure gradient throughout the entire flow field, a commonly used starting condition for incompressible flow simulations. In such simulations, the absolute pressure level is less significant than the pressure differences that drive the flow. The `zeroGradient` type specifies that there is no change in pressure across the boundary at the flow entry point or inlet. A `fixedValue` type with a `uniform 0` value is considered as an outlet pressure condition maintaining a constant pressure value at the outlet. The `zeroGradient` classification for the wall indicates that there is no pressure gradient that is perpendicular to the walls of the artery. This is in line with a no-flux condition, where the wall does not allow the flow of fluid, thereby preventing pressure from varying in a direction that is perpendicular to the wall.

3.7.1 Constant inlet velocity flow analysis

The velocity magnitude and pressure profiles for Newtonian blood flow at the point of stenosis in a stenotic artery under laminar flow conditions are depicted in Figure 3.19. The velocity profile $(U_{Magnitude})$ is represented by the dashed orange line, while the dotted red line illustrates the pressure (p) within the artery. The velocity distribution within the stenotic region of the artery exhibits a parabolic profile with a pronounced peak at the center. This is indicative of the highest velocity occurring at the site of the smallest cross-sectional area of the arterial lumen. As blood travels through the narrowed section of an artery, it speeds up to maintain a consistent flow rate. The velocity of the blood gradually decreases as it moves further away from the

centerline. The lowest pressure is found at the center of the stenosis where the velocity is the highest, as indicated by the pressure profile. Bernoulli's principle describes the inverse relationship between pressure and velocity in a constricted region.

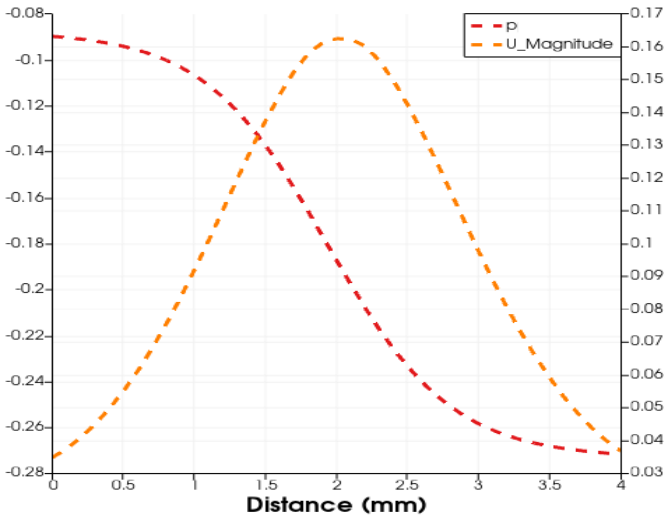

FIGURE 3.19: Simulated velocity magnitude and pressure at stenosis in a Newtonian blood flow with constant inlet conditions.

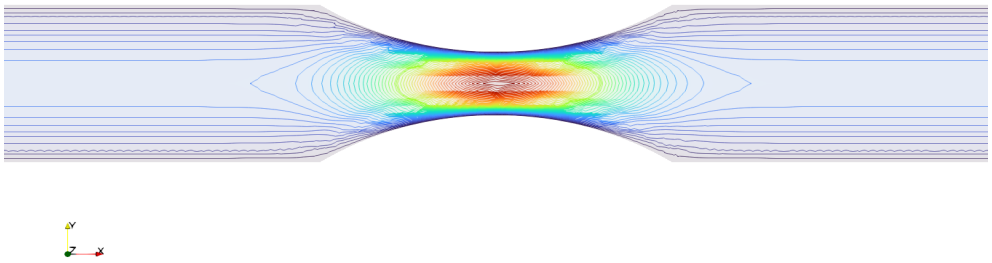

FIGURE 3.20: Velocity contours of Newtonian blood flow through a stenotic artery.

The graph shown in Figure 3.20 provides a clear visualization of laminar Newtonian blood flow through a narrowed section of an artery. The colors in the graph correspond to different velocities, with red and orange indicating higher velocities and blue indicating lower velocities. The central region of the stenosis displays the highest velocity due to the conservation of mass, with a gradual increase in velocity towards the narrowed region. After passing through the stenosis, the flow decelerates, as evidenced by the shift towards blue hues. This pattern shows the altered hemodynamics caused by the stenosis, with the highest velocity magnitudes present at the throat of the constriction. Overall, the graph offers an informative and detailed visualization of the flow acceleration and deceleration associated with stenotic geometry.

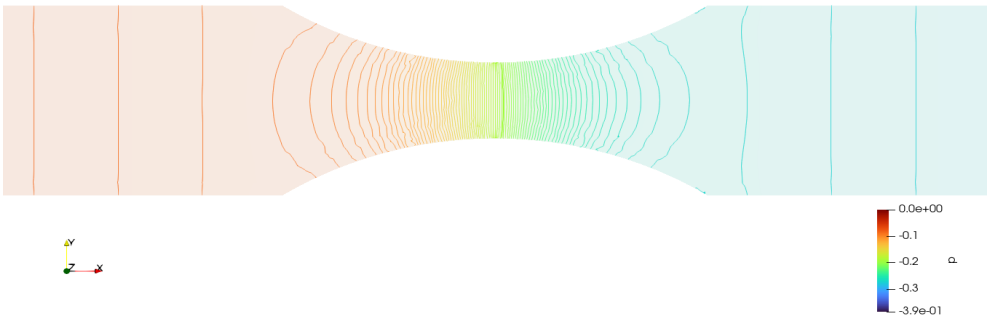

FIGURE 3.21: Pressure contours of Newtonian blood flow through a stenotic artery.

The pressure distribution for a laminar Newtonian blood flow is visually represented in Figure 3.21 using a range of colors, from red to blue. In this spectrum, red represents higher-pressure regions, while blue denotes lower-pressure areas. The `zeroGradient` condition at the inlet implies that the pressure gradient is zero in the normal direction to the boundary, which, combined with the uniform internal field, suggests an initially uniform pressure distribution upstream of the stenosis. As the blood flows through the constricted section, there is an observable drop in pressure, highlighted by the green to blue transition, which indicates the pressure loss due to the stenotic resistance. At the outlet, the pressure is set to a uniform value of zero, leading to a gradient towards this condition, as seen in the contour shift to blue.

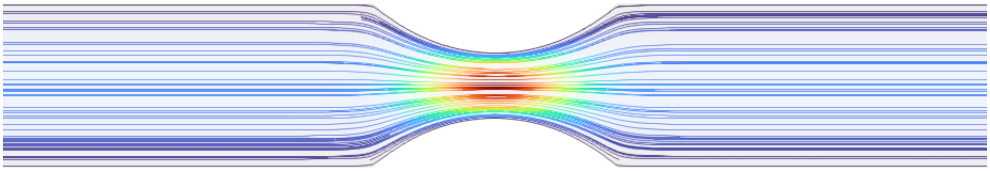

FIGURE 3.22: Streamline visualization depicting velocity magnitudes and flow patterns through the constriction.

The velocity magnitude of laminar blood flow with no initial components in the transverse directions is illustrated by the streamline graph shown in Figure 3.22. This type of pattern typically arises due to the acceleration of blood as it passes through the narrowed stenotic section, causing an increase in velocity magnitude. The boundary conditions specify a zero gradient at the outlet, allowing the flow to exit without resistance, and a no-slip condition at the walls, which enforces zero velocity at the boundary and captures the behavior of the fluid in contact with the arterial walls. The streamlines converge in the flow field, and the velocity magnitudes increase at the stenosis, visualizing the impact of the geometric constriction on the flow characteristics.

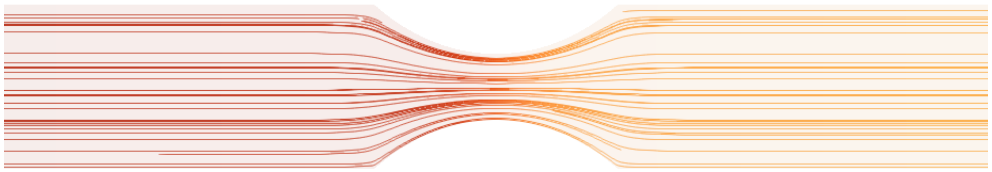

FIGURE 3.23: Streamline visualization depicting pressure magnitudes and flow patterns through the constriction.

Streamlines shown in Figure 3.23 indicate the direction and magnitude of the pressure gradients. These streamlines illustrate how the pressure changes from the inlet to the outlet through the stenotic region. The inlet and walls have a zero gradient pressure boundary condition, while the outlet has a fixed value of zero. The streamlines cluster and change color in the stenotic region, indicating the highest pressure gradients occur there due to the flow constriction. The red and orange streamlines represent higher pressure magnitudes, while cooler colors, such as blue, signify lower pressures. As the flow returns to a less constricted state downstream of the stenosis, the streamlines spread out, highlighting a decrease in the pressure gradient magnitude. This pattern is indicative of the decrease in pressure along the flow direction, with the most significant drop occurring at the point of constriction.

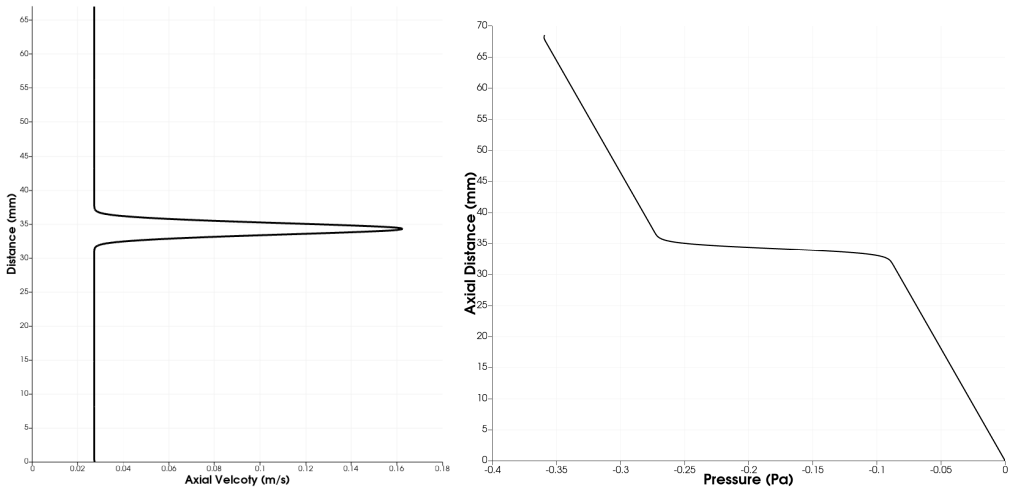

(A) (B)

FIGURE 3.24: Axial velocity (U_x) and pressure profile of Newtonian blood flow in a stenotic artery with a constant inlet velocity of $0.0137 m/s$.

The axial velocity magnitude and pressure along the arterial cross-section for laminar Newtonian blood flow at stenosis, calculated with a $Re \approx 200$, is depicted in the line plot illustrated in Figure 3.24. The simulation is constrained by given boundary conditions and maintains a constant inlet velocity of 0.0137m/s with a no-slip condition at arterial walls. Figure 3.24a shows a sharp increase in velocity at the stenosis due to the continuity equation, followed by a gradual decrease in velocity as the artery widens. The outlet's `zeroGradient` condition enables free outflow, ensuring no artificial back-pressure influences the velocity profile.
Pressure upstream of stenosis is uniform with zeroGradient boundary set at inlet.

This means no change in pressure normal to flow as shown in Figure 3.24b. The graph shows a significant pressure drop as the flow encounters the stenotic region. This pressure reduction results from increased flow resistance in the narrowed section, which causes energy loss in the system due to viscous dissipation and work done by the fluid to overcome the obstruction caused by the stenosis. Downstream of the stenosis, the pressure stabilizes at a lower level than the initial pressure, aligning with the zero pressure condition at the outlet. The pressure recovery observed after the stenosis suggests a return to less restrictive flow conditions.

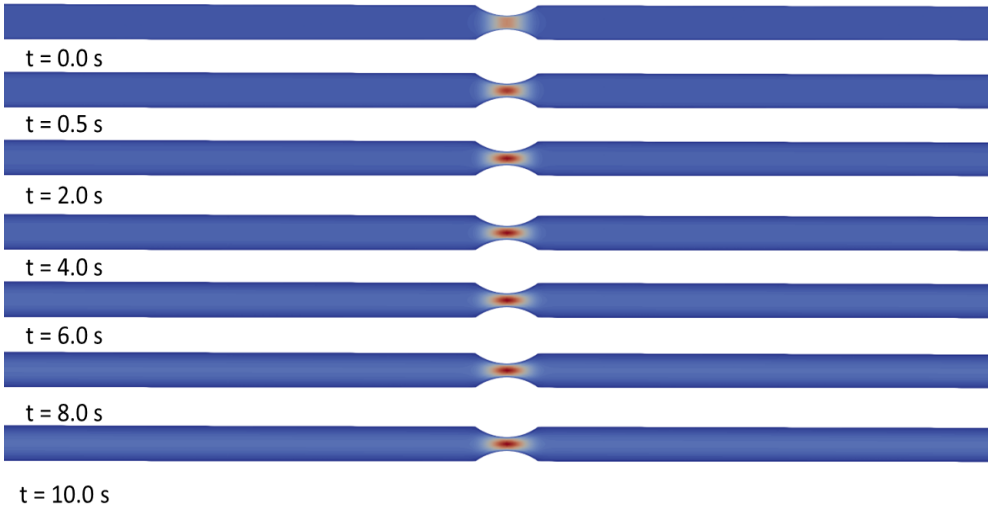

FIGURE 3.25: Temporal evolution of axial velocity U_x for constant inlet velocity.

Figure 3.25 depicts the progress of the axial velocity profile of laminar Newtonian blood flow through a stenotic artery at different time intervals. The velocity profile across the artery is uniform at $t = 0.0s$, which corresponds to the initial condition of zero velocity throughout the domain, except at the inlet, where the velocity is set to $0.0137m/s$. At $t = 0.5s$, the parabolic flow profile begins to develop, with higher velocities at the center of the artery. The stenosis causes a visible increase in velocity at the constriction as time advances to $t = 2.0s$ and beyond, and the flow becomes fully developed, exhibiting the characteristic blunted profile of laminar flow in a cylindrical tube, with the highest velocities at the center. The flow stabilizes and becomes steady in the post-stenotic region by $t = 4.0s$, and this pattern remains consistent through $t = 6.0s$, $t = 8.0s$, and up to $t = 10.0s$. The parabolic profile is preserved throughout the artery, except at the stenosis, where the profile sharply peaks due to the constriction. The no-slip condition at the walls creates a region where the velocity is zero.

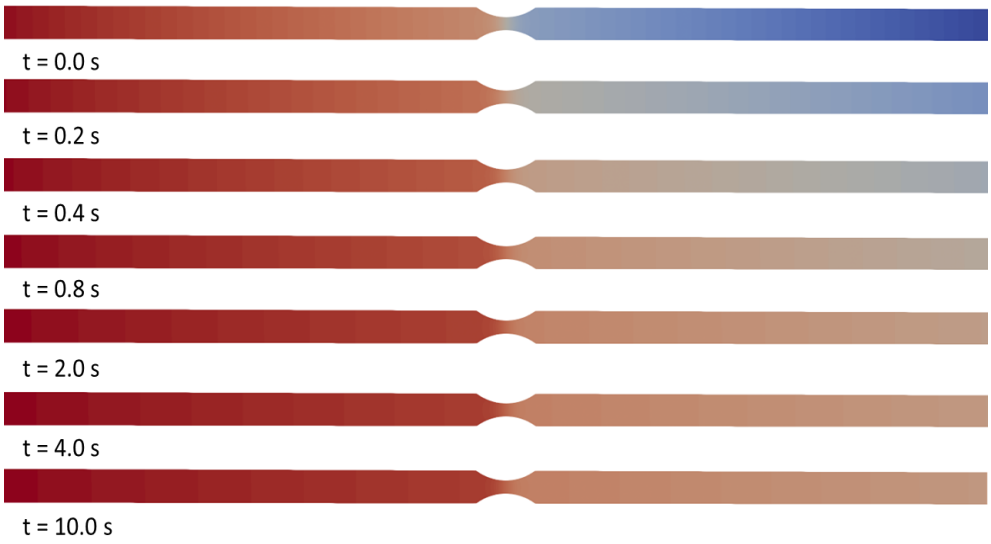

FIGURE 3.26: Temporal evolution of pressure for constant inlet velocity.

The temporal evolution of pressure distribution for laminar blood flow through an arterial cross-section is demonstrated in Figure 3.26 with the internal pressure field initially uniform at zero, with no pressure gradient imposed at the inlet and a fixed value of zero at the outlet. At $t = 0.0s$, the flow commences and the uniform internal pressure field represents the initial condition. At $t = 0.2s$, there are differences in pressure that appear due to the flow that is starting to form, caused by the constant velocity at the entrance. When the fluid moves through the narrow area, it encounters resistance, resulting in a decrease in pressure. Moving to $t = 0.4s$ and beyond, we observe a more pronounced pressure gradient, particularly at $t = 0.8s$, where the highest pressure drop is observed due to the fully developed flow. At $t = 2.0s$, the flow is likely in a steady state, with a consistent pressure profile. At times $t = 4.0s$ and $t = 10.0s$, there are no significant changes in the pressure profiles, indicating a steady flow and dissipation of initial transient effects.

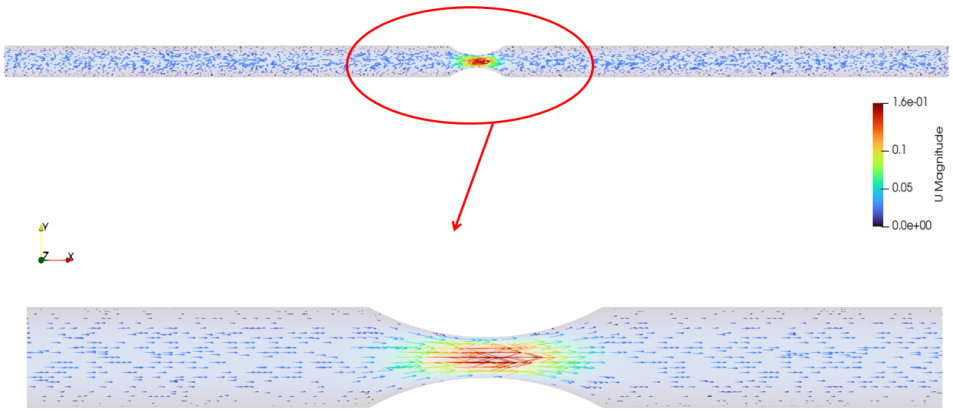

FIGURE 3.27: Velocity vectors for constant inlet.

Figure 3.27 displays a plot of the velocity vectors, which represent the direction and speed of blood flow through a stenosed arterial section at a constant inlet velocity computed with $Re = 200$. Within the stenotic region, the flow accelerates due to the constriction in the cross-sectional area, which is consistent with the continuity equation and conservation of mass. The velocity vectors show a significant increase in magnitude in this region. The longest red vectors, which indicate the highest velocities, are at the throat of the stenosis, highlighting a localized region of high kinetic energy. As the flow moves beyond the stenosis, the velocity vectors decrease in length, indicating that the flow is decelerating in the expanded area. This is due to the increase in area and the associated drop in flow speed. Finally, the `zeroGradient` condition at the outlet allows the velocity to gradually adjust to ambient conditions without imposing a specific gradient.

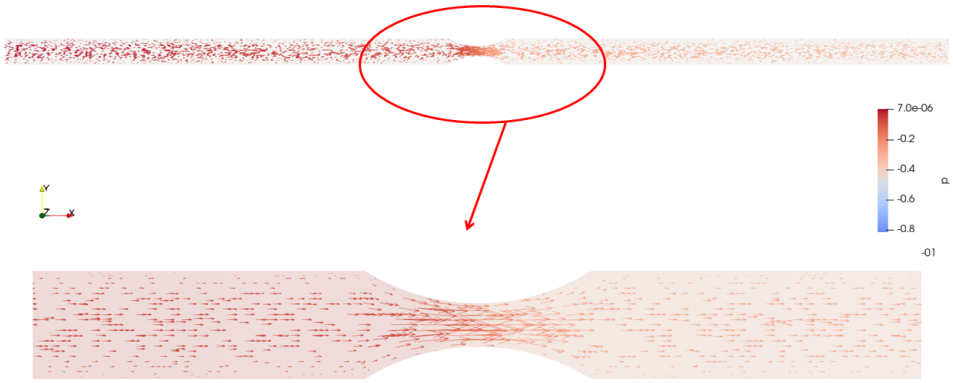

FIGURE 3.28: Pressure vectors for constant inlet.

The gradient of the pressure field within an arterial segment is visualized in Figure 3.28, representing the direction and magnitude of the greatest rate of change of pressure at each point within the flow field. At the inlet, the `zeroGradient` boundary condition allows pressure to adjust without a predetermined gradient. Thus, no significant pressure change occurs in the immediate inlet region until the velocity vectors progress through the artery, indicating where the pressure gradients are developing due to flow resistance. Vectors are pronounced at stenosis, indicating high-pressure gradients due to constriction. Pressure decreases upstream to downstream of stenosis. In the post-stenotic state, the pressure vectors diminish as the flow exits the constriction, and pressure begins to recover due to the widening of the arterial passage.

3.8 Concluding statments

This chapter presents a comprehensive analysis of flow momentum and pressure for Newtonian blood flow through an elliptical-shaped stenotic artery. The flow is assumed to be laminar and incompressible. The simulation was conducted using OpenFOAM. A 3D 70% stenotic arterial section was created using AutoCAD software, and the STL file was extracted as part of the pre-processing step. The next step

involved generating a high-quality mesh using `blockMesh` and `snappyHexMesh` utilities in OpenFOAM. The `icoFoam` solver was used for incompressible and laminar flow, which employs the finite volume method. Two main cases were examined for Newtonian blood flow, namely, flow initialized by parabolic inlet velocity and flow initialized by constant inlet velocity. For both cases, blood velocity and pressure were studied at the narrowest part of the stenosis and for the overall stenotic arterial lumen to gain a better understanding of the flow dynamics. The main findings are:

- **Line plots:** At the center of stenosis in Figure 3.9 and Figure 3.19, the velocity magnitude and pressure distribution exhibit a parabolic curve for the parabolic velocity inlet profile and the constant inlet velocity. The maximum velocity is at the center of stenosis, while the pressure drops to its lowest value at the same location. In both Figure 3.14 and Figure 3.24, the pre and post-stenotic sections maintain a constant value of U_x but indicate a sudden rise in momentum at the stenotic section. The pressure remains consistent in the pre-stenotic region and exhibits a sharp decline in pressure at the stenosis, which stabilizes at the post-stenotic section due to zero pressure conditions.

- **Contours:** Figure 3.10 and Figure 3.11 presents velocity and pressure contours for parabolic inlet velocity whereas Figure 3.20 and Figure 3.21 are the velocity and pressure contours for Newtonian blood flow through stenotic artery. The flow moves towards a narrow stenotic region, creating a recirculation zone after it. Pressure remains constant in the pre-stenotic region but low pressure is observed in the stenosis section. Pressure recovery is observed in the post-stenotic region.

- **Streamlines:** The initial blue streamlines at the beginning of the arterial section, as seen in Figure 3.12 and Figure 3.22, indicate low velocity. The blue streamlines turn red at the stenosis, indicating maximum flow at the stenosis site. Following the stenosis, recirculating zones can be observed. Figures 3.13 and 3.23 display evenly spaced pressure streamlines, which signify laminar flow. At the core of the stenosis, a pressure drop is noticed. Downstream of the stenosis, a decrease in the magnitude of the pressure gradient is observed.

- **Time-lapse graphs:** Figure 3.15 and Figure 3.25 exhibit the velocity of blood flow passing through a stenotic artery. The flow becomes intricate due to the narrowing, and downstream of the stenosis, distinct separation zones can be observed. At t=10.0s, the flow reaches a state of quasi-steadiness. The evolution of the pressure field is rendered in Figure 3.16 and 3.26. The pressure gradually develops along the artery, exhibiting a gradient towards the outlet. The stenotic region exhibits a localized low-pressure zone due to the accelerated flow speeds in the constriction.

- **Vector plots:** The velocity vectors change significantly in Figures 3.17 and 3.27 through the stenosis, indicating increased velocity due to reduced cross-sectional area. The highest speeds occur at the throat of the constriction, and significant changes in the flow are observed within and immediately downstream of the stenosis. Figure 3.18 and Figure 3.28 describe the pressure distribution and vectors along an arterial segment simulated for laminar Newtonian blood. The pressure vectors become concentrated and pronounced at the stenosis point, indicating an increase in the pressure gradient due to flow restriction. Pressure gradients develop due to flow resistance and are high at

stenosis. The pressure recovers due to the widening of the arterial passage in the post-stenotic state.

Conclusions

This dissertation explores the dynamics of blood flow in constricted arteries using computational fluid dynamics techniques and fluid models. It contributes to the understanding of blood behavior under various conditions influenced by physiological and non-physiological factors. The study also provides insights into the interplay between fluid mechanics and the cardiovascular system, paving the way for further research.

Chapter 1 centers on the study of the time-dependent, axisymmetric flow of a hybrid nanofluid comprised of Cu-Al_2O_3-blood through elliptical-shaped stenotic arteries. Employing the Casson fluid model to describe the non-Newtonian nature of blood, the study explores the influence of pulsatile pressure gradients, magnetic fields, and nanoparticle additives on the flow dynamics. The numerical simulations are performed using the Forward Time Central Space method (FTCS). An extensive analysis of the velocity and temperature distributions is done, quantifying the effects of various parameters over mass and heat transfer using the graphical and tabular representations. The wall shear stress and local Nusselt number analysis also highlight the complexity of blood flow in restricted conditions. The Casson model parameters and magnetic field have been observed to increase the momentum profile, while variations in Reynolds number, Hall current parameter, and particle volume fractions showed opposite results. Applied magnetic field, Eckert number, and particle volume fraction have a favorable effect on the Cu-Al_2O_3-blood's temperature profile, while the Casson parameter, Hall current parameter, Reynolds number, and Prandtl number have an adverse effect.

Chapter 2 expands the laminar flow analysis of Chapter 1 to the conditions of turbulent blood flow by introducing the Casson model with copper and alumina nanoparticles. We began by converting the Navier-Stokes equations (NSE) to Reynolds-averaged Navier-Stokes equations (RANS) by separating the flow variables into average and fluctuating components. This was done in the context of the presence of nanoparticles, pulsatile pressure gradient, and magnetohydrodynamic effects on flow properties. The Reynold stress term was then further modeled by the zero equation turbulence model. Numerical simulation for mean flow velocity was carried out using the FTCS method. The findings from this chapter enhance our understanding of turbulent flow in blocked arteries, indicating significant changes in velocity profiles and wall shear stresses due to the non-Newtonian properties of blood and the presence of nanoparticles.

In Chapter 3, attention is directed towards laminar flow conditions within a 3D stenotic artery that is modeled realistically. An obstructed part of an artery was produced using AutoCAD software, and subsequently, the STL file was utilized by OpenFOAM, which offers open-source packages for computational fluid dynamics using C++ programming. First, a high-quality mesh of a stenotic arterial section using the blockMesh and snappyHexMesh utilities was generated. The computational domain was decomposed into four subdomains to accelerate the simulation procedure. The following stage involves utilizing the icoFoam solver to perform simulations of laminar and incompressible flows. The simulations aimed to evaluate the

impact of parabolic and constant inlet velocity profiles on momentum and pressure distributions within the stenosed artery. Through a comprehensive analysis of velocity and pressure changes at the narrowest point of the stenosis and throughout the arterial section, important insights are gained into the physical phenomena that occur during blood flow.
Hence, this research provides insights into narrow arteries' velocity and temperature distributions. These insights can lead to the development of more precise diagnostic tools. Understanding the influence of various factors on blood flow can help in creating targeted diagnostic and monitoring technologies that can assess patient-specific cardiovascular risks more effectively. Additionally, the study analyzes the impact of nanoparticles in blood, which can pave the way for advanced treatment techniques. These techniques include the targeted delivery of drugs to specific sites within the vascular system.

Future research directions

- One potential next step is to finalize Case 1.7.2 from Chapter 1, which has yet to be fully explored. It could provide insight into hybrid nanofluid dynamics regarding cardiovascular applications by uncovering more intricate flow behaviors under diverse conditions.

- In Chapter 3, a laminar case was presented for the Newtonian model, which can be adapted for the non-Newtonian Casson model with further modifications. An effective enhancement can be achieved by analyzing the properties of the flow. Additionally, turbulent analysis of blood flow can be conducted while introducing nanoparticles to gain a better understanding of drug delivery in CFD.

Appendix A

Fundamental Equations Of Fluid Dynamics.

Fluid dynamics aims to accurately calculate the velocity field of a fluid and understand its complex motion, influenced by factors such as pressure, temperature, and viscosity. Studying the velocity field helps researchers and engineers understand fluid behavior to improve system efficiency. This relies on equations predicting fluid velocity and pressure, considering boundary conditions like inlets, outlets, and walls. These complex equations have limited analytical solutions. Simple geometries, like the flow between two parallel plates or a circular pipe, have straightforward solutions, but more complex geometries require sophisticated solutions. Within this particular section, we aim to derive the essential equations that are utilized to encapsulate the widely recognized principles of mechanics:

1. Conservation of mass (see A.1)
2. Conservation of momentum (see A.2)

The Eulerian approach for deriving the conservation of mass and momentum is foundational in fluid dynamics. It involves observing the behavior of fluid properties at fixed points in space over time. By focusing on a control volume, the Eulerian framework facilitates the analysis of fluid flow and the interactions of different fluid elements within that volume, enabling precise predictions of fluid behavior under various conditions. Fluids consist of individual molecules with different physical properties like density and velocity at a microscopic level. However, when it comes to fluid dynamics, the focus is on macroscopic phenomena, not on the molecular level. Instead, fluid is treated as a continuum and viewed on a larger scale where many molecules make up each "small" fluid element. To assign an average bulk flow velocity $V(x,t)$ to each element at point x, faster, fluctuating Brownian molecular velocities are averaged. Similarly, a locally averaged density $\rho(x,t)$ is defined, and these quantities smoothly vary with x on the macroscopic scale of the flow.

A.1 Conservation of mass

To obtain the continuity equation, we begin by considering a compressible fluid flowing through a tiny control volume with a length of Δx, height of Δz, and width of Δy. The volume element allows for the movement of fluid in and out through multiple surfaces. For the sake of simplicity, we consider only a flow in the x-direction. Within an infinitesimal time dt, a certain mass $dm_x(in)$ flows in, and $dm_x(out)$ flows out of the control volume simultaneously. As the fluid enters the specified volume element, it possesses a particular magnitude of velocity $v_x(in)$, so the distance it

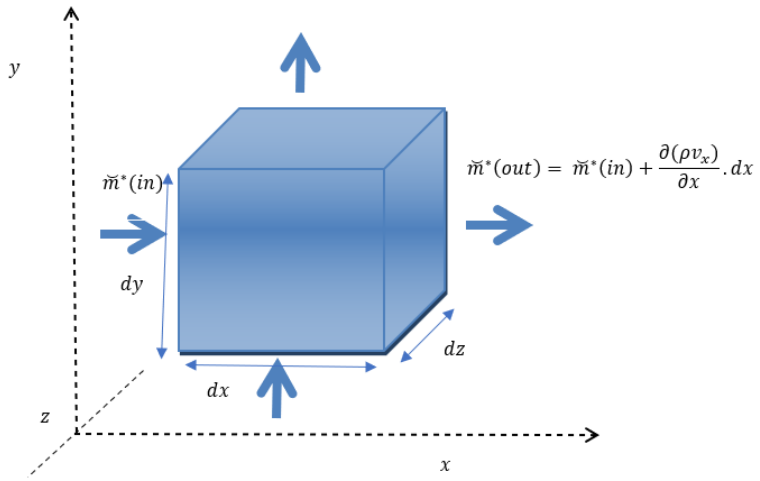

FIGURE A.1: Fluxes of mass that enter and exit an element.

travels in time dt is $dx_x(in) = v_x(in) \cdot dt$. As a result, the volume enters the control volume:

$$dV_x(in) = \Delta A \cdot dx_x(in) = \Delta A \cdot v_x(in) \cdot dt$$

If the density of the fluid flowing in the control volume is $\rho_x(in)$ then inflow mass will be:

$$dm_x(in) = dv_x(in) \cdot \rho_x(in) = \Delta A \cdot \rho_x(in) \cdot v_x(in) \cdot dt$$

The mass flow rate into the control volume depends only on density and velocity per unit area. The mass flow rate specific to this area or mass flux $(m_x^*(in))$ which indicates the mass flow in the flow direction per unit time and the unit area:

$$m_x^*(in) = \frac{dm_x(in)}{\Delta A \cdot dt} = \rho_x(in) \cdot v_x(in)$$

or

$$\boxed{m^* = \rho \cdot v} \tag{A.1}$$

When dealing with compressible fluids, the density in a flow field typically varies from point to point. For instance, if the fluid collects in the control volume being studied, the density and the flow velocity at the outflow of the volume will be different from the inflow. However, we can still calculate the mass flux at both the outflow and inflow using the same method (equation (A.1))

$$m_x^*(out) = \rho_x(out) \cdot v_x(out)$$

The rate of change of mass $(\breve{m})$ in x-direction:

$$\breve{m} = \breve{m}_x(in) - \breve{m}_x(in) \tag{A.2}$$

$$\check{m} = \check{m}_x^*(in) \cdot \Delta A - \check{m}_x^*(out) \cdot \Delta A$$

$$\boxed{\check{m} = \check{m}_x^*(in) \cdot \Delta y \Delta z - \check{m}_x^*(out) \cdot \Delta y \Delta z} \tag{A.3}$$

Now consider a control volume in a compressible flow. Within this volume, the mass flow rate and the product of density and velocity along the x-axis undergo changes. From these variations, we can establish a mass flow rate gradient along the x-axis $(d\check{m}_x^*)$

$$d\check{m}_x^* = \frac{\partial(\rho \cdot v_x)}{\partial x} \cdot dx \tag{A.4}$$

Thus, the mass flux at the control volume's outflow is determined as:

$$\check{m}_x^*(out) = \check{m}_x^*(in) + d\check{m}_x^*$$

or

$$\check{m}_x^*(out) = \check{m}_x^*(in) + \frac{\partial(\rho \cdot v_x)}{\partial x} \cdot dx \tag{A.5}$$

The equation for determining the temporal change of mass $(\check{m})$ using equation (A.2) within the control volume is:

$$\check{m} = \check{m}_x^*(in).dydz - \check{m}_x^*(out) \cdot dydz$$

$$\check{m} = \check{m}_x^*(in) \cdot dydz - \left(\check{m}_x^*(in) + \frac{\partial(\rho \cdot v_x)}{\partial x} \cdot dx\right) \cdot dydz$$

$$\check{m} = \cancel{\check{m}_x^*(in) \cdot dydz} - \cancel{\check{m}_x^*(in) \cdot dydz} - \frac{\partial(\rho \cdot v_x)}{\partial x} \cdot dxdydz$$

$$\check{m} = -\frac{\partial(\rho \cdot v_x)}{\partial x} \cdot dxdydz = -\frac{\partial(\rho \cdot v_x)}{\partial x} \cdot dv \tag{A.6}$$

When the gradient is positive, the mass in the volume element experiences a decrease over time. This is because the outgoing mass flow is greater than the incoming mass flow, and the negative sign serves as an indicator of this phenomenon. If the mass within a volume changes over time, its density ρ changes too:

$$\check{m} = -\frac{\partial \rho}{\partial t} \cdot dv \tag{A.7}$$

Using equation (A.5) and equation (A.6), The gradient of the mass flux and resulting temporal change of density at one point in the flow are related as follows:

$$\frac{\partial \rho}{\partial t} \cdot \cancel{dv} = -\frac{\partial(\rho.v_x)}{\partial x} \cdot \cancel{dv}$$

$$\frac{\partial \rho}{\partial t} = -\frac{\partial(\rho \cdot v_x)}{\partial x} \tag{A.8}$$

Equation (A.9) is called continuity equation (in one dimension). Similarly, the continuity equation for three-dimensional flow is:

$$\frac{\partial \rho}{\partial t} + \vec{\nabla} \cdot (\rho \vec{v}) = 0. \tag{A.9}$$

A.2 Conservation of momentum

In the realm of physics, the conservation of momentum is a fundamental and unshakable principle. It posits that if there are no external forces acting upon a closed system, the total momentum remains constant. This law has far-reaching implications in the study of motion and helps us understand the behavior of objects in motion. For this, we delve deeper into the nature of fluid elements and the various forces that impact them.
For now, we will concentrate solely on the fluid's movement in the x-direction. The fluid element's motion is determined by the pressure forces exerted on its front and back surfaces, which can be likened to normal stresses and are denoted by the Greek symbol (σ) in the subsequent text. The normal stresses on the front and back of a fluid element differ due to pressure changes in the flow direction. Therefore, a pressure gradient and a normal stress gradient $(\partial \sigma_x / \partial x)$ are located at the considered point x and the change in normal stress (σ_x) at point x along dx is $(\partial \sigma_x / \partial x \cdot dx)$. Now the pressure-dependent normal forces acting at points x and dx on the fluid volume element are:

$$F_x = \sigma_x \cdot dA_{yz} \qquad \text{normal force at } x$$

$$F_{x+dx} = \left(\sigma_x + \frac{\partial \sigma_x}{\partial x} dx\right) dA_{yz} \qquad \text{normal force at } x + dx$$

The resulting normal force will be the difference of above normal forces as these forces are acting in different directions on a volume element:

$$F_{\sigma x} = F_x - F_{x+dx}$$

$$= \cancel{\sigma_x \cdot dA_{yz}} - \cancel{\sigma_x dA_{yz}} - \frac{\partial \sigma_x}{\partial x} dx dA_{yz}$$

$$\boxed{F_{\sigma x} = -\frac{\partial \sigma_x}{\partial x} dV \qquad \text{The normal force resulting in the x-direction.}}$$

As fluid possesses high viscosity η, it undergoes shear forces or stresses that affect its top and bottom surfaces in the x-direction and its lateral surfaces. In contrast to normal stresses perpendicular to the surface, shear stresses run parallel. The shear stress τ_{ij} is determined using Newton's law of friction. The normal direction to the surfaces is denoted by $i = (y, z)$ and the direction in which τ_{ij} acts is denoted by $j = (x)$:

$$\boxed{\tau_{ij} = \tau_{yx} = \eta \cdot \frac{\partial v_j}{\partial i}}$$

As the fluid element's width (dy) changes, the velocity gradient $(\partial v_x / \partial y)$ also changes. This means a different shear stress will be present at the position $(y + dy)$. We can

define a corresponding shear stress gradient $(\partial\tau_{yx}/\partial y)$ at this point, resulting in the following shear stress at $(y + dy)$:

$$\tau_{yx} + \frac{\partial\tau_{yx}}{\partial y}dy$$

In practical terms, a positive shear stress gradient means that, as per Newton's law of fluid friction, the velocity gradient increases in the y direction. This indicates that the flow velocity at the location $y + dy$ is greater than at the location y. When observing the flow direction (positive x-direction), the fluid moves slower to the right of the fluid element and faster to the left. On the right side, the fluid element decelerates while on the left side, it accelerates due to the flow. This causes the shear stress at point y to be directed in the negative x direction and at point $y + dy$ in the positive direction. The difference between these two shear stresses is the resulting shear stress on the two lateral surfaces.

$$\tau_{yx_{final}} = \text{Shear stress at y+dy} - \text{Shear stress at y}$$

$$\tau_{yx_{final}} = \tau_{yx} + \frac{\partial\tau_{yx}}{\partial y} \cdot dy - \tau_{yx}$$

$$\tau_{yx_{final}} = \frac{\partial\tau_{yx}}{\partial y} \cdot dy.$$

Now, the force $F_{\tau yx}$ acting on the lateral surface of the fluid element will be the product of shear stress per unit area and area dA_{xz}

$$F_{\tau yx} = \tau_{yx \cdot final} \cdot dA_{xz}$$

$$F_{\tau yx} = \frac{\partial\tau_{yx}}{\partial y} \cdot dy.dA_{xz}$$

$$\boxed{F_{\tau_{yx}} = \frac{\partial\tau_{yx}}{\partial y} \cdot dV}$$

Likewise, the perpendicular force exerted on the upper and lower regions of the fluid component is applied in a comparable manner.

$$F_{\tau_{zx}} = \frac{\partial\tau_{zx}}{\partial z} \cdot dV$$

In addition to normal and shear forces, the behavior of a fluid element is also influenced by the force of gravity. It's worth noting that the flow in the x-direction can vary in angle and may not always be horizontal. In such situations, only the component of the weight force F_{gx} that points in the x-direction is of significance. The symbol g_x is representative of the component of gravitational acceleration that acts in the x-direction.

$$F_{g_x} = dm \cdot g_x$$

When analyzing the behavior of fluids, it is important to consider the various forces that may be acting on them. Weight force is a type of body force that affects the entire fluid element, rather than just its surfaces. This means that it is exerted on the "body" of the fluid, rather than on specific points. In addition to weight force, there may be other types of body forces to take into account, such as electrical or magnetic forces. By understanding the different forces that may be at play, we can

gain a better understanding of how fluids behave in different situations. So the force of weight acting on the fluid element in the x-direction is:

$$\boxed{F_{g_x} = \rho g_x \cdot dV}$$

The consequential force acting on a fluid element in the x-direction is the sum of normal force $F_{\sigma x}$, shear forces $F_{\tau_{yx}}$ and $F_{\tau_{zx}}$, and body force F_{g_x}:

$$F_{x_{final}} = F_{\sigma_x} + F_{\tau_{yx}} + F_{\tau_{zx}} + F_{g_x}$$

$$F_{x_{final}} = -\frac{\partial \sigma_x}{\partial x} \cdot dV + \frac{\partial \tau_{yx}}{\partial y} \cdot dV + \frac{\partial \tau_{zx}}{\partial z} \cdot dV + \rho g_x \cdot dV$$

It follows from Newton's second law that this resultant force produces the acceleration a_x with $dm = \rho dV$ denotes the mass of fluid element:

$$a_x = \frac{F_{x_{final}}}{dm} = \frac{F_{x_{final}}}{\rho dV} = \frac{\cancel{dV}(-\frac{\partial \sigma_x}{\partial x} + \frac{\partial \tau_{yx}}{\partial y} + \frac{\partial \tau_{zx}}{\partial z} + \rho g_x)}{\rho \cancel{dV}}$$

$$a_x = \frac{-\frac{\partial \sigma_x}{\partial x} + \frac{\partial \tau_{yx}}{\partial y} + \frac{\partial \tau_{zx}}{\partial z} + \rho g_x}{\rho} \tag{A.10}$$

The alteration in the velocity of a fluid element in the x-direction, referred to as substantial acceleration a_x, can be determined by two factors. Firstly, calculating the change in velocity over time at a fixed location, known as local acceleration $(\partial v_x / \partial t)$. Secondly, by taking into account the change in velocity resulting from the movement of the fluid element itself, known as convective acceleration $(\partial v_x / \partial x . v_x + \partial v_x / \partial y \cdot v_y + \partial v_x / \partial z \cdot v_z)$:

$$\underbrace{a_x}_{\text{Substantial Acceleration}} = \underbrace{\frac{\partial v_x}{\partial t}}_{\text{Local Acceleration}} + \underbrace{\frac{\partial v_x}{\partial x} \cdot v_x + \frac{\partial v_x}{\partial y} \cdot v_y + \frac{\partial v_x}{\partial z} \cdot v_z}_{\text{Convective Acceleration}} \tag{A.11}$$

The relationship at hand for substantial, local, and convective acceleration can be accurately characterized through the Euler equation. In the event that the equation for significant acceleration (A.11) is incorporated into the aforementioned equation (A.10), the resulting connection can be expressed as follows:

$$\boxed{\left(\frac{\partial v_x}{\partial t} + \frac{\partial v_x}{\partial x} \cdot v_x + \frac{\partial v_x}{\partial y} \cdot v_y + \frac{\partial v_x}{\partial z} \cdot v_z\right)\rho = -\frac{\partial \sigma_x}{\partial x} + \frac{\partial \tau_{yx}}{\partial y} + \frac{\partial \tau_{zx}}{\partial z} + \rho g_x} \tag{A.12}$$

When a fluid is in motion, its velocity and velocity gradient change along all directions. Due to the fluid's viscosity, the shear stress is influenced not only by the velocity gradient in a certain direction but also by the velocity gradient perpendicular to it. It is a mathematical construct that accounts for the internal frictional forces that arise within a fluid when it is subjected to deformation. This leads to the deformation of the fluid element, where the shear forces cause inclined surfaces, which in turn affect another spatial dimension. However, in fluids, the stresses that act in additional spatial directions are not due to actual deformation but rather the shear rate. To describe these stresses, including normal and shear stresses, acting on a fluid element, the introduction of a viscous stress tensor is necessary. The tensor has nine

components, each of which represents a different component of the stress.

$$\tau = \begin{bmatrix} \tau_{xx} & \tau_{xy} & \tau_{xz} \\ \tau_{yx} & \tau_{yy} & \tau_{yz} \\ \tau_{zx} & \tau_{zy} & \tau_{zz} \end{bmatrix} \tag{A.13}$$

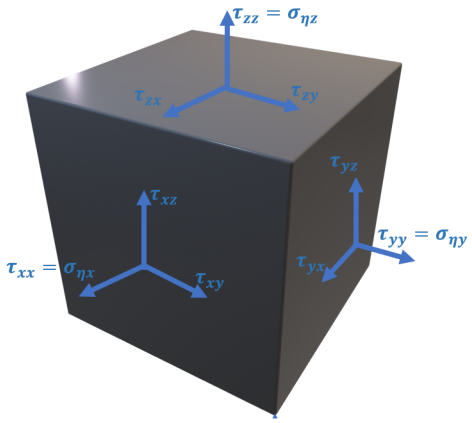

FIGURE A.2: The normal and Shear Stresses of viscous stress tensor

Assuming a Newtonian fluid is isotropic, where the fluid mechanical properties are considered to be consistent in all directions, the components of the viscous stress tensor τ can be determined as follows:

$$\tau = \eta. \begin{bmatrix} \left(\frac{\partial v_x}{\partial x} + \frac{\partial v_x}{\partial x}\right) & \left(\frac{\partial v_x}{\partial y} + \frac{\partial v_y}{\partial x}\right) & \left(\frac{\partial v_x}{\partial z} + \frac{\partial v_z}{\partial x}\right) \\ \left(\frac{\partial v_y}{\partial x} + \frac{\partial v_x}{\partial y}\right) & \left(\frac{\partial v_y}{\partial y} + \frac{\partial v_y}{\partial y}\right) & \left(\frac{\partial v_y}{\partial z} + \frac{\partial v_z}{\partial y}\right) \\ \left(\frac{\partial v_z}{\partial x} + \frac{\partial v_x}{\partial z}\right) & \left(\frac{\partial v_z}{\partial y} + \frac{\partial v_y}{\partial z}\right) & \left(\frac{\partial v_z}{\partial z} + \frac{\partial v_z}{\partial z}\right) \end{bmatrix} \tag{A.14}$$

To determine the individual entries of the viscous stress tensor:

$$\boxed{\tau_{ij} = \eta\left(\frac{\partial v_i}{\partial j} + \frac{\partial v_j}{\partial i}\right)} \tag{A.15}$$

In equation (A.12), the shear stresses are:

$$\tau_{yx} = \eta\left(\frac{\partial v_y}{\partial x} + \frac{\partial v_x}{\partial y}\right) \tag{A.16}$$

$$\tau_{zx} = \eta\left(\frac{\partial v_z}{\partial x} + \frac{\partial v_x}{\partial z}\right) \tag{A.17}$$

The normal stresses in equations (A.13) and (A.14), marked as red and are diagonal, have both normal and effective directional forces in the same direction and are denoted as σ. It is worth noting that viscosity not only produces shear stresses but also normal stresses. Subsequently, these normal stresses that arise from the viscosity of a fluid are also designated with the symbol for viscosity η and using equation (A.15)

$$\tau_{xx} = \sigma_{\eta x}, \quad \tau_{yy} = \sigma_{\eta y}, \quad \tau_{zz} = \sigma_{\eta z},$$

$$\tau_{xx} = \sigma_{\eta x} = \eta\left(\frac{\partial v_x}{\partial x} + \frac{\partial v_x}{\partial x}\right) = 2\eta\frac{\partial v_x}{\partial x}.$$

The viscous normal stress is a type of force that is exerted on a fluid element. This force acts perpendicularly to the fluid element and is in addition to the static pressure. Unlike the static pressure, which is directed towards the fluid element, the viscous normal stress operates in the opposite direction, i.e., away from the fluid element. This force is caused by the internal friction between fluid molecules. The viscous normal stress can be thought of as a force that pulls the fluid element away from the surface normal, and it is particularly relevant in the study of fluid mechanics and fluid dynamics. So, the resulting normal stress will be:

$$\sigma_x = p - \sigma_{\eta x} = p - 2\eta\frac{\partial v_x}{\partial x}. \tag{A.18}$$

Now using equations (A.16), (A.17) and (A.18) in the right side of (A.12):

$$\left(\frac{\partial v_x}{\partial t} + \frac{\partial v_x}{\partial x}\cdot v_x + \frac{\partial v_x}{\partial y}\cdot v_y + \frac{\partial v_x}{\partial z}\cdot v_z\right)\rho = -\frac{\partial \sigma_x}{\partial x} + \frac{\partial \tau_{yx}}{\partial y} + \frac{\partial \tau_{zx}}{\partial z} + \rho g_x$$

$$= -\frac{\partial}{\partial x}\left(p - 2\eta\frac{\partial v_x}{\partial x}\right) + \eta\frac{\partial}{\partial y}\left(\frac{\partial v_y}{\partial x} + \frac{\partial v_x}{\partial y}\right) + \eta\frac{\partial}{\partial z}\left(\frac{\partial v_z}{\partial x} + \frac{\partial v_x}{\partial z}\right) + \rho g_x$$

$$= -\frac{\partial p}{\partial x} + 2\eta\frac{\partial^2 v_x}{\partial x^2} + \eta\frac{\partial}{\partial y}\left(\frac{\partial v_y}{\partial x}\right) + \eta\frac{\partial^2 v_x}{\partial y^2} + \eta\frac{\partial}{\partial z}\left(\frac{\partial v_z}{\partial x}\right) + \eta\frac{\partial^2 v_x}{\partial z^2} + \rho g_x$$

$$= -\frac{\partial p}{\partial x} + \eta\frac{\partial^2 v_x}{\partial x^2} + \eta\frac{\partial}{\partial x}\left(\frac{\partial v_x}{\partial x}\right) + \eta\frac{\partial}{\partial y}\left(\frac{\partial v_y}{\partial x}\right) + \eta\frac{\partial^2 v_x}{\partial y^2} + \eta\frac{\partial}{\partial z}\left(\frac{\partial v_z}{\partial x}\right) + \eta\frac{\partial^2 v_x}{\partial z^2} + \rho g_x,$$

by rearranging:

$$= -\frac{\partial p}{\partial x} + \eta\left(\frac{\partial^2 v_x}{\partial x^2} + \frac{\partial^2 v_y}{\partial y^2} + \frac{\partial^2 v_z}{\partial z^2}\right) + \eta\frac{\partial}{\partial x}\left(\frac{\partial v_x}{\partial x}\right) + \eta\frac{\partial}{\partial x}\left(\frac{\partial v_x}{\partial y}\right) + \eta\frac{\partial}{\partial x}\left(\frac{\partial v_x}{\partial z}\right) + \rho g_x,$$

or

$$= -\frac{\partial p}{\partial x} + \eta\left(\frac{\partial^2 v_x}{\partial x^2} + \frac{\partial^2 v_y}{\partial y^2} + \frac{\partial^2 v_z}{\partial z^2}\right) + \eta\frac{\partial}{\partial x}\underbrace{\left(\frac{\partial v_x}{\partial x} + \frac{\partial v_x}{\partial y} + \frac{\partial v_x}{\partial z}\right)}_{0} + \rho g_x,$$

The following equation serves to describe, in a precise and formal manner, the motion of an incompressible fluid as a continuum in the x-direction:

$$\left(\frac{\partial v_x}{\partial t} + \frac{\partial v_x}{\partial x}.v_x + \frac{\partial v_x}{\partial y}.v_y + \frac{\partial v_x}{\partial z}.v_z\right)\rho = -\frac{\partial p}{\partial x} + \eta\left(\frac{\partial^2 v_x}{\partial x^2} + \frac{\partial^2 v_y}{\partial y^2} + \frac{\partial^2 v_z}{\partial z^2}\right) + \rho g_x, \tag{A.19}$$

Analogous equations apply for motion in y- and z-directions.

$$\left(\frac{\partial v_y}{\partial t}+\frac{\partial v_y}{\partial x}\cdot v_x+\frac{\partial v_y}{\partial y}\cdot v_y+\frac{\partial v_y}{\partial z}\cdot v_z\right)\rho=-\frac{\partial p}{\partial y}+\eta\left(\frac{\partial^2 v_y}{\partial x^2}+\frac{\partial^2 v_y}{\partial y^2}+\frac{\partial^2 v_y}{\partial z^2}\right)+\rho g_y, \tag{A.20}$$

$$\left(\frac{\partial v_z}{\partial t}+\frac{\partial v_z}{\partial x}\cdot v_x+\frac{\partial v_z}{\partial y}\cdot v_y+\frac{\partial v_z}{\partial z}\cdot v_z\right)\rho=-\frac{\partial p}{\partial z}+\eta\left(\frac{\partial^2 v_z}{\partial x^2}+\frac{\partial^2 v_z}{\partial y^2}+\frac{\partial^2 v_z}{\partial z^2}\right)+\rho g_z, \tag{A.21}$$

So the Navier-Stokes equation for the incompressible fluids is:

$$\rho\Bigg[\underbrace{\frac{\partial\vec{v}}{\partial t}}_{\substack{\text{Local}\\ \text{Acceleration}}}+\underbrace{\vec{v}(\vec{v}\cdot\vec{\nabla})}_{\substack{\text{Convective}\\ \text{Acceleration}}}\Bigg]=-\underbrace{\vec{\nabla}p}_{\substack{\text{Pressure Force/}\\ \text{Normal Force}}}+\underbrace{\eta(\vec{\nabla}^2\vec{v})}_{\substack{\text{Frictional Force/}\\ \text{Shear Force}}}+\underbrace{\rho\vec{g}}_{\substack{\text{Weight Force/}\\ \text{Body Force}}} \tag{A.22}$$

In cylindrical coordinates:

$$\left(\frac{\partial v_r}{\partial t}+\frac{\partial v_r}{\partial r}v_r+\frac{\partial v_r}{\partial\theta}\frac{v_\theta}{r}-\frac{v_\theta^2}{r}+\frac{\partial v_r}{\partial z}v_z\right)\rho=-\frac{\partial p}{\partial r}+\eta\left(\frac{\partial}{\partial r}\left(\frac{1}{r}\frac{\partial(rv_r)}{\partial r}\right)+\right.$$

$$\left.\frac{1}{r^2}\frac{\partial^2 v_r}{\partial\theta^2}-\frac{2}{r^2}\frac{\partial v_\theta}{\partial\theta}+\frac{\partial^2 v_r}{\partial z^2}\right)+\rho g_r, \tag{A.23}$$

$$\left(\frac{\partial v_\theta}{\partial t}+\frac{\partial v_\theta}{\partial r}v_r+\frac{\partial v_r}{\partial\theta}\frac{v_\theta}{r}+\frac{v_\theta v_r}{r}+\frac{\partial v_\theta}{\partial z}v_z\right)\rho=-\frac{1}{r}\frac{\partial p}{\partial\theta}+\eta\left(\frac{\partial}{\partial r}\left(\frac{1}{r}\frac{\partial(rv_\theta)}{\partial r}\right)+\right.$$

$$\left.\frac{1}{r^2}\frac{\partial^2 v_\theta}{\partial\theta^2}+\frac{2}{r^2}\frac{\partial v_r}{\partial\theta}+\frac{\partial^2 v_\theta}{\partial z^2}\right)+\rho g_\theta, \tag{A.24}$$

$$\left(\frac{\partial v_z}{\partial t}+\frac{\partial v_z}{\partial r}v_r+\frac{\partial v_z}{\partial\theta}\frac{v_\theta}{r}+\frac{\partial v_z}{\partial z}v_z\right)\rho=-\frac{\partial p}{\partial z}+\eta\left(\frac{1}{r}\frac{\partial}{\partial r}\left(r\frac{\partial(v_z)}{\partial r}\right)+\right.$$

$$\left.\frac{1}{r^2}\frac{\partial^2 v_z}{\partial\theta^2}+\frac{\partial^2 v_z}{\partial z^2}\right)+\rho g_z, \tag{A.25}$$

Bibliography

Abdullah, Normazni and Zuhaila Ismail (2022). "Finite Element Analysis of Biomagnetic Fluid Flow in a Channel with an Overlapping Stenosis". In: *Malaysian Journal of Fundamental and Applied Sciences* 18.6, pp. 618–629. DOI: 10.11113/mjfas.v18n6.2442.

Afonso, A. M., F. T. Pinho, and P. J. Oliveira (2012). "Turbulent flow of viscoelastic fluids: A comparison of closure models". In: *Journal of Non-Newtonian Fluid Mechanics* 175, pp. 1–10.

Aldosari, S. M. et al. (2023). "Drug release using nanoparticles in the cancer cells on 2-D materials in order to target drug delivery: A numerical simulation via molecular dynamics method". In: *Engineering Analysis With Boundary Elements* 148, pp. 34–40. DOI: 10.1016/j.enganabound.2022.12.020.

Algehyne, E. A. et al. (2023). "Entropy optimization and response surface methodology of blood hybrid nanofluid flow through composite stenosis artery with magnetized nanoparticles $(Au\text{-}Ta)$ for drug delivery application". In: *Scientific Reports* 130, p. 9856. DOI: 10.1038/s41598-023-36931-6.

Alias, N. et al. (2016). "Numerical analysis on mathematical model for drug delivery system on blood flow in external magnetic fields by magnetic nanoparticles". In: 78, pp. 31–37. DOI: 10.11113/JT.V78.8290.

Antoniac, I. V. et al. (2020). "Synthesis and Characterization of Coated Iron Oxide Nanoparticles Produced for Drug Delivery in Viscoelastic Solution". In: *Revista De Chimie* 71.4, pp. 145–154. DOI: 10.37358/RC.20.4.8053.

Barbieri, M. (2023). "Mathematical Modeling and Numerical Simulations for Drug Release from PLGA Particles". In: *Lecture Notes in Computer Science*, pp. 347–360. DOI: 10.1007/978-3-031-36030-5_28.

Basha, H. T. et al. (2022a). "Finite Difference Computation of Au-Cu/Magneto-Bio-Hybrid Nanofluid Flow in an Inclined Uneven Stenosis Artery". In: *Complexity* 3, pp. 1–18. DOI: 10.1155/2022/2078372.

— (2022b). "Finite Difference Computation of Au-Cu/Magneto-Bio-Hybrid Nanofluid Flow in an Inclined Uneven Stenosis Artery". In: *Complexity* 3, pp. 1–18. DOI: 10.1155/2022/2078372.

Berger, S. A. and L-D. Jou (2000). "Flows in Stenotic Vessels". In: *Annual Review of Fluid Mechanics* 32.Volume 32, 2000, pp. 347–382. ISSN: 1545-4479. DOI: https://doi.org/10.1146/annurev.fluid.32.1.347.

Biglarian, M. et al. (2020). "Computational investigation of stenosis in curvature of coronary artery within both dynamic and static models". In: *Computer methods and programs in biomedicine* 185, p. 105170.

Boussinesq, J. (1877a). "Essai sur la théorie des eaux courantes". In: *Mémoires présentés par divers savants à l'Académie des Sciences* 23. DOI: 10.1002/zamm.19420220502.

— (1897). "Théorie de l'écoulement tourbillonnant et tumultueux des liquides dans les lits rectilignes à grande section." In: *Gauthier-Villars* 1.

Boussinesq, Joseph (1877b). "Theorie de l'ecoulement tourbillant". In: *Mem. Acad. Sci.* 23, p. 46.

Bruschi, M. L. and L. de A. S. de Toledo (2019). "Pharmaceutical Applications of Iron-Oxide Magnetic Nanoparticles". In: *Magnetochemistry* 5.3, p. 50. DOI: 10.3390/MAGNETOCHEMISTRY5030050.

Buradi, A. and A. Mahalingam (2018). "Effect of stenosis severity on wall shear stress based hemodynamic descriptors using multiphase mixture theory". In: *J. Appl. Fluid Mech.* 11, pp. 1497–1509. DOI: 10.29252/jafm.11.06.29062.

Burns, Alan (2023). *Lipid Concentration Effects on Blood Flow Through Stenosed Tube*.

Burton, A. C. (1972). "TPhysiology and biophysics of the circulation: an introductory text". In: *Year Book Medical Publishers*.

Caro, C. G. (2001). "Vascular fluid dynamics and vascular biology and disease". In: *Math. Meth. Appl. Sci.* 24, pp. 1311–1324. DOI: 10.1002/mma.181.

Carvalho, V. et al. (2020a). "3D printed biomodels for flow visualization in stenotic vessels: An experimental and numerical study". In: *Micromachines* 11.6, p. 549.

Carvalho, Violeta et al. (2020b). "Numerical simulation of blood pulsatile flow in stenotic coronary arteries: The effect of turbulence modeling and non-Newtonian assumptions". In: *2020 24th International Conference on Circuits, Systems, Communications and Computers (CSCC)*, pp. 112–116. DOI: 10.1109/CSCC49995.2020.00027.

Casciola, Carlo Massimo, A Olivieri, Renzo Piva, et al. (1998). "Threshold amplitude of local disturbances in the transition of wall bounded flows". In: *Euromech colloquium 380/Ercoftac sig33*.

Cassano, R. et al. (2022). *Copper nanoparticles-based stimuli-responsive approaches*. DOI: 10.1016/b978-0-12-824456-2.00015-1.

Cavaccini, Giovanni et al. (2006). "Mathematical and numerical modeling of liquids dynamics in a horizontal capillary". In: *Recent Progress in Computational Sciences and Engineering, ICCMSE* 1, pp. 1–5.

Cebeci, Tuncer and AMO Smith (1968). *A finite-difference solution of the incompressible turbulent boundary-layer equations by an eddy-viscosity concept*. Douglas Aircraft Company.

Chaichana, T., Z. Sun, and J. Jewkes (2013). "Hemodynamic impacts of various types of stenosis in the left coronary artery bifurcation: a patient-specific analysis". In: *Physica Medica* 29.5, pp. 447–452.

Chakraborty, Bhaskar et al. (2024). "Multi-Scale Modelling of Boiling Heat Transfer: Exploring the Applicability of an Enhanced Volume of Fluid Method in Submicron Scales". In: *International Journal of Thermofluids*, p. 100683.

Chakravarty, K. and D. C. Dalal (2018). "Mathematical modelling of liposomal drug release to tumour". In: *Mathematical Biosciences* 306, pp. 82–96. ISSN: 0025-5564. DOI: https://doi.org/10.1016/j.mbs.2018.10.012. URL: https://www.sciencedirect.com/science/article/pii/S0025556417306600.

Chakravarty, S. and P. K. Mandal (1994a). "Mathematical modelling of blood flow through an overlapping arterial stenosis". In: *Mathematical and computer modelling* 19.1, pp. 59–70.

Chakravarty, S. and P.K. Mandal (1994b). "Mathematical modelling of blood flow through an overlapping arterial stenosis". In: *Mathematical and Computer Modelling* 19.1, pp. 59–70. ISSN: 0895-7177. DOI: https://doi.org/10.1016/0895-7177(94)90116-3. URL: https://www.sciencedirect.com/science/article/pii/0895717794901163.

Chalampiari, A., S. Paras, and A. Karabelas (2009). "Flow patterns and turbulence in unbaffled and baffled tanks". In: *Chemical Engineering Science* 64.7, pp. 1376–1388.

Chen, J. and X. Y. Lu (2004). "Numerical investigation of the non-Newtonian blood flow in a bifurcation model with a non-planar branch". In: *Journal of Biomechanics* 37, pp. 1899–1911. DOI: 10.1016/j.jbiomech.2004.02.030.

Choi, S. U. S. and J. A. Eastman (1995). "Enhancing thermal conductivity of fluids with nanoparticles". In: *In: D. A. Siginer and H. P. Wang, Eds., Developments and Applications of Non-Newtonian Flows, ASME, New York* 66, pp. 99–105. DOI: 10.1080/15287394.2013.830584.

Cimmelli, Vito Antonio, Francesco Oliveri, and Angelo Raffaele Pace (2004). "Thermoelectrodynamics of rigid superconductors". In: *Archives of Mechanics* 56.5, pp. 377–389.

— (2011). "On the thermodynamics of Korteweg fluids with heat conduction and viscosity". In: *Journal of Elasticity* 104, pp. 115–131.

Comminal, R et al. (2019). "A hybrid RANS LES approach for turbulent non Newtonian flows: Application to the flow past a cylinder". In: *Journal of Non Newtonian Fluid Mechanics* 273, p. 104181.

Connell, D. J. et al. (2018). "Rationalising drug delivery using nanoparticles: a combined simulation and immunology study of GnRH adsorbed to silica nanoparticles." In: *Scientific Reports* 8.1, pp. 17115–17115. DOI: 10.1038/S41598-018-35143-7.

Daraee, Hadis et al. (2016). "Application of liposomes in medicine and drug delivery." In: *Artificial Cells Nanomedicine and Biotechnology* 44.1, pp. 381–391. DOI: 10.3109/21691401.2014.953633.

De Luca, R et al. (2017). "Towards cavitation-enhanced permeability in blood vessel on a chip". In: *AIP Conference Proceedings*. Vol. 1873. 1. AIP Publishing.

Demetzos, C. (2016). *Application of Nanotechnology in Drug Delivery and Targeting*. DOI: 10.1007/978-981-10-0791-0_4.

Demir, E. et al. (2013). "Determination of TiO_2, ZrO_2, and Al_2O_3 Nanoparticles on Genotoxic Responses in Human Peripheral Blood Lymphocytes and Cultured Embryonic Kidney Cells". In: *Journal of Toxicology and Environmental Health, Part A: Current Issues* 76, pp. 990–1002. DOI: 10.1080/15287394.2013.830584.

Direct, CFD (2015). "OpenFOAM user guide". In: DOI: http://cfd.direct/openfoam/user-guide/.

Dolui, S., B.C. Bhaumik, and S. De (2022). "Combined effect of induced magnetic field and thermal radiation on ternary hybrid nanofluid flow through an inclined catheterized artery with multiple stenosis". In: *Chemical physics letters* 811, pp. 140209–140209. DOI: 10.1016/j.cplett.2022.140209.

Doutel, E. et al. (2019). "Geometrical effects in the hemodynamics of stenotic and non-stenotic left coronary arteries—numerical and in vitro approaches". In: *International Journal for Numerical Methods in Biomedical Engineering* 35.8. e3207 CNM-Nov-18-0300.R1, e3207. DOI: https://doi.org/10.1002/cnm.3207. eprint: https://onlinelibrary.wiley.com/doi/pdf/10.1002/cnm.3207. URL: https://onlinelibrary.wiley.com/doi/abs/10.1002/cnm.3207.

Eastman, J. A. et al. (2001). "Anomalously increased effective thermal conductivities of ethylene glycol-based nanofluids containing copper nanoparticles". In: *Applied Physics Letters* 78.6, pp. 718–720. DOI: 10.1063/1.1341218.

Einstein, A. (1956). "Investigation on the Theory of Brownian Motion". In: *Dover, New York*.

Elhanafy, A., A. Elsaid, and A. Guaily (2020a). "Numerical investigation of hematocrit variation effect on blood flow in an arterial segment with variable stenosis degree". In: *Journal of Molecular Liquids* 313, p. 113550.

Elhanafy, Ahmed, Ahmed Elsaid, and Amr Guaily (2020b). "Numerical investigation of hematocrit variation effect on blood flow in an arterial segment with variable stenosis degree". In: *Journal of Molecular Liquids* 313, p. 113550. ISSN: 0167-7322. DOI: https://doi.org/10.1016/j.molliq.2020.113550. URL: https://www.sciencedirect.com/science/article/pii/S0167732220300945.

Farooq, A. A. et al. (2021). "Entropy production rate in ciliary induced flows through cylindrical tubules under the consequences of Hall effect". In: *Journal of the Taiwan Institute of Chemical Engineers* 120, pp. 207–217. DOI: 10.1016/j.jtice.2021.03.024.

Fazio, Riccardo and Alessandra Jannelli (2020). "A Non-Standard Finite Difference Scheme for MHD Boundary Layer Fluid Flow". In: *arXiv preprint arXiv:2003.06261*.

— (2021). "A non-standard finite difference scheme for magneto-hydro dynamics boundary layer flows of an incompressible fluid past a flat plate". In: *Mathematical and Computational Applications* 26.1, p. 22.

Fraser, Jonathan M. (2023a). *Modelling Pulsatile Blood Flow Using Casson Fluid Model Through an Overlapping Stenotic Artery with Au-Cu Hybrid Nanoparticles: Varying Viscosity Approach*. DOI: 10.1007/978-3-031-29959-9_10.

— (2023b). *Modelling Pulsatile Blood Flow Using Casson Fluid Model Through an Overlapping Stenotic Artery with Au-Cu Hybrid Nanoparticles: Varying Viscosity Approach*. DOI: 10.1007/978-3-031-29959-9_10.

Gandhi, R., Bhupendra K. Sharma, and Oluwole Daniel Makinde (2022). "Entropy analysis for MHD blood flow of hybrid nanoparticles (Au–Al_2O_3/blood) of different shapes through an irregular stenosed permeable walled artery under periodic body acceleration: Hemodynamical applications". In: *Journal of applied mathematics and mechanics*. DOI: 10.1002/zamm.202100532.

Gandhi, R. et al. (2023). "Entropy generation and shape effects analysis of hybrid nanoparticles ($Cu - Al_2O_3$/ blood) mediated blood flow through a time-variant multi-stenotic artery". In: *International Journal of Thermofluids* 18. DOI: 10.1016/j.ijft.2023.100336.

Gao, P., J. Nicolas, and T. Ha-Duong (2021). "Supramolecular Organization of Polymer Prodrug Nanoparticles Revealed by Coarse-Grained Simulations". In: *Journal of the American Chemical Society* 143.42, pp. 17412–17423. DOI: 10.1021/JACS.1C05332.

Gaudio, L. T. et al. (2018). "Different blood flow models in coronary artery diseases: effects on hemodynamic parameters". In: *2018 40th Annual International Conference of the IEEE Engineering in Medicine and Biology Society (EMBC)*. IEEE, pp. 3185–3188.

Ghadikolaei, S. S. et al. (2018). "MHD boundary layer analysis for micropolar dusty fluid containing Hybrid nanoparticles (Cu-Al_2O_3) over a porous medium". In: *Journal of Molecular Liquids* 268, pp. 813–823. DOI: 10.1016/j.molliq.2018.07.105.

Gul, A., E. E. Tzirtzilakis, and S. S. Makhanov (2022). "Simulation of targeted magnetic drug delivery: Two-way coupled biomagnetic fluid dynamics approach". In: *Physics of fluids* 34.2, pp. 021911–021911. DOI: 10.1063/5.0080216.

H, Masuda et al. (1993). "Alteration of Thermal Conductivity and Viscosity of Liquid by Dispersing Ultra-Fine Particles (Dispersion of Al_2O_3, SiO_2 and TiO_2 Ultra-Fine Particles)". In: *Netsu Bussei* 7, pp. 227–233. DOI: 10.2963/jjtp.7.227.

Haand, T. S. et al. (2022). "A Numerical Investigatation Of Blood Flow Through The Aortic Value". In: *Journal of Science and Technique* 17.05. DOI: 10.56651/lqdtu.jst.v17.n05.527.

Haldar, K. (1985a). "Effects of the shape of stenosis on the resistance to blood flow through an artery". In: *Bulletin of Mathematical Biology* 47.4, pp. 545–550. ISSN: 0092-8240. DOI: https://doi.org/10.1016/S0092-8240(85)90020-5. URL: https://www.sciencedirect.com/science/article/pii/S0092824085900205.

Haldar, K (1985b). "Effects of the shape of stenosis on the resistance to blood flow through an artery". In: *Bulletin of mathematical biology* 47, pp. 545–550.

Halevas, E. and A. A. Pantazaki (2018). "Copper Nanoparticles as Therapeutic Anticancer Agents". In: 2, pp. 119–140.

Harun, S. N. et al. (2021). "Synthesis and Optimization of Mesoporous Silica Nanoparticles for Ruthenium Polypyridyl Drug Delivery". In: *Pharmaceutics* 13.2, p. 150. DOI: 10.3390/PHARMACEUTICS13020150.

Haverich, A. and E. C. Boyle (2019). *Atherosclerosis Pathogenesis and Microvascular Dysfunction*.

He, L. et al. (2020). "Glutathione and pH serial responsive functional mesoporous silica nanoparticles for drug delivery". In: *Micro & Nano Letters* 15.5, pp. 291–295. DOI: 10.1049/MNL.2019.0317.

Hoskins, P. R. and D. Hardman (2017). *Blood and blood flow*. DOI: 10.1007/978-3-319-46407-7_3.

Huang, C. R. et al. (1987). "Thixotropic properties of whole blood from healthy human subjects". In: *Biorheology* 24, pp. 795–801. DOI: 10.3233/BIR-1987-24630.

Huang, J. et al. (2023). *Iron Oxide Nanoparticle-Mediated mRNA Delivery to Hard-to-Transfect Cancer Cells*. DOI: 10.3390/pharmaceutics15071946.

Kaushik, Y. et al. (2022). "Effect of Al_2O_3 Nanoparticles on Performance and Emission Characteristics of Diesel Engine Fuelled with Diesel–Neem Biodiesel Blends". In: *Sustainability* 14.13, pp. 7913–7913. DOI: 10.3390/su14137913.

Khanduri, U. and B. K. Sharma (2022). "Hall and ion slip effects on hybrid nanoparticles (*Au-GO*/blood) flow through a catheterized stenosed artery with thrombosis". In: *Proceedings of the Institution of Mechanical Engineers, Part C: Journal of Mechanical Engineering Science* 237.10, pp. 2256–2278. DOI: 10.1177/09544062221136710.

Kojic, M. et al. (2017). "A composite smeared finite element for mass transport in capillary systems and biological tissue". In: *Comput. Methods Appl. Mech Eng.* 24, pp. 413–437. DOI: 110.1016/j.cma.2017.06.019.

Kojić, M. et al. (2008). *Computer Modeling in Bioengineering: Theoretical Background, Examples and Software*.

Ku, D. N. and D. P. Gidden (1983). "Pulsatile flow in a model carotid bifurcation". In: *Arteriosclerosis: An Official Journal of the American Heart Association, Inc.* 3, pp. 31–39. DOI: 10.1161/01.ATV.3.1.31.

Lamichhane, N. et al. (2018). "Liposomes: Clinical Applications and Potential for Image-Guided Drug Delivery." In: *Molecules* 23.2, p. 288. DOI: 10.3390/MOLECULES23020288.

Lee, S. et al. (1999). "Measuring Thermal Conductivity of Fluids Containing Oxide Nanoparticles". In: *Journal of Heat Transfer* 121, pp. 280–289. DOI: 10.1115/1.2825978.

Lilley, GM (1994). "Turbulence Modelling for CFD DC Wilcox DCW Industries, 5354 Palm Drive, La Canada, CA 91011, USA. 1993. 460pp+ software diskette. Illustrated. $75." In: *The Aeronautical Journal* 98.980, pp. 405–405.

Liu, B. et al. (2015). "Influence of model boundary conditions on blood flow patterns in a patient specific stenotic right coronary artery". In: *Biomedical engineering online* 14, pp. 1–17.

Lopes, D. et al. (2021). "Analysis of finite element and finite volume methods for fluid-structure interaction simulation of blood flow in a real stenosed artery". In:

International Journal of Mechanical Sciences 207, p. 106650. ISSN: 0020-7403. DOI: https://doi.org/10.1016/j.ijmecsci.2021.106650.

Lyras, Konstantinos G. and Jack Lee (2021). "Comparison of numerical implementations for modelling flow through arterial stenoses". In: *International Journal of Mechanical Sciences* 211, p. 106780. ISSN: 0020-7403. DOI: https://doi.org/10.1016/j.ijmecsci.2021.106780.

Mahalingam, A. et al. (2016). "Numerical analysis of the effect of turbulence transition on the hemodynamic parameters in human coronary arteries". In: *Cardiovasc. Diagnosis Ther.* 6, pp. 208–220. DOI: 10.21037/cdt.2016.03.08.

Makarishcheva, D. D. et al. (2022). "Development of a Quantitative Determination Method for Aluminum Ions in Adsorbed Drugs Using Atomic Absorption Spectrometry with Electrothermal Atomization". In: *Pharmaceutical Chemistry Journal* 56.4, pp. 527–531. DOI: 10.1007/s11094-022-02669-0.

Mandal, P. K. (2005a). "An unsteady analysis of non-Newtonian blood flow through tapered arteries with a stenosis". In: *International journal of non-linear mechanics* 40.1, pp. 151–164.

Mandal, Prashanta Kumar (2005b). "An unsteady analysis of non-Newtonian blood flow through tapered arteries with a stenosis". In: *International Journal of Non-Linear Mechanics* 40.1. Non-linear Fluid Mechanics, pp. 151–164. ISSN: 0020-7462. DOI: https://doi.org/10.1016/j.ijnonlinmec.2004.07.007. URL: https://www.sciencedirect.com/science/article/pii/S0020746204000940.

Mauro, M. et al. (2009). "In vitro transdermal absorption of Al2O3 nanoparticles". In: *Toxicology in Vitro* 59, pp. 275–280. DOI: 10.1016/j.tiv.2019.04.015.

Maxwell, J. C. (1881). "A Treatise on Electricity and Magnetism". In: *Clarendon Press, Oxford, UK*.

McComb, W. D. (1990). "The Physics of Fluid Turbulence". In: *Oxford University Press*.

Mendis, S., P. Puska, and B. Norrving (2011). "Global atlas on cardiovascular disease prevention and control. WHO". In: *World Health Organization*.

Meng, Y., X. Niu, and G. Li (2022). "Liposome Nanoparticles as a Novel Drug Delivery System for Therapeutic and Diagnostic Applications". In: *Current Drug Delivery* 20, pp. 41–56. DOI: 10.2174/1567201819666220324093821.

Minea, A. A. (2020). "Pumping power and heat transfer efficiency evaluation on Al_2O_3, TiO_2 and SiO_2 single and hybrid water-based nanofluids for energy application". In: *Journal of Thermal Analysis and Calorimetry* 139, 1171—1181. DOI: 10.1007/s10973-019-08510-3.

Mitsoulis, Evan and Thanasis Zisis (2001). "Flow of Bingham plastics in a lid-driven square cavity". In: *Journal of non-newtonian fluid mechanics* 101.1-3, pp. 173–180.

Mok, J., S. Han, and H. Lee (2020). "Study on the blood flow in stenosed microvascular model under pulsed magnetic field". In: *AIP Advances* 10.1, 015005=. DOI: 10.1063/1.5130156.

Moradicheghamahi, J., J. Sadeghiseraji, and M. Jahangiri (2019). "Numerical solution of the Pulsatile, non-Newtonian and turbulent blood flow in a patient specific elastic carotid artery". In: *International Journal of Mechanical Sciences* 150, pp. 393–403.

Morris, P. D. et al. (2016). "Computational fluid dynamics modelling in cardiovascular medicine". In: *Cardiovasc. Diagnosis Ther.* 6, pp. 208–220. DOI: 10.21037/cdt.2016.03.08.

Mulpuru, Viswajit, Akhilesh Kumar Maurya, and Nidhi Mishra (2019). "CFD Analysis of Anticancerous Ag and CuO Nanoparticles in Tumor Angiogenic Vessels". In: 2019, pp. 1–2. DOI: 10.1109/INDICON47234.2019.9030301.

Naatz, H. et al. (2020a). "Model-Based Nanoengineered Pharmacokinetics of Iron-Doped Copper Oxide for Nanomedical Applications". In: *Angewandte Chemie* 59.5, pp. 1828–1836. DOI: 10.1002/ANIE.201912312.

— (2020b). "Model-Based Nanoengineered Pharmacokinetics of Iron-Doped Copper Oxide for Nanomedical Applications". In: *Angewandte Chemie* 59.5, pp. 1828–1836. DOI: 10.1002/ANIE.201912312.

Nadeem, Sohail et al. (2023). "Numerical computations of blood flow through stenosed arteries via CFD tool OpenFOAM". In: *Alexandria Engineering Journal* 69, pp. 613–637. ISSN: 1110-0168. DOI: https://doi.org/10.1016/j.aej.2023.02.005. URL: https://www.sciencedirect.com/science/article/pii/S1110016823001035.

Najafi, M., A. Morsali, and M. Reza Bozorgmehr (2019). "DFT study of SiO 2 nanoparticles as a drug delivery system: structural and mechanistic aspects". In: *Structural Chemistry* 30.3, pp. 715–726. DOI: 10.1007/S11224-018-1227-9.

Naser, N. N. N. M., I. Abdullah, and A. H. Talib (2019). "Velocity distribution of biomagnetic blood flow through a cosine-shaped stenosed artery". In: 2138.1, p. 030028. DOI: 10.1063/1.5121065.

Oliveira, P. J. and F. T. Pinho (1998). "Numerical procedure for the computation of viscoelastic flows using a modified porous medium formulation". In: *Journal of Non-Newtonian Fluid Mechanics* 79.1, pp. 1–22.

Omamoke, E. and E. Amos (2023). "Treatment and Slip Effect on MHD Blood Flow through a Stenotic Artery: A Mathematical Model". In: *Asian Research Journal of Mathematics* 19.6, pp. 61–76. DOI: 10.9734/arjom/2023/v19i6666.

Osborne, R. (1883). "XXIX. An experimental investigation of the circumstances which determine whether the motion of water shall be direct or sinuous, and of the law of resistance in parallel channels." In: *Philosophical Transactions of the Royal society of London* 174, pp. 935–982. DOI: 10.1098/rstl.1883.0029.

Pak, B. C. and Y. Cho (1998). "Hydrodynamic and heat transfer study of dispersed fluids with submicron metallic oxide particle". In: *Experimental Heat Transfer* 11, pp. 151–170. DOI: 10.1080/08916159808946559.

Pandey, R. et al. (2009). "Silica nanoparticles postloaded with photosensitizers for drug delivery in photodynamic therapy". Pat.

Pathak, T. S. and S. Afkhami (2023). "Enhancing Simulations of Superparamagnetic Magnetic Drug Delivery to Predict Efficacy of Treatment". In: *Journal of Student Research* 12.1. DOI: 10.47611/jsrhs.v12i1.4088.

Paulsen, D. F. (2010). "Chapter 11. Circulatory System". In: *Histology & amp; Cell Biology: Examination & Board Review, 5e*. New York, NY: The McGraw-Hill Companies. URL: accessmedicine.mhmedical.com/content.aspx?aid=57093947.

Pedley, T. J. (1980). *The Fluid Mechanics of Large Blood Vessels*. Cambridge Monographs on Mechanics. Cambridge University Press.

Perktold, K. et al. (1991). "Pulsatile non-Newtonian blood flow in three-dimensional carotid bifurcation models: a numerical study of flow phenomena under different bifurcation angles". In: *Journal of Biomedical Engineering* 13, pp. 507–515. DOI: 10.1016/0141-5425(91)90100-L.

Pinho, Fernando T, Paulo J Oliveira, and Ana I Miranda (2001). "Assessment of the performance of viscoelastic constitutive equations in steady shear flows of non-Newtonian fluids". In: *Journal of Non-Newtonian Fluid Mechanics* 95.2-3, pp. 153–184.

Pontrelli, G (2001). "Blood flow through an axisymmetric stenosis". In: *Year Book Medical Publishers* 215, pp. 1–10. DOI: 10.1177/095441190121500101.

Prandtl, L. (1925). "Bericht über Untersuchungen zur ausgebildeten Turbulenz". In: *ZAMM-Journal of Applied Mathematics and Mechanics Zeitschrift für Angewandte Mathematik und Mechanik* 5. DOI: 10.1002/zamm.19250050212.

— (1942). "Bemerkungen zur Theorie der freien Turbulenz". In: *ZAMM-Journal of Applied Mathematics and Mechanics Zeitschrift für Angewandte Mathematik und Mechanik* 22. DOI: 10.1002/zamm.19420220502.

Pulingam, T. et al. (2022). "Exploring Various Techniques for the Chemical and Biological Synthesis of Polymeric Nanoparticles". In: *Nanomaterials* 12.3, pp. 576–576. DOI: 10.3390/nano12030576.

Rabby, M. G., A. Razzak, and M. M. Molla (2017). "Pulsatile non-Newtonian blood flow through a model of arterial stenosis". In: *Procedia Eng.* 56, pp. 225–231. DOI: 10.1016/j.proeng.2013.03.111.

Reynolds, O. (1894). "On the dynamical theory of incompressible viscous fluids and the determination of the criterion". In: *Philosophical transactions of the royal society of London.(a.)* 186. DOI: 10.1098/rsta.1895.0004.

Richardson, L. F. (2010). *Weather prediction by numerical process*. DOI: 10.1017/CBO9780511618291.

Ritchie, H. (2018). "Causes of Death". In: *Our World in Data*. URL: https://ourworldindata.org/causes-of-death.

Robison, Jason Anthony (2023). *Fluid-Structure Interaction: Numerical Analysis of Biomagnetic Flow Inhibition on a Plaque in a Stenosed Bifurcation Artery*. DOI: 10.20944/preprints202303.0117.v1.

Rumsey, Christopher et al. (2004). "Summary of the 2004 CFD validation workshop on synthetic jets and turbulent separation control". In: *2nd AIAA Flow Control Conference*, p. 2217.

Sahai, N., M. Gogoi, and N. Ahmad (2021). "Mathematical Modeling and Simulations for Developing Nanoparticle-Based Cancer Drug Delivery Systems: A Review". In: *Current Pathobiology Reports* 9.1, pp. 1–8. DOI: 10.1007/S40139-020-00219-5.

Sarkar, Sutanu, and B. Lakshmanan (1991). "Application of a Reynolds stress turbulence model to the compressible shear layer." In: *AIAA journal* 29, pp. 743–749. DOI: 10.2514/3.10649.

Sarwar, L. et al. (Oct. 2022). "Thermal enhancement and numerical solution of blood nanofluid flow through stenotic artery". In: *Scientific Reports* 12. DOI: 10.1038/s41598-022-20267-8.

Schlichting, Hermann and Klaus Gersten (2016). *Boundary-layer theory*. springer.

Sharma, B. K., Poonam, and A. J. Chamkha (2022). "Effects of heat transfer, body acceleration and hybrid nanoparticles (Au–Al2O3) on MHD blood flow through a curved artery with stenosis and aneurysm using hematocrit-dependent viscosity". In: *Waves in Random and Complex Media*, pp. 1–31. DOI: 10.1080/17455030.2022.2125597.

Shi, Y., P. Lawford, and R. Hose (2011). "Review of Zero-D and 1-D Models of Blood Flow in the Cardiovascular System". In: *BioMedical Engineering OnLine* 33, pp. 275–280. DOI: 10.1186/1475-925X-10-33.

Siogkas, P. K. et al. (2015). "Patient-specific simulation of coronary artery pressure measurements: an in vivo three-dimensional validation study in humans". In: *BioMed Research International* 2015.

Sodagar, Hamid, Ali Shakiba, and Hamid Niazmand (2020). "Numerical investigation of drug delivery by using magnetic field in a 90-degree bent vessel: a 3D simulation". In: *Biomechanics and Modeling in Mechanobiology* 19.6, pp. 2255–2269. DOI: 10.1007/S10237-020-01337-0.

Spalart, Philippe and Steven Allmaras (1992). "A one-equation turbulence model for aerodynamic flows". In: *30th aerospace sciences meeting and exhibit*, p. 439.

Spivak, Yu. M. et al. (2022). "Porous Aluminum Oxide for Medical Applications Including Targeted Drug Delivery". In: *Nano- i mikrosistemnaâ tehnika* 24.10, pp. 258–268. DOI: 10.17587/nmst.24.258-268.

Suciu, M. et al. (2020). "Applications of superparamagnetic iron oxide nanoparticles in drug and therapeutic delivery, and biotechnological advancements." In: *Beilstein Journal of Nanotechnology* 11.1, pp. 1092–1109. DOI: 10.3762/BJNANO.11.94.

Supratim, S. (2023). "Numerical Investigation of Blood Flow Through Stenosed Coronary Artery Using Reduced Order Model". In: *Fluid Mechanics and Fluid Power (Vol. 2)*. Ed. by Suvanjan Bhattacharyya and Ali Cemal Benim. Singapore: Springer Nature Singapore, pp. 87–92. ISBN: 978-981-19-6970-6.

Tang, D., C. Yang, and D. N. Ku (1999). "A 3-D thin-wall model with fluid–structure interactions for blood flow in carotid arteries with symmetric and asymmetric stenoses". In: *Computers & structures* 72.1-3, pp. 357–377.

Tatarchuk, T. et al. (2023). "Iron Oxide Nanomaterials for Bacterial Inactivation and Biomedical Applications". In: *Nanooptics and Photonics, Nanochemistry and Nanobiotechnology, and Their Applications*. Springer International Publishing, pp. 207–221.

Taylor, G. I. (1932). "The transport of vorticity and heat through fluids in turbulent motion". In: *Proceedings of the Royal Society of London. Series A* 135. DOI: 10.1098/rspa.1932.0061.

Tortora, G. J. and S. R. Grabowski (2000). In: *Principles of Anatomy and Physiology*. John Wiley and Sons, Inc.

Tripathi, J., B. Vasu, and O. A. Bég (2021). "Computational simulations of hybrid mediated nano-hemodynamics (Ag-Au/Blood) through an irregular symmetric stenosis". In: *Computers in Biology and Medicine* 130, p. 104213.

Tripathi, J., B. Vasu, and O. Bég (2021). "Computational simulations of hybrid mediated nano- hemodynamics (Ag-Au/Blood) through an irregular symmetric stenosis". In: *Computers in Biology and Medicine* 130, p. 104213. DOI: 10.1016/j.compbiomed.2021.104213.

Tyagi, A. K., A. Arya, and S. Tyagi (2023). "Development of copper nanoparticles and their prospective uses as antioxidants, antimicrobials, anticancer agents in the pharmaceutical sector". In: *Precision nanomedicine*. DOI: 10.33218/001c.83932.

Umadevi, C. et al. (2021). "Effects of magnetic field on blood flow with suspended copper nanoparticles through an artery with overlapping stenosis". In: 8.1. DOI: 10.36963/IJTST.2021080103.

Van Driest, Edward R (1956). "On turbulent flow near a wall". In: *Journal of the aeronautical sciences* 23.11, pp. 1007–1011.

Varghese, R., N. Vijay, and Y. B. Dalvi (2021). *Magnetic Nanoparticles for Image-Guided Drug Delivery*. DOI: 10.1007/978-981-16-1260-2_3.

Vasu, B., A. Dubey, and O. A. Bég (Oct. 2019). "Finite Element Analysis of Non-Newtonian Magneto-Hemodynamic Flow Conveying Nano-Particles through a Stenosed Coronary Artery". In: *Heat Transfer-Asian Research*. DOI: 10.1002/htj.21598.

Versteeg, Henk Kaarle (2007). *An introduction to computational fluid dynamics the finite volume method, 2/E*. Pearson Education India.

Wilcox, David C et al. (1998). *Turbulence modeling for CFD*. Vol. 2. DCW industries La Canada, CA.

Wootton, D. M. and D. N. Ku (1999). "Fluid Mechanics of Vascular Systems, Diseases, and Thrombosis". In: *Annual Review of Biomedical Engineering* 1, pp. 299–329. DOI: 10.1146/annurev.bioeng.1.1.299.

Wu, J. et al. (2015). "Transient blood flow in elastic coronary arteries with varying degrees of stenosis and dilatations: CFD modelling and parametric study". In: *Computer Methods in Biomechanics and Biomedical Engineering* 18.16, pp. 1835–1845.

Xiao, X. et al. (2022). "Polymeric nanoparticles—Promising carriers for cancer therapy". In: *Frontiers in Bioengineering and Biotechnology* 10. DOI: 10.3389/fbioe.2022.1024143.

Xingting, L. et al. (2022). "The thermal behavior of blood flow in the arteries with various radii and various stenosis angles using non-Newtonian Sisko model". In: *Alexandria Engineering Journal* 61, pp. 7195–7201. DOI: 10.1016/j.aej.2021.12.063.

Xuan, Y. and W. Roetzel (2000). "Conceptions for heat transfer correlation of nanofluids". In: *Journal of Molecular Liquids* 43, 3701—3707. DOI: 10.1016/S0017-9310(99)00369-5.

Yan, S. et al. (2020a). "Numerical investigation of non-Newtonian blood flow within an artery with cone shape of stenosis in various stenosis angles". In: *Computer methods and programs in biomedicine* 192, p. 105434.

Yan, Shu-Rong et al. (2020b). "Numerical investigation of non-Newtonian blood flow within an artery with cone shape of stenosis in various stenosis angles". In: *Computer Methods and Programs in Biomedicine* 192, p. 105434. ISSN: 0169-2607. DOI: https://doi.org/10.1016/j.cmpb.2020.105434. URL: https://www.sciencedirect.com/science/article/pii/S0169260719324228.

Yanrong, F. et al. (2019). "Liposome nanoparticle drug delivery system loaded with small interference RNA and preparation method and applications thereof". Pat.

Yerpude, S.T. et al. (2022). "CHAPTER FOURTEEN - Computational analysis of nanofluids-based drug delivery system: Preparation, current development and applications of nanofluids". In: *Applications of Nanofluids in Chemical and Biomedical Process Industry*. Ed. by Shriram S. Sonawane et al. Elsevier, pp. 335–364. ISBN: 978-0-323-90564-0. DOI: https://doi.org/10.1016/B978-0-323-90564-0.00014-3. URL: https://www.sciencedirect.com/science/article/pii/B9780323905640000143.

Zafar, M. et al. (2022). "Performance Analysis of Magnetic Nanoparticles during Targeted Drug Delivery: Application of OHAM". In: 130.2, pp. 723–749. DOI: 10.32604/cmes.2022.017257.

Zhou, F.-F. (2017). "Coronary Artery Diameter is Inversely Associated with the Severity of Coronary Lesions in Patients Undergoing Coronary Angiography". In: *Cell. Physiol. Biochem.* 43, pp. 1247–1257. DOI: 10.1159/000481765.